HEAT AND CHEMICAL TRANSPORT IN AQUIFERS AT DIFFERENT GEOLOGICAL SETTING

A Dissertation

by

KEWEI CHEN

Submitted to the Office of Graduate and Professional Studies of
Texas A&M University
in partial fulfillment of the requirements for the degree of

DOCTOR OF PHILOSOPHY

Chair of Committee,	Hongbin Zhan
Committee Members,	Peter S. Knappett
	Benchun Duan
	David Sparks
Head of Department,	Michael Pope

December 2018

Major Subject: Geology

ABSTRACT

Heat and chemical transport are two fundamental processes that are widely existed in the subsurface environments and come with natural phenomena (e.g., volcanic eruption, diurnal or seasonal temperature variation) or anthropogenic activities (e.g., well injection). A common characteristic of these two transport processes is they are both governed by the advection-dispersion equation (ADE) and both advective movements are impacted by the local heterogeneity of porous media. However, they still exhibit many different behaviors. For example, heat diffusivity in the solid matrix is usually two order of magnitude higher than the matrix diffusivity of chemicals. In addition, chemical transport usually comes with reaction and sorption. To investigate the characteristic behaviors of heat and chemical transport at different geological settings, this study focuses on three geological environments ranging from kilometer-scale to meter-scale, including volcanic hydrothermal system, shallow riverbeds where surface-water and groundwater exchange occurs and local fractured aquifer for well testing. For the volcanic hydrothermal system, a novel model that connects the heat and chemical transport is proposed to explain the over 10-year temperature and chemical data collected at the thermal springs near volcanic summit. For the shallow riverbeds, an ensemble data assimilation approach is proposed to estimate the hydraulic exchange flux between surface water and groundwater based on the heat transport observed in the riverbeds. For the local fractured aquifer, a novel fractional model for single-well push-pull test is proposed to explain the observed long tailing behavior of conservative tracer

during pumping. This study demonstrates the capability of using heat and chemical as tracers to quantitatively or qualitatively estimate the flow and transport behaviors at different geological environments. Further work is needed to explore the capability of model and methods to accommodate more geological conditions.

ACKNOWLEDGEMENTS

I would like to thank my committee chair, Dr. Hongbin Zhan, and my committee members, Dr. Peter S. Knappett, Dr. David Sparks and Dr. Benchun Duan, for their guidance and support throughout the course of this research.

I would also like to thank Dr.Xingyuan Chen for her guidance on the work at Pacific Northwest National Laboratory.

Thanks also go to my colleagues and the department faculty and staff for making my time at Texas A&M University a great experience.

Finally, thanks to my mother and father for their encouragement throughout my Ph.D. journey.

CONTRIBUTORS AND FUNDING SOURCES

Contributors

This work was supervised by a dissertation committee consisting of Professor Hongbin Zhan, David Sparks, Benchun Duan of the Department of Geology & Geophysics and Professor Peter S. Knappett of the Department of Water Management and Hydrological Science.

The data analyzed for Chapter II was provided by Erick R. Burns of the United States Geological Survey. The data and analyses depicted in Chapter III were conducted in part by Xingyuan Chen of the Pacific Northwest National Laboratory. The data analyzed for Chapter IV was provided by Qiang Yang of Columbia University.

All other work conducted for the dissertation was completed by the student independently.

Funding Sources

Graduate study was supported by a fellowship from Texas A&M University.

TABLE OF CONTENTS

ABSTRACT ii

ACKNOWLEDGEMENTS iv

CONTRIBUTORS AND FUNDING SOURCES v

TABLE OF CONTENTS vi

LIST OF FIGURES viii

LIST OF TABLES xiii

CHAPTER I INTRODUCTION 1

CHAPTER II THE INFLUENCE OF EPISODIC SHALLOW MAGMA DEGASSING ON HEAT AND CHEMICAL TRANSPORT IN VOLCANIC HYDROTHERMAL SYSTEMS 3

- 2.1. Introduction 3
- 2.2. Geological Setting 4
- 2.3. Conceptual Model and Method of Analysis 7
- 2.4. Results 12
- 2.5. Discussion and Conclusions 21
- References 23

CHAPTER III USING ENSEMBLE DATA ASSIMILATION TO ESTIMATE TRANSIENT HYDROLOGIC EXCHANGE FLUXES UNDER HIGHLY DYNAMIC FLOW CONDITIONS 27

- 3.1 Introduction 27
- 3.2. Methodology 31
- 3.3 Results and discussion 40
- 3.4 Application and limitation 54
- 3.5 Conclusion 57
- References 57

CHAPTER IV FRACTIONAL MODELS SIMULATING NON-FICKIAN BEHAVIOR IN FOUR-STAGE SINGLE-WELL PUSH-PULL TESTS 63

- 4.1. Introduction 63
- 4.2. Methodology 67
- 4.3. Discussion 80

4.4. Modeling of SWPP Tests 92
4.5. Applicability and limitation 96
4.6. Conclusions 99
References 101

CHAPTER V SUMMARY 108

APPENDIX A 110

APPENDIX B 115

LIST OF FIGURES

Page

Figure 2.1 (a) Map showing the Caribbean volcanic arc with the location of La Soufrière volcano. (b) Contour map near the summit of La Soufrière volcano. Symbols in the contour map: (1) flank collapse scars; (2) La Grande Découverte Caldera; (3) La Soufrière dome; (4) summit fractures; (5) La Ty fault system; (6) 1976–1977 fumaroles active until 1981; (7) La Ty fumarolic field (weakly active until 1997); (8) summit fumaroles active since 1997; (9) fumaroles with intermittent acid lakes; (10) Savane à Mulets (SAM) and Col de l'Echelle (CDE) wells. The hydrothermally altered zone is yellow and thermal springs are indicated by large labeled circles (modified from Villemant et al., 2014). (c) Conceptual model for pulsatory degassing into near-surface aquifers at La Soufrière dome. Recharge occurs on the up-dip side of the hydrothermal alteration zones, with some possible recharge from the "meteoric water" lines. Red star, the zone of interaction between aquifer and volcanic gases; blue arrow, flow path; dashed line, outline of the deep hydrothermal system; solid line connecting magma reservoir and dome, eruptive conduit. 5

Figure 2.2 Comparison between the square-wave chloride source (Chen, this study) and instantaneous-source used by Villemant et al. (2005), and estimated Cl mass and amount of heat in individual pulses. (a) Plot showing that Cl pulse concentration estimated by the current study and Villemant et al. (2005) are generally correlated with seismicity and each other, Red line: the square-wave chloride pulses. Blue dot: instantaneous sources (scaled for comparison to a similar range as the square wave) inferred by Villemant et al. (2005). Gray line: number of detected earthquakes for comparison with degassing loading; (b) The time between the starting points of successive square-wave pulses showing that pulse frequency decreases over time; (c) Cross-plot of the Cl mass M_{Cl} (kg) and amount of heat Q (TJ) delivered in individual pulses, showing that heat and Cl delivered in each pulse is correlated, where M_{Cl} = flow rate × pulse duration × pulse concentration and Q = volumetric heat capacity of water × flow rate × pulse duration × (local boiling temperature – background recharge temperature); (d) plot of M_{Cl} and Q delivered in individual pulses over time, showing the decrease in heat and Cl delivered by individual pulses over time.....14

Figure 2.3 Measured and simulated Cl concentrations and temperatures at springs of CE (proximal to the summit, ~75 m distant), Ga (intermediate to the summit, ~650 m) and CC (distal to the summit, ~2800 m). (a) CE spring Cl concentration responds quickly to the degassing activity (~3 months' delay) and the delay times for Ga and CC spring are ~2.1 years and ~9 years,

respectively. (b) Measured and simulated temperature: CE spring temperature decays with the decreasing pulse frequency; Ga spring temperature increases ~3 °C from 1979 to 1982 and then remains constant; CC spring temperature is constant at 45 °C from 1979 to 1991. Dashed line: Simulated CE spring temperature assuming no episodic degassing pulse heating except the heating from the first one-year pulse. The difference between the CE solid and dashed lines is the result of heat pulses to the aquifer from degassing. 16

Figure 2.4 BTCs and temperature profiles generated for different heat pulse durations using the model for Ga spring (x = 650 m). Fraction of thermal signal = (observed temperature at x – steady temperature at x) / (local boiling temperature - steady temperature at x). (a) BTCs at Ga spring with 1-, 10-, 30-, 100- and 1000-year pulse duration. After 1000 years the full thermal signal has not reached the Ga spring despite having an estimated advective travel time of ~2.1 years; b) The distribution of temperature along the groundwater flowpath at four different times, 1-, 10-, 30- and 100-year, resulting from two different pulse durations. The 10-year pulse is shown with solid lines, and the 100-year pulse is shown with discrete symbols. For times less than 10 years, the profiles are identical. Between 10 and 100 years, temperatures continue to rise for the 100-year pulse, but the 10-year pulse quickly damps and translates towards the spring (distance = 650 m).....20

Figure 3.1 Location map and collected data. a. The field site at Hanford 300 area where the thermistor, piezometers and the river gauge are installed. b. River stage between 7/2016 and 7/2017. Note that there is a 7-days gap in early Nov., 2016 and early June, 2017. c. River temperature and subsurface temperatures at depths -0.04 m, -0.24 m and -0.64 m between 7/2016 and 7/2017. Note that upwelling of cold groundwater and hot groundwater are observed in summer and winter, respectively.....32

Figure 3.2 Thermistor configuration and the associated 1-D hydro-thermal model. Schematic diagram of the thermistor and the 1-D hydro-thermal model that simulate the fluid and heat flow along the thermistor. Temperatures recorded by middle sensors at depths -0.04 m and -0.24 m are considered to be observations, and the hydraulic heads and temperatures at the river and bottom side are used as boundary conditions to drive the 1-D numerical model. The grid dimension of the 1-D numerical model is 0.01 m.....38

Figure 3.3 3-D hydro-thermal model of the study site. Permeability field of the 3-D numerical model with the dimension 400 m×400 m×20 m built for the study site. Black spot is the location where the thermistor is installed.....40

Figure 3.4 Estimation of permeability, thermal conductivity and porosity of 1-D hydro-thermal model using ES-MDA by considering two parameter set(a) and three parameter set(b). a1-a4 and a5-a8 show the evolution of permeability(k) and thermal conductivity(λ), respectively, with the assimilation time windows t=1000,2000,4000 and 8000 minutes. b1-b4, b5-b8 and b9-b12 show the evolution of permeability, thermal conductivity and porosity(φ), respectively, with the number of data points t=200,400,800 and 1600. 42

Figure 3.5 Error of estimated k and λ with different observation error ratio. a. k and λ are estimated, b. k, λ and φ are estimated. 43

Figure 3.6 Performance of data assimilation methods and the accuracy of estimated HEF under synthetic 1-D flow condition. a. Estimated temperature at the depth of -0.25 m using prior ensemble of permeability and thermal conductivity. b. Posterior temperature at the depth of -0.25 m using EnKF method. c-d. Posterior temperature at the depth of -0.25 m using ES-MDA method after 2 and 4 iterations, respectively. e. Temperature at the depth -0.25 m and correlated hydraulic conductivity using equation 6 based on the estimated permeability. Note that a sharp increase of hydraulic conductivity is observed in Jan., 2017 due to the upwelling of hot groundwater. f. Comparison between the true HEF calculated by PFLOTRAN and the estimated HEF based on Darcy's law. g. Correlation between the true HEF and estimated HEF. h. Correlation between the true HEF and the ratio of the true HEF to hydraulic gradient. 46

Figure 3.7 Estimation of HEF without hydraulic head information under synthetic 1-D flow condition. The observations are synthetic temperature time series collected at the frequency of 5 minutes from the depths of -0.05 m, -0.15 m and -0.25 m. Only flux qis estimated assuming φ and λare known. a. River temperature and simulated temperatures at different depths. b-d. Estimated HEFs by assimilating 1-point temperature data from depth -0.05 m and 3-points data from three observation depths using 15-minutes(b), 30-minutes(c) and 1-hour(d) assimilation time windows. 48

Figure 3.8 Sensitivity of HEF estimation without hydraulic head information to the number of estimated parameters. Three parameter sets are considered, including 1 parameter q, two parameters q and φand three parameters q,φ and λ. The temperature time series are extracted from the synthetic 1-D model at the depth -0.05 m and the assimilation time window is 15-minutes..49

Figure 3.9 Estimation of HEF using continuous and discontinuous assimilation schemes. Continuous assimilation scheme means using the posterior parameters from previous assimilation time window as the prior of the

current assimilation time window, and discontinuous assimilation scheme means regenerating prior parameters for current time window if the flow direction is found to be reversed. If the flow direction changes from downwelling to upwelling, the new prior of hydraulic gradient is generated with the mean and standard deviation set to be -0.4 and 0.2, respectively, and if the flow direction changes from upwelling to downwelling, the mean and standard deviation of the new prior of hydraulic gradient is set to be 0.4 and 0.2, respectively. Note that the discontinuous scheme requires the flow direction information known in advance, which could be inferred from the hydraulic head measurements. The temperature time series are extracted from the synthetic 1-D model at the depth -0.05 m and the assimilation time window is 15-minutes. Three parameters, including q,φ and λ, are estimated. 51

Figure 3.10 Estimation of HEF under 3-D homogeneous (a) and heterogeneous (b) flow conditions without hydraulic head information. Temperature observation is from the depth of -0.05 m and assimilation time window is 15 minutes. q,φand λare estimated together. 52

Figure 3.11 Estimation of HEF under 3-D homogeneous (a) and heterogeneous (b) flow conditions without hydraulic head information. Temperature observation is from the depth of -0.05 m and assimilation time window is 15 minutes. q, φ and λ are estimated together. 53

Figure 3.12 Estimated HEF between 7/2016 and 5/2018 using real temperature observations recorded at the Hanford site. Temperature is collected every 5 minutes. The temperature at the depth of -0.24 m is used as observation, and the temperature at the depth of -0.04 m and -0.64 m are used as boundary condition. Hydraulic heads are recorded at the depth of -0.55 m and -2.71 m near the thermistor. a. Observed river stage. b. Observed temperatures at different depths. c. Estimated HEF using continuous and discontinuous schemes. d. Posterior temperature by continuous and discontinuous schemes. 55

Figure 4.1 Calibration of the FORMIM model and the FS model with α = 2 at the end of each stage of the SWPP test, including injection, chasing, resting and pumping. (a) Distribution curve of the relative mobile concentration at each stage; (b) Distribution curve of the relative immobile concentration at each stage. 81

Figure 4.2 Distribution curves of the mobile concentration at the end of each stage of the SWPP test using the FS model with α = 1.4, 1.6, 1.8 and 2 and retardation factor (1+β). (a) Distribution curves at the end of injection; (b)

Distribution curves at the end of chasing; (c) Distribution curves at the end of resting; (d) Distribution curve after 50 hours of pumping. 83

Figure 4.3 Distribution curves of the mobile concentration at the end of each stage of the SWPP test using the FT model with γ = 0.4, 0.6, 0.8 and 1. (a) Distribution curves at the end of injection; (b) Distribution curves at the end of chasing; (c) Distribution curves at the end of resting; (d) Distribution curves after 50 hours of pumping. 84

Figure 4.4 BTCs during the pumping stage. (a) FS model with α = 1.4, 1.6, 1.8 and 2; (b) FT model with γ = 0.4, 0.6, 0.8 and 1. 85

Figure 4.5 BTCs with β = 0, 0.25, 0.5, 0.75 and 1. (a) FS model with α = 1.8; (b) FT model with γ = 0.8. 86

Figure 4.6 Relative mobile mass distributions at the end of each stage of the SWPP test using the ADE, FS (α =1.8) and FT (γ=0.8) models. (a): Mass distribution at the end of injection stage (t_{inj} = 10 hours); (b): Mass distribution at the end of chasing stage (t_{cha} = 3 hours); (c): Mass distribution at the end of resting stage (t_{rest} = 10 hours); (d): Mass distribution after 50 hours of pumping. 88

Figure 4.7 BTCs with different durations for injection, chasing and resting stages using the FTS model (α = 1.8, γ = 0.8) and the ADE model. (a) Injection duration t_{inj} = 10, 20 and 30 hours; (b) Chasing duration t_{cha} = 1, 3, 10 hours; (c) Resting duration t_{rest} = 10, 100 and 200 hours. Note that the BTCs of the ADE model overlap with each other in the resting stage in (c).....90

Figure 4.8 BTCs with Q_{pump} = 0.5, 1.5 and 4.5 m^3/hr using the FTS model (α = 1.8, γ = 0.8) and the ADE model. 91

Figure 4.9 BTCs with varying time-fractional index for each stage. 92

Figure 4. 10 Experimental data of the S1 and S2 tests and predicted BTCs by the FTS model. S1(left): FTS model with γ=0.8691 and α=1.9201; S2(right): FTS model with γ=0.8142 and α=1.9051. 94

Figure 4.11 Experimental data of Gouze et al. (2008) and predicted BTCs by the FTS model. Black solid: BTC from Gouze et al. (2008) with t_{inj}=4 min and t_{cha}=40 min; Red solid: FTS model with α=1.9 and γ=0.75; Red dashed: FTS model with α=1.8 and γ=0.7 96

LIST OF TABLES

Page

Table 3.1 Coefficients of a_i and b_i in equation (4) 34

Table 3.2 Model parameter and data assimilation setting 44

Table 4.2 Model settings for the validation of the FORMIM model and the FS model with $\alpha = 2$ 89

Table 4.3 Experimental data of S1 and S2 tests 93

Table 4.4 List of models developed for simulating SWPP tests 98

CHAPTER I

INTRODUCTION

Heat and chemical transport are two fundamental processes that are widely existed in the subsurface environments and come with natural phenomena (e.g., volcanic eruption, diurnal or seasonal temperature variation) or anthropogenic activities (e.g., well injection). A common characteristic of these two transport processes is they are both governed by the advection-dispersion equation (ADE) and both advective movements are impacted by the local heterogeneity of porous media. However, they still exhibit many different behaviors. For example, heat diffusivity in the solid matrix is usually two order of magnitude higher than the matrix diffusivity of chemicals. In addition, chemical transport usually comes with reaction and sorption. To investigate the characteristic behaviors of heat and chemical transport at different geological settings, this study focuses on three geological environments ranging from kilometer-scale to meter-scale, including volcanic hydrothermal system, shallow riverbeds where surface-water and groundwater exchange occurs and local fractured aquifer for well testing.

The contents of this work can be divided into three separate parts, corresponding to chapter II, III and IV, respectively. Chapter II investigates the relation between the heat and chemicals that are injected into the volcanic hydrothermal system during pulsatory magma degassing. A novel model was developed to quantitatively estimate the timing and duration of each degassing event in addition with the amount of heat and chemicals. Chapter III investigates how to estimate the hydrologic exchange flux

between surface water and groundwater using the high-resolution temperature time series collected at different depth in the riverbed. An ensemble data assimilation method, namely, Ensemble Smoother-Multiple Data Assimilation, was developed to estimate the daily and sub-daily flux. Chapter IV is about the anomaly transport behavior in fractured aquifer. A fractional model is developed to interpret the long-tailing behavior observed in pumping stage of single-well push-pull test.

CHAPTER II

THE INFLUENCE OF EPISODIC SHALLOW MAGMA DEGASSING ON HEAT AND CHEMICAL TRANSPORT IN VOLCANIC HYDROTHERMAL SYSTEMS

2.1. Introduction

The phreatic eruptions that occurred in 1976-1977 at La Soufrière of Guadeloupe led to the establishment of a comprehensive volcano-monitoring network by the "Observatoire Volcanologique et Sismologique de La Soufrière de Guadeloupe" (OVSG-IPGP). Thermal springs, fumaroles and acid ponds have been monitored since 1979, along with permanent monitoring of seismic events and deformation. Fumarolic activity on the summit vanished almost completely by 1981, and the temperature and geochemical anomalies (deviations from background) observed at the springs diminished gradually from 1979 to 1992. Some fumaroles were reactivated after 1992 and HCl-rich H_2O vapor reappeared in late 1997. Those phenomena imply intrusion of new magma around 1992 (Boichu et al., 2011; Villemant et al., 2014). The evidence of magmatic influence, such as observed geochemical anomalies at springs, continues today.

Past studies have demonstrated that the geochemical anomalies in the springs (Cl or He isotopes and the F/Cl/Br/I/S chemistry) are of magmatic origin (Villemant et al., 2005; Ruzié et al., 2012; Villemant et at., 2014; Li et al., 2015). The interpretation of

*Reprinted with permission from "The influence of episodic shallow magma degassing on heat and chemical transport in volcanic hydrothermal systems" by Chen, K., H. Zhan, E. Burns, S. E. Ingebritsen, P. Agrinier, 2018, *Geophys. Res. Lett.*, 45(7), 3068-3076, Copyright [2018] by Wiley.

spring temperature data has been more qualitative, in part due to lack of information about the subsurface structure, and in part because measureable temperature response occurs at only a few springs. However, understanding heat transport in the hydrothermal system is important since the thermal response reflects the input of magmatic fluid and mechanisms of eruption.

Recent geophysical surveys have greatly improved our understanding of the hydrothermal system, resulting in a physical model that describes the transport of both magmatic heat and chemicals (Zlotnicki et al., 2006; Rosas-Carbajal et al., 2016; Rosas-Carbajal et al., 2017). Using this new model, we expand upon the previous chemical model of Villemant et al. (2005) to demonstrate that joint quantitative analysis of heat and conservative tracers allows refined estimation of the post-eruptive degassing history of La Soufrière volcano. In addition, we analyze the combination of spring flow path properties and episodic heat flow that results in detectable thermal anomalies at springs.

2.2. Geological Setting

La Soufrière volcano is located on the island Basse Terre in Guadeloupe (Figure 2.1) and attains a maximum elevation of 1470 m above mean sea level (m.s.l.). Many thermal springs occur in or near the Cratère Amic structure, including Carbet Echelle (CE), Tarade (Ta), Bains Jaunes (BJ), Pas du Roy (PR), Galion (Ga), Ravine Marchand (RM) and Ravine Roche (RR), all of which are at high altitudes between ~950 m and ~1170 m above m.s.l. and at a maximum distance of 1.2 km from the summit (Fig. 1). Other more-distant springs, including Chute du Carbet (CC), Bains Chauds du Matouba (BCM) and Habitation Revel (HR), occur about 2-3 km from the dome.

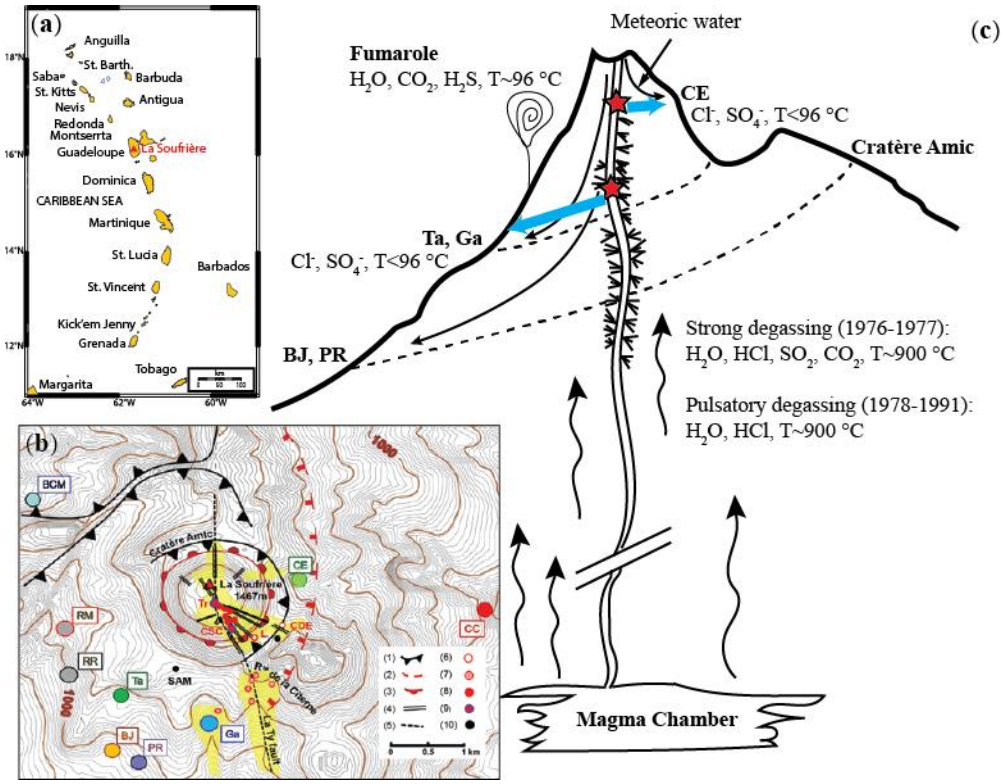

Figure 2.1 (a) Map showing the Caribbean volcanic arc with the location of La Soufrière volcano. (b) Contour map near the summit of La Soufrière volcano. Symbols in the contour map: (1) flank collapse scars; (2) La Grande Découverte Caldera; (3) La Soufrière dome; (4) summit fractures; (5) La Ty fault system; (6) 1976–1977 fumaroles active until 1981; (7) La Ty fumarolic field (weakly active until 1997); (8) summit fumaroles active since 1997; (9) fumaroles with intermittent acid lakes; (10) Savane à Mulets (SAM) and Col de l'Echelle (CDE) wells. The hydrothermally altered zone is yellow and thermal springs are indicated by large labeled circles (modified from Villemant et al., 2014). (c) Conceptual model for pulsatory degassing into near-surface aquifers at La Soufrière dome. Recharge occurs on the up-dip side of the hydrothermal alteration zones, with some possible recharge from the "meteoric water" lines. Red star, the zone of interaction between aquifer and volcanic gases; blue arrow, flow path; dashed line, outline of the deep hydrothermal system; solid line connecting magma reservoir and dome, eruptive conduit.

Springs exhibit a gradation in response as a function of distance from the volcano. Only the spring that is nearest to the summit, CE, exhibits both strong geochemical and temperature anomalies. Springs at intermediate distance, such as Ga

and BJ, capture much smoother Cl pulses (the result of dispersion), with a temperature response that is both lagged and significantly damped. The most distant springs, CC and BCM, show long-term thermal responses that may be confounded by regional hydrogeologic variation or climate variability, and only the CC spring exhibited the Cl response indicative of volcanic gas/vapor interaction. For the work herein, CE, Ga, and CC are selected for investigation of the role of time and distance on the thermal and Cl pulses, thereby representing a range of distances from degassing heat source to spring outflow (~ 75 m, ~650 m and ~2.5 km, respectively: Villemant et al., 2005).

The lava dome has been mapped geophysically, and individual aquifer flow horizons have been estimated for each spring, largely by mapping high electrical-conductivity pore-filling hydrothermal-alteration minerals that form impermeable layers that result in the perching and lateral flow of groundwater (Zlotnicki et al., 2006; Rosas-Carbajal et al., 2016; Rosas-Carbajal et al., 2017). A mapped 150 m-wide hydrothermally altered zone, with high electrical conductivity (larger than 1 S.m-1), lies about 150 m below the surface and is likely the main aquifer that transmits groundwater past the eruptive conduit to Ga spring (Zlotnicki et al., 2006; Rosas-Carbajal et al., 2016). The aquifers for springs CE and CC are likely more than 100 m below the surface. The average flow rate of Ga spring is 7.8 L/min between 1979 and 1995, and for spring CE, the average flow rate since 1995 is 7.1 L/min (Villemant et al, 2005). No flow rate data is available for spring CC. The average annual land surface temperature at the base of the lava dome is nearly constant at about 20 °C, and the thermal gradient in

the conductive domain beneath the hydrothermal systems is ~170 °C/km (Zlotnicki et at., 1992).

Fluid discharged from the spring is a combination of meteoric water and magmatic gases. Within the eruptive conduit (Figure 2.1c), high-temperature gas and vapor emission occurs in pulses, and is related to a two-step magma degassing process characterized by the initial rapid release of HCl-rich H_2O vapor during emplacement of new magma, followed by protracted release of gases and vapor at diminishing rates during crystallization of the newly emplaced magma (Boichu et al., 2008). This pulsatory magma degassing has previously been conceptualized as a series of instantaneous pulses that release hot gas and vapors (including HCl) to the overlying aquifer(s), causing observed thermal and geochemical anomalies, including a conservative Cl pulse (Villemant et al., 2005).

2.3. Conceptual Model and Method of Analysis

We assume that each aquifer discharging to a spring receives pulses of Cl and heat from the eruptive conduit at a discrete location under the volcano, after which Cl is transported conservatively. Heat is added conductively to the aquifer from below along the groundwater flow path, and the aquifer is insulated from the land surface above by the vadose zone. While the instantaneous chemical addition models of Villemant et al. (2005) ensure that the total Cl mass added is correct, instantaneous models require unrealistic infinite spikes in concentration/temperature near the zone of chemical/heat addition. Instead, we conceptualize the input pulses as square-waves with physically realistic magnitude where timing is the same for all springs and for both Cl and heat.

Use of a square-wave has two advantages. First, degassing is not instantaneous, resulting in a period of interaction with the aquifer which is now explicitly represented. Second, the amplitude of the heat pulse is constrained by the local boiling point (measured near the summit at the 96℃ boiling acid pond and fumaroles, which range between 94-120℃), where the process of boiling prevents groundwater temperature from being arbitrarily high, providing a constraint on pulse duration. The number of pulses, the starting times and duration, and the magnitude of the pulses were adjusted to calibrate the model to measurements. Magnitude of each Cl pulse was adjusted so that mass delivered as HCl balanced with measured Cl. A constant temperature of 96 °C was assumed for all pulses. This uniformly high temperature assumes that boiling and condensation of vapor is widespread within the part of the aquifer that is interacting with volcanic gases and vapors. Temperatures do not exceed boiling temperatures, because excess heat is consumed by the latent heat of vaporization.

Assuming single-phase lateral transport of chloride and heat in the aquifer simplifies calculations and is also consistent with the physics of the system as we understand it. Significant lateral chloride transport by a vapor phase is unlikely, because the volatility of chloride in low-pressure vapor is negligibly small. Lateral heat transport by a vapor phase will also be negligibly small, because of the large density contrast between liquid and vapor phases. The density contrast between liquid water and water vapor (a factor of about 10^3 at pressures of a few bars) dictates a strong tendency for subvertical upward vapor flow into the overlying unsaturated zone, so that vapor will tend to leave the system above where it is first generated. As some water vapor

condenses along its upward flow-path, condensate will tend to flow subvertically downward through the unsaturated zone, providing a narrow zone of contribution to the aquifer. Lateral flow of heavier-than-air noncondensible gases (dominated by CO_2) is physically possible in the unsaturated zone above the water table. However, the fumarole temperature – near the local boiling point for pure water – indicates minor CO_2 content; the vapor is likely >98% H_2O by mass. Despite the high water content of the vapor, measured spring flowrate and chemistry indicate that condensed vapor is a very small fraction of the total groundwater flowing beneath La Soufrière volcano (Villemant et al., 2014).

For heat transport, we consider both heat advection and dispersion within the aquifer along the flow path and conductive heat exchange between the aquifer and the vadose zone and basal layers (Burns et al., 2017). The governing equation for heat transport in the aquifer with multiple heat pulses is:

$$\Gamma_{aq}\frac{\partial T_{aq}}{\partial t}+u\rho_w c_w\frac{\partial T_{aq}}{\partial x}-\sigma_a\frac{\partial^2 T_{aq}}{\partial x^2}+\frac{\sigma_{vz}}{h_{aq}}\frac{\partial T_{vz}}{\partial z}\bigg|_{z=h_{vz}}-\frac{\sigma_{bu}}{h_{aq}}\frac{\partial T_{bu}}{\partial z}\bigg|_{z=h_{vz}+h_{aq}}=0\,, \quad (1a)$$

$$T_{aq}(x=0,t)=T_{r,j}(t), t\in[t_{j-1},t_j),\ j=1,2,...,P\,, \quad (1b)$$

where T is the temperature with "*aq*", "*vz*" and "*bu*" corresponding to aquifer, vadose zone and basal unit, respectively; Γ is the volumetric heat capacity; u is the groundwater flow velocity; ρ_w and c_w are the water density and specific heat, respectively; σ is the bulk thermal conductivity; h is the layer thickness; and $T_{r,j}$ is the temperature of pulses at the point of interaction between the groundwater and the volcanic gases. Temperature

alternates between hot pulse temperature and cool background temperature, and P is the number of periods used to define heat pulses. The heat exchange between the vadose zone and the aquifer occurs at $z=h_{vz}$ where $z=0$ is at the land surface, and the heat exchange between the basal unit and the aquifer is at $z= h_{vz}+h_{aq}$. The heat flow model is pseudo-2D, in that the one-dimensional sub-horizontal groundwater-flow along the aquifer is assumed to be well-mixed, and sub-vertical conductive heat exchange with the overlying and underlying geology is assumed to be orthogonal to groundwater-flow. Burns et al. (2016, 2017) provides an expanded discussion and limitations associated with this approach. Simulation results will be minimally sensitive to variations in vadose thickness, because vadose thickness is large compared with the heat penetration depth that occurs over the simulation period of a decade (~30 m), as estimated by the 1D conduction solution,

$$T_{vz} = \Delta T erfc(\frac{d}{2}\sqrt{\frac{\Gamma_{vz}}{\sigma_{vz} t}}) \ , \tag{2}$$

where ΔT is the step change of aquifer temperature and d is vertical distance away from the aquifer (Carslaw and Jaeger, 1986).

For Cl transport in the aquifer, we assume that Cl is conservative (i.e., no diffusion into the overlying/underlying geology and no chemical reactions), giving the one-dimensional equation for advection and dispersion along the flow path,

$$\frac{\partial C}{\partial t} + u\frac{\partial C}{\partial x} - D\frac{\partial C^2}{\partial x^2} = 0 \ , \tag{3a}$$

$$C(x=0,t) = C_{r,j}(t), t \in \left[t_{j-1}, t_j \right), \ j = 1, 2, ..., P \ , \tag{3b}$$

where D is the dispersion coefficient and $C_{r,j}$ is the constant concentration used to define pulses (alternating between pulse magnitude and background concentration). The transient solutions for heat transport and Cl transport are developed in the Appendix A, with the solutions given as equations (S20) and (S24).

For implementation of the solutions, other model assumptions include: (1) all three springs experience degassing pulses at the same time (in response to the same seismo-volcanic events), but chloride loading rate varies as a function of heterogeneous emplacement of magma and geology between magma and aquifers (i.e., total amount of Cl delivered to each flow path can vary); (2) the groundwater and hot fluid (gas/vapor/condensate mixture) are instantaneously well-mixed in the aquifer; (3) the groundwater flow rates are constant for the period of simulation 1979-1992 (Villemant et al., 2005); (4) the high-temperature gas/vapor mixtures increases the fluid temperature to the boiling point instantaneously; (5) the influence of variable fluid density, viscosity and specific heat is not significant. All model parameters were extracted from published values (Villemant et al., 2005; Eppelbaum et al., 2014; Villemant et al., 2014; Rosas-Carbajal et al., 2016), and are summarized in Table A1 of the Appendix A.

To calibrate the model, we adopt this workflow: (1) use a steady temperature distribution along each aquifer estimated by the steady solution of Burns et al. (2016) as the initial condition before pulsatory injection, allowing us to simulate background conductive geothermal heat flow into the aquifer along the groundwater flow path; (2) estimate the number and timing of Cl-pulses by matching the peak arrival times at each spring (because peak is a good indicator of advective flow); (3) estimate the duration for

each pulse to balance total heat delivered to CE spring assuming a constant 96 °C source temperature; (4) estimate Cl concentrations of individual pulses necessary to balance measured Cl concentration at springs.

Initial conditions were developed by estimating long term temperature and Cl conditions at the springs. The lowest Cl values are assumed to be approximately the background steady value. Similarly, because degassing adds heat, the lowest temperatures were used to estimate long-term background temperature. Background conductive heat flow from beneath the aquifer is estimated to be 0.34 W/m^2 by using the measured thermal gradient of Zlotnicki et al. (~170 °C/km, 1992), and a representative value of thermal conductivity for andesite (1.97 W/mK, Eppelbaum et al., 2014).

2.4. Results

The long-term steady background spring temperatures (i.e., no influence of degassing pulses) are estimated to be 21 °C, 38 °C and 43 °C for CE, Ga and CC springs, respectively, under the assumptions that the 1976 phreatic eruption did not yet have a strong thermal effect on the two longer flow-path springs (Ga and CC) by 1979, and that by 1991, the CE spring temperature was asymptotically trending towards background temperature. Using the estimated basal heat flow (0.34 W/m^2) and the long-term steady background spring temperatures, background groundwater inflow temperatures at the eruptive conduit (i.e., no influence of degassing pulses) were computed to be 20.5 °C, 35.6 °C and 37.5 °C, for CE, Ga, and CC springs flow-paths, respectively.

To represent the period of decreasing volcanic activity after 1976, we used 26 square waves to match the measured 1979-1992 thermal and chemical response at the springs (Figure 2.2a, Table S2). For our analysis, a single relatively long-duration one-year pulse was used to represent the phreatic eruption, perturbing the long-term steady chloride and temperature values and giving a good match to the conditions when measurements started in 1979. It is possible that multiple degassing events occurred before 1979, and that the effect of such degassing events in terms of thermal response at the springs would be equivalent to an individual pulse that lasts for about one year.

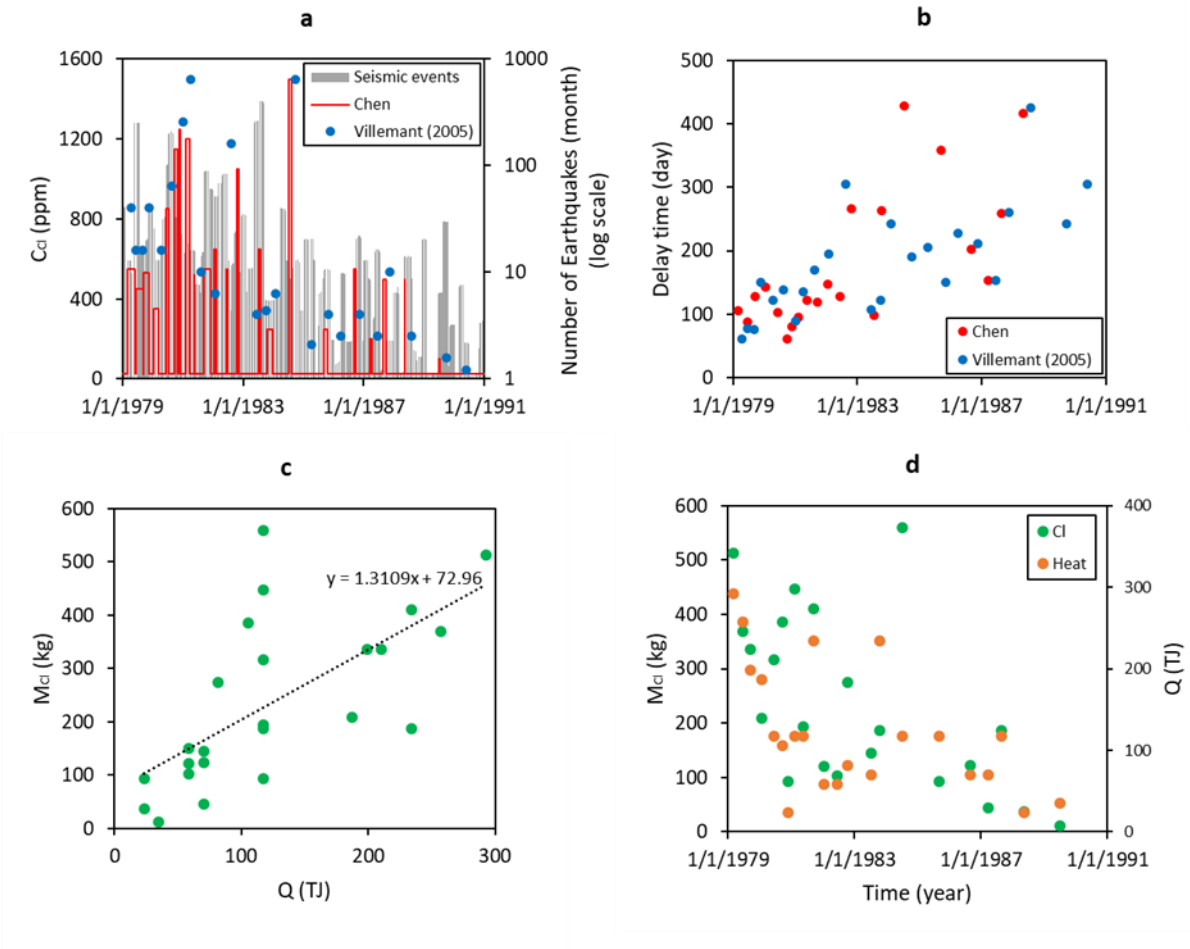

Figure 2.2 Comparison between the square-wave chloride source (Chen, this study) and instantaneous-source used by Villemant et al. (2005), and estimated Cl mass and amount of heat in individual pulses. (a) Plot showing that Cl pulse concentration estimated by the current study and Villemant et al. (2005) are generally correlated with seismicity and each other, Red line: the square-wave chloride pulses. Blue dot: instantaneous sources (scaled for comparison to a similar range as the square wave) inferred by Villemant et al. (2005). Gray line: number of detected earthquakes for comparison with degassing loading; (b) The time between the starting points of successive square-wave pulses showing that pulse frequency decreases over time; (c) Cross-plot of the Cl mass M_{Cl} (kg) and amount of heat Q (TJ) delivered in individual pulses, showing that heat and Cl delivered in each pulse is correlated, where M_{Cl} = flow rate × pulse duration × pulse concentration and Q = volumetric heat capacity of water × flow rate × pulse duration × (local boiling temperature – background recharge temperature); (d) plot of M_{Cl} and Q delivered in individual pulses over time, showing the decrease in heat and Cl delivered by individual pulses over time.

Our results are similar to those of Villemant et al. (2005), who for the same 1979-1992 period used 27 instantaneous Cl pulses to estimate the timing of degassing events and total chloride introduced to the aquifers. Both sets of results display a reduction in frequency of degassing events over time (Figure 2.2b) and less addition of chloride to the aquifers over time. The mass of Cl introduced in an individual pulse is proportional to the amount of heat in the same pulse (Figure 2.2c), and there is a decreasing trend in mass and heat delivered by individual pulses over time (Figure 2.2d).

Figure 2.3a shows measured and the new simulated chloride concentrations for CE, Ga and CC springs, and Figure 3b shows corresponding measured and simulated temperature. Compared to the previous method of using instantaneous Cl spikes to understand transport to springs (Villemant et al., 2005), jointly simulating the breakthrough of temperature and Cl estimates the duration of degassing pulses and also provides physically realistic values of temperature and Cl at all points within the aquifers. By definition, instantaneous spikes require arbitrarily high concentrations and temperatures to deliver the correct amount of total mass and heat, respectively. However, because the upper limit of aquifer temperature is constrained by boiling/condensation, minimum pulse duration is well-defined by the total heating necessary to replicate measured spring temperatures, given this upper limit temperature. Because Cl is conservative, the center of the square wave is well-constrained (within ~0.01 years). Using the pulse duration estimated from the temperature signal, the measured total mass of Cl is used to estimate the magnitude of the Cl pulse.

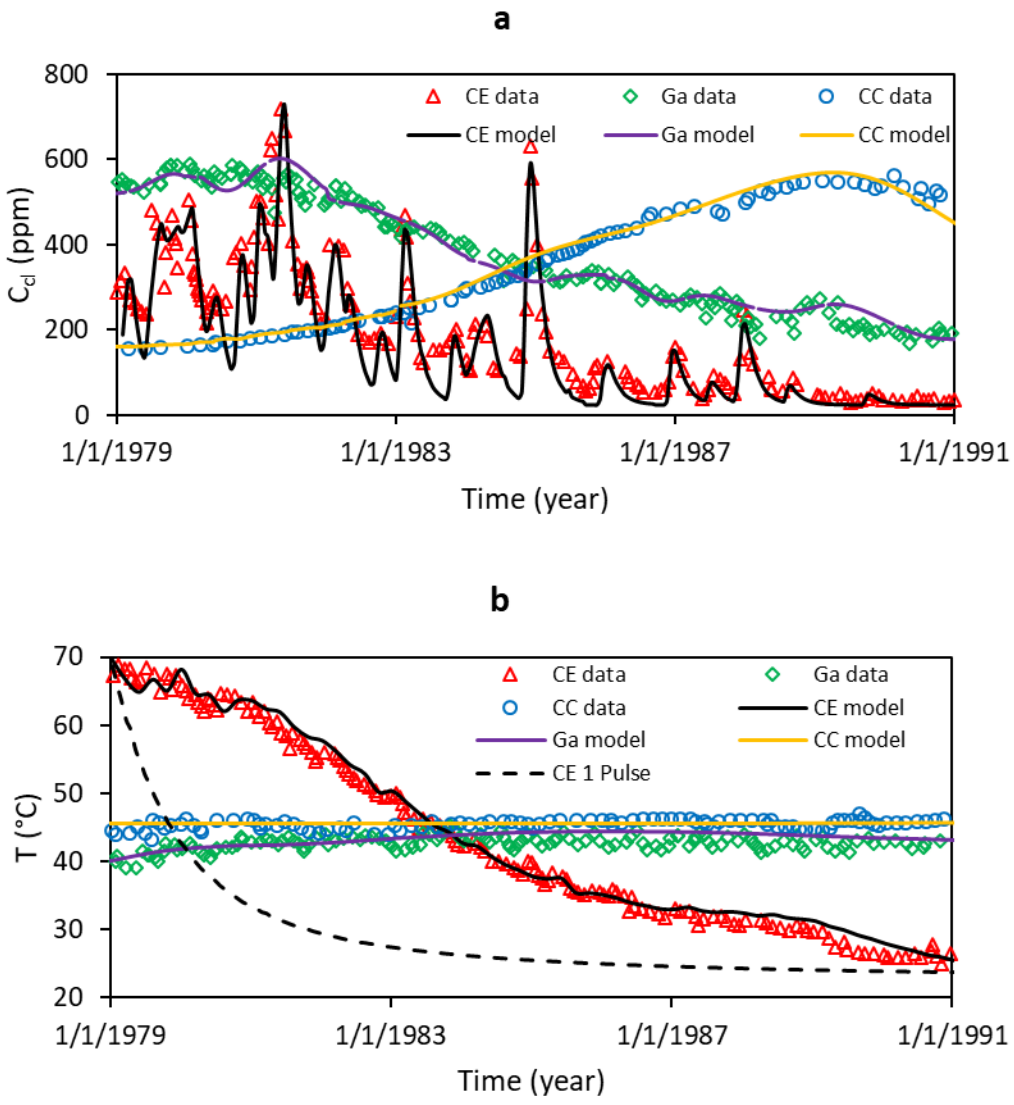

Figure 2.3 Measured and simulated Cl concentrations and temperatures at springs of CE (proximal to the summit, ~75 m distant), Ga (intermediate to the summit, ~650 m) and CC (distal to the summit, ~2800 m). (a) CE spring Cl concentration responds quickly to the degassing activity (~3 months' delay) and the delay times for Ga and CC spring are ~2.1 years and ~9 years, respectively. (b) Measured and simulated temperature: CE spring temperature decays with the decreasing pulse frequency; Ga spring temperature increases ~3 °C from 1979 to 1982 and then remains constant; CC spring temperature is constant at 45 °C from 1979 to 1991. Dashed line: Simulated CE spring temperature assuming no episodic degassing pulse heating except the heating from the first one-year pulse. The difference between the CE solid and dashed lines is the result of heat pulses to the aquifer from degassing.

CE spring is very sensitive to pulsatory degassing (Figure 2.3a), and individual past degassing events are recorded in the peaks of the Cl time-series (i.e., the memory effect of Villemant et al., 2005). The temperature record has even longer memory (Figure 3b), with temperature constraining estimates of pulse duration, and with conductive heat exchange resulting in lagged and damped long-term response to degassing episodes. The Cl concentration data from CE spring cannot help us infer degassing activity before 1979 due to the short system memory resulting from rapid advection of a conservative tracer (~3 month advective travel time, obtained from the ratio of the aquifer length to groundwater velocity). For Ga spring, with a memory of ~2.1 year, the first peak of the Cl time-series reflects degassing activity as early as 1976-1977. Note that due to the longer transit time, while individual peaks are still discernable, the overall Cl response is starting to resemble a single large broad bulge, where dispersion is merging individual pulses. The broad decline in Cl concentration over the period 1979-1992 reflects both the reduction in pulse frequency and in individual pulse Cl concentration (Fig. 2.2d). At CC spring, with an advective time of ~9 years, the Cl peak is correspondingly later in time, and the curve is even smoother than for Ga due to the additional dispersion over distance and time.

Temperature at springs is lagged and damped due to conductive heat exchange with the overlying and underlying geology. Figure 3b displays the observed and modeled temperature curves for the three springs with all degassing pulses applied at 96 °C over the same durations as the Cl pulses. Damping of the thermal signal is partly the result of the time-lag physics, but also heat loss to ambient conditions, so that total heat

arriving at the spring is less than the pulsatory heat addition to groundwater (i.e., heat is not conservative). The simulated temperature for the proximal CE spring matches the measurements well, supporting the conceptual models of heat delivery and transport, and demonstrating that temperatures exceeding the boiling point are not required to explain the temperature signal at springs. The reasonable match to temperature for all three springs demonstrates the importance of flow path length on controlling thermal signals.

To underscore the importance of total heat added by pulses, temperature was simulated at CE spring assuming there were no heat pulses following the 1976-1977 phreatic eruption (dashed line on Figure 2.3b). The difference between the solid and dashed lines for CE spring shows the influence of pulsatory heating, and the area between the curves is the difference in heat delivered to the spring as a result of degassing pulses.

Whether a pulse is a single long pulse, or a series of pulses closely spaced in time, the resulting heat signal at springs will be lagged and damped, possibly to the point of being undetectable. For La Soufrière springs, because pulse temperatures are constrained to be ~96 °C, the recorded temperature at each spring is only a function of duration of the pulse. Figure 4a displays BTCs for a range of pulse durations using the hydrogeologic setting of Ga spring. The 1-year pulse peak is weakened by more than 95% at the Ga spring. The longer the pulse duration, the larger the amplitude and the longer it takes for the disturbed temperature to return to steady state. The Cl responses at CE and Ga springs are much stronger than the heat responses, which are weakened by conduction to adjacent layers over the long flow paths (Fig. 2.3b). Figure 2.4b shows

temperature profiles along the groundwater flow path contributing to Ga spring at different times for both 10-year and 100-year pulses. For the 100-year pulse, the temperature at Ga spring continuously increases throughout the 100 year period. Conversely, for the 10-year pulse, the spring temperature first increases and then decreases. The 30-year profile for the 10-year pulse shows the effects of damping and translation along the groundwater flow-path after the pulse is discontinued. The 100-year profile for the 10-year pulse shows additional damping and translation, and shows that heat stored from a 10-year pulse will have lasting but relatively small effects on spring temperature.

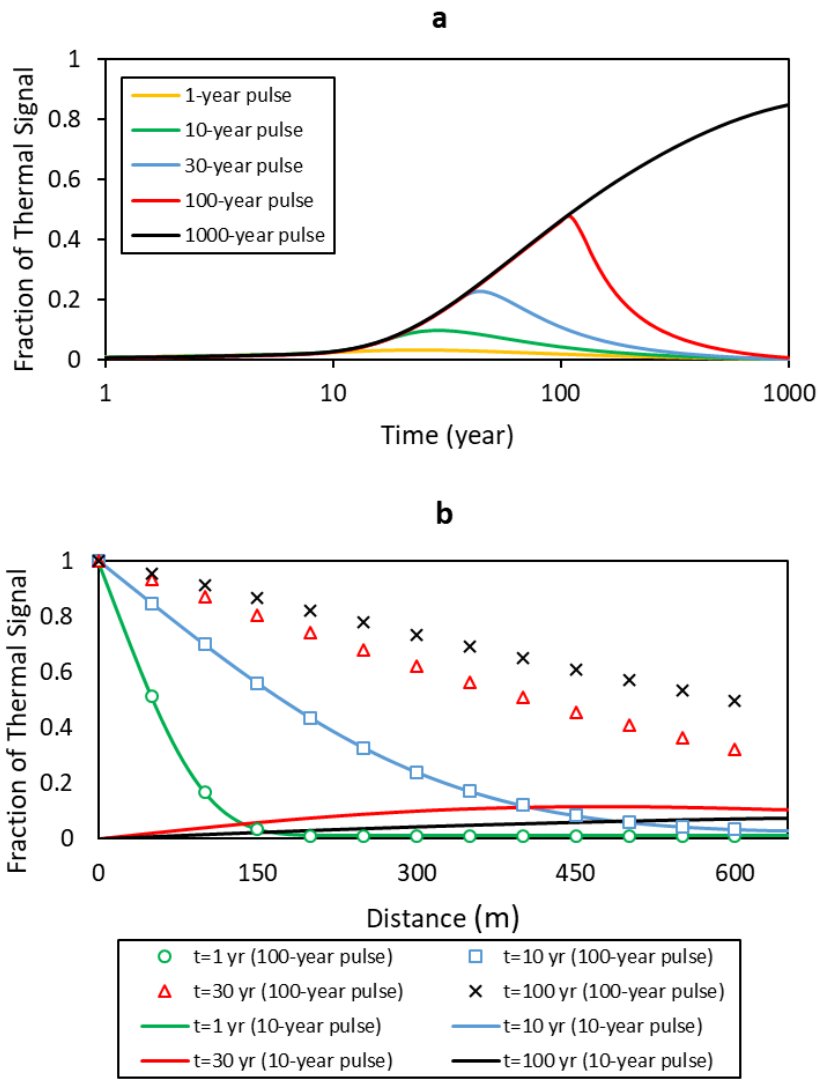

Figure 2.4 BTCs and temperature profiles generated for different heat pulse durations using the model for Ga spring (x = 650 m). Fraction of thermal signal = (observed temperature at x – steady temperature at x) / (local boiling temperature - steady temperature at x). (a) BTCs at Ga spring with 1-, 10-, 30-, 100- and 1000-year pulse duration. After 1000 years the full thermal signal has not reached the Ga spring despite having an estimated advective travel time of ~2.1 years; b) The distribution of temperature along the groundwater flowpath at four different times, 1-, 10-, 30- and 100-year, resulting from two different pulse durations. The 10-year pulse is shown with solid lines, and the 100-year pulse is shown with discrete symbols. For times less than 10 years, the profiles are identical. Between 10 and 100 years, temperatures continue to rise for the 100-year pulse, but the 10-year pulse quickly damps and translates towards the spring (distance = 650 m).

2.5. Discussion and Conclusions

Our model demonstrates that a single sequence of magma degassing events following the 1976-1977 phreatic eruption can explain the observed geochemical and temperature signals for a range of La Soufrière springs. The chloride time-series records episodic degassing events, with lag times consistent with measured spring flow rates. Relative to chloride, heat is significantly lagged and damped, and for short-duration degassing events, thermal responses will not be detectable at distal springs.

While the physical model of the cycle of magma cooling, crystallization and degassing has been previously developed and is correlated to the time-series of Cl observed at springs, the transport process of the volatiles between the starting point, magma, and the ending point, spring, is less well known (Villemant et al., 2005, Boichu et al., 2008; Boichu et al., 2011). Our model partially fills the gap by demonstrating that limited-duration pulses with physically realistic rates of exchange between vapor and aquifers can explain measured spring responses. Because aquifer temperature must be at or below boiling, including spring temperature in our analysis provided a constraint on degassing pulse minimum duration.

The basal conductive heat flux beneath the volcano is estimated to be about 0.34 W/m^2 based on the measured geothermal gradient, which is in the range of reasonable values (e.g., Morgan et al., 1977; Ingebritsen et al., 1989; Blackwell et al., 1990; Hochstein,1995; Williams and DeAngelo, 2008, 2011; Burns et al., 2017). The regional heat flux on the crest of the Lesser Antilles arc, 0.1 W/m^2 (Manga et al., 2012), is much lower than that nearer the volcano, where it is elevated by conduction from the

underlying magma reservoir. During degassing events heat delivered to groundwater advectively by vapors is much larger than conductively delivered heat flow, and the total amount of heat delivered from individual degassing events can be estimated from the duration and magnitude of the thermal input pulses.

We developed a semi-analytic solution to transport of Cl and heat in La Soufrière volcano's hydrothermal system that assumes geothermal heating of groundwater from recharge areas to springs, allowing us to evaluate the influence of episodic heating in a narrow region of interaction. During periods of magma degassing, heat is added to groundwater via interaction with volcanic gases and vapor as groundwater flows beneath the volcanic dome. Considering Cl and heat together allows us to define a single set of degassing events (i.e., pulse durations) that explains spring response for both Cl and temperature as a function of distance from the dome. Further, the resulting set of degassing pulses does not require physically unreasonable values of temperature or Cl at any location within the hydrothermal system.

References

Carslaw H. S. and Jaeger, J. C. (1986), Conduction of Heat in Solids, Clarendon Press, Oxford, United Kingdom.

Blackwell, D. D., J. L. Steele, S. Kelley, and M. A. Korosec (1990), Heat flow in the state of Washington and thermal conditions in the Cascade range, *J. Geophys. Res.*, *95*(B12), 19, 495-19,516.

Boichu, M., B. Villemant, and G. Boudon (2008), A model for episodic degassing of an andesitic magma intrusion, *J. Geophys. Res.-Sol. Ea.*, *113*(B7).

Boichu, M., B. Villemant, and G. Boudon (2011), Degassing at La Soufriere de Guadeloupe volcano (Lesser Antilles) since the last eruptive crisis in 1975-77: Result of a shallow magma intrusion?, *J. Volcanol. Geoth. Res.*, *203*(3-4), 102-112.

Burns, E. R., S. E. Ingebritsen, M. Manga, and C. F. Williams (2016), Evaluating geothermal and hydrogeologic controls on regional groundwater temperature distribution, *Water Resour. Res.*, *52*(2), 1328-1344.

Burns, E. R., Y. H. Zhu, H. B. Zhan, M. Manga, C. F. Williams, S. E. Ingebritsen, and J. B. Dunham (2017), Thermal effect of climate change on groundwater-fed ecosystems, *Water Resour. Res.*, *53*(4), 3341-3351.

Eppelbaum L., L. Kutasov and A. Pilchin (2014), Applied Geothermics, Springer Berlin Heidelberg.

Feuillard, M., C. J. Allegre, G. Brandeis, R. Gaulon, J. L. Lemouel, J. C. Mercier, J. P. Pozzi, and M. P. Semet (1983), The 1975-1977 Crisis of La Soufriere De Guadeloupe (F.W.I.) - a Still-Born Magmatic Eruption, *J. Volcanol. Geoth. Res.*, *16*(3-4), 317-334.

Hochstein, M. P. (1995), Crustal heat transfer in the Taupo Volcanic Zone (New Zealand): Comparison with other volcanic arcs and explanatory heat source models, *J. Volcanol. Geotherm. Res.*, *68*, 117-151.

Ingebritsen, S. E., D. R. Shelly, P. A. Hsieh, L. E. Clor, P. H. Seward, and W. C. Evans (2015), Hydrothermal response to a volcano-tectonic earthquake swarm, Lassen, California, *Geophys. Res. Lett.*, *42*(21), 9223-9230.

Ingebritsen, S. E., D. R. Sherrod, and R. H. Mariner (1989), Heat flow and hydrothermal circulation in the Cascade range, north-central Oregon, *Science*, 243, 1458-1462.

Li, L., M. Bonifacie, C. Aubaud, O., Crispi, C. Desset, and P. Agrinier (2015), Chlorine isotopes of thermal springs in arc volcanoes for tracing shallow magmatic activity, *Earth Planet. Sci. Lett.*, 413, 101-110.

Manga, M., M. J. Hornbach, A. L. Friant, O. Ishizuka, N. Stroncik, T. Adachi, M. Aljahdali, G. Boudon, C. Breitkreuz, A. Fraass, A. Fujinawa, R. Hatfield, M. Jutzeler, K. Kataoka, S. Lafuerza, F. Maeno, M. Martinez-Colon, M. McCanta, S. Morgan, M. R. Palmer, T. Saito, A. Slagle, A. J. Stinton, K. S. V. Subramanyam, Y. Tamura, P. J. Talling, B. Villemant, D. Wall-Palmer and F. Wang (2012), Heat flow in the Lesser Antilles island arc and adjacent back arc Grenada basin, *Geochem. Geophys.*, 13(8).

Morgan, P., D. D. Blackwell, R. E. Spafford, and R. B. Smith (1977), Heat flow measurements in Yellowstone Lake and the thermal structure of the Yellowstone Caldera, *J. Geophys. Res.*, 82(26), 3719-3723.

Rosas-Carbajal, M., J. C. Komorowski, F. Nicollin, and D. Gibert (2016), Volcano electrical tomography unveils edifice collapse hazard linked to hydrothermal system structure and dynamics, *Sci. Rep.*, 6(29899).

Rosas-Carbajal, M., K. Jourde, J. Marteau, S. Deroussi, J. C. Komorowski, and D. Gibert (2017), Three-dimensional density structure of La Soufriere de Guadeloupe lava dome from simultaneous muon radiographies and gravity data, *Geophys. Res. Lett.*, *44*(13), 6743-6751.

Ruzie, L., M. Moreira, and O. Crispi (2012), Noble gas isotopes in hydrothermal volcanic fluids of La Soufriere volcano, Guadeloupe, Lesser Antilles arc, *Chem. Geol*., *304*, 158-165.

Villemant, B., G. Hammouya, A. Michel, M. P. Semet, J. C. Komorowski, G. Boudon, and J. L. Cheminee (2005), The memory of volcanic waters: Shallow magma degassing revealed by halogen monitoring in thermal springs of La Soufriere volcano (Guadeloupe, Lesser Antilles), *Earth Planet. Sci. Lett.*, *237*(3-4), 710-728.

Villemant, B., J. C. Komorowski, C. Dessert, A. Michel, O. Crispi, G. Hammouya, F. Beauducel, and J. B. De Chabalier (2014), Evidence for a new shallow magma intrusion at La Soufriere of Guadeloupe (Lesser Antilles) Insights from long-term geochemical monitoring of halogen-rich hydrothermal fluids, *J. Volcanol. Geoth. Res.*, *285*, 247-277.

Williams, C. F., and J. DeAngelo (2008), Mapping geothermal potential in the western United States, *Trans. Geotherm. Resour. Counc.*, *32*, 181-188.

Williams, C. F., and J. DeAngelo (2011), Evaluation of approaches and associated uncertainties in the estimation of temperatures in the upper crust of the western United States, *GRC Trans.*, *35*, 1599-1605.

Zlotnicki, J., G. Boudon, and J. L. Lemouel (1992), The volcanic activity of La Soufriere of Guadeloupe (Lesser Antilles) - structural and tectonic implications, *J. Volcanol. Geoth. Res.*, *49*(1-2), 91-104.

Zlotnicki, J., G. Vargemezis, A. Mille, F. Bruere, and G. Hammouya (2006), State of the hydrothermal activity of Soufriere of Guadeloupe volcano inferred by VLF surveys, *J. Appl. Geophys.*, *58*(4), 265-279.

CHAPTER III

USING ENSEMBLE DATA ASSIMILATION TO ESTIMATE TRANSIENT HYDROLOGIC EXCHANGE FLUXES UNDER HIGHLY DYNAMIC FLOW CONDITIONS

3.1 Introduction

Hydrologic exchange flow (HEF), including both vertical flow through riverbed and lateral flow through bank sediments, has gained much attention among the river corridor research community in recent years due to the significant impact of HEF on the biogeochemical process of carbon and nutrients cycling (Kiel and Cardenas, 2014; Gomez-Velez et al., 2015; Harvey and Gooseff, 2015; Kaufman et al., 2017). For the two directions of exchange flow, vertical HEF (HEF) has been demonstrated to have a much greater impact on the denitrification process compared with lateral exchange (Gomez-Velez et al., 2015). How to quantify the HEF and relate the flux to the biogeochemical process is a challenge, which has stimulated the development of many hydrogeophysical methods for flux measurements.

The methods to estimate the flux across the riverbed can be grouped into three categories, including direct measurement using seepage meter, heat tracer methods and Darcy's law based methods (Kalbus et al. 2006). Traditional seepage meter is designed to directly measure the flux based on water balance equation, but the performance of using collection bag to estimate the water accumulation or loss in a certain time interval is affected by the moving river water and the mixed grain size (Rosenberry, 2008;

Harvey and Gooseff, 2015). Some other instruments are therefore deployed to replace the collection bag such as ultrasonic meter, electromagnetic meter and so on (Paulsen et al., 2001; Rosenberry and Morin, 2004). Heat tracer method is popular in recent years due to the low cost and well-developed theory (Hatch et al., 2006; Keery et al., 2007; Rau et al., 2010; McCallum et al, 2012; Luce et al, 2013). However, the assumption of steady flow in one dimension and the signal processing technique for the extracting of diurnal heat signal cause concern in field application as the diurnal heat signal is impacted by the complex and heterogeneous flow field (Lautz 2010; Irvine and Lautz, 2015; Rau et al., 2015). In addition, the heat tracer method uses the daily averaged diurnal signal to infer the flux, which cannot capture the highly dynamic (e.g. sub-hourly) flux information. The Darcy's law method is physics-based that links the Darcy's flux with the hydraulic gradient and hydraulic conductivity. Hydraulic gradient can be obtained through the monitored head difference in the riverbed. Hydraulic conductivity can be either measured in the laboratory or the field using the traditional test methods like constant-test head or slug test. The magnitude of hydraulic conductivity could change over several order of magnitude at small reach scale, which makes the estimation of spatial flux challenging (Cardenas and Zlotnik, 2003; Lautz and Siegel, 2006; Naganna and Deka, 2018). Some resent attempts include using the predictive relation between the streambed temperature and modeled flux to estimate the spatial flux or assimilating the distributed temperature sensing (DTS) data to calculate the flux based on an empirical thermal-mixing model (Lautz and Ribaudo, 2012; Huang, 2016). Most efforts that using Darcy's law to estimate flux implicitly assumes that the

hydraulic conductivity is a static value. This assumption is valid for the point-of-time measurement when the water temperature does not change too much within diurnal temperature cycle. However, for the long-term estimation of flux, the hydraulic conductivity is expected to be strongly impacted by fluid temperature variation due to the reciprocal relation between temperature and viscosity (Constantz and Murphy, 1991; Constantz, 1998). Cardenas and Wilson (2007) pointed out that the thermal-induced fluid viscosity variation could significantly change the magnitude of hyporheic flux. This fact calls attention to the current methods that is developed to estimate the HEF, especially for the long-term monitoring of hyporheic flux.

The ensemble-based data assimilation technique is an effective method to estimate model parameters with the advantage of low computational cost compared with the full Bayesian approaches (Evenson, 2009; Chen et al., 2012; Chen et al., 2013). Ensemble Kalman filter (EnKF), a sequential data assimilation technique, along with many of its variants are introduced into the petroleum and hydrology field to estimate the model states (e.g. pressure, saturation) and parameters (e.g., hydraulic conductivity, porosity) (Evenson 1994; Evensen,2003; Oliver and Chen,2011). The computational advantage of EnKF might be not obvious when a large quantity of data is encountered due to the frequent restart of forward simulation at the time point when data is collected. Ensemble smoother (ES) is an alternative of EnKF that assimilates all data simultaneously and then updates the model parameters after a one-time forward simulation (van Leeuwen and Evensen, 1996). This method avoids restart of forward simulation, thus it reduces time cost but with the sacrifice of computational accuracy.

Emerick and Reynolds (2012; 2013) proposed the iterative form of ES, namely, ES-Multiple Data Assimilation (ES-MDA), to improve the accuracy. A common application of data assimilation technique in hydrology field is using the observed hydraulic head, temperature data or tracer concentration to estimate the hydraulic conductivity field, of which the hydraulic conductivity is treated as time-invariant model property (Chen and Zhang, 2006; Chen et al., 2013; Kurtz et al., 2013; Ju et al., 2018). Again, this implicit assumption that hydraulic conductivity is time-invariant cannot be applied to the hyporheic flow research. In fact, what should be time-invariant is the intrinsic permeability instead of the hydraulic conductivity. Dynamic hydraulic conductivity that is closely related with fluid temperature needs to be considered while estimating the hydraulic conductivity in the hyporheic zone.

The objective of this study is to develop a data assimilation-based approach to estimate the highly dynamic HEF using the observed hydraulic heads and temperature in the riverbed during long term monitoring. The unique contribution of this proposed method is it overcomes two deficiency of heat tracer method. First is our method can capture sub-daily HEF, unlike heat tracer method which cannot capture highly dynamic flux information. Second is our method is physics-based thus strong groundwater upwelling observed in our study site with temperature that is significantly different from the river temperature would not affect the method performance. However, heat tracer method would fail in this situation because the greatly damped diurnal signal is unidentifiable during upwelling. In addition, the time-variant hydraulic conductivity correlated with the seasonal change of temperature is considered to give an accurate

estimation of HEF, which is often underestimated or overestimated with a single field measurement of hydraulic conductivity for long term estimation.

3.2. Methodology

3.2.1 Study site

Our study site is at the 300 Area of the U.S. Department of Energy Hanford site located in southeastern Washington State, adjacent to the Columbia River. The river stage along the reach is regulated by the upstream Priest Rapids Dam for hydroelectric power generation, with an average daily fluctuation of ~0.5 m and annual fluctuations at 2-3 m (Zachara et al. 2016; Zhou et al., 2017). River stage fluctuations at this magnitude and frequency lead to extremely dynamic exchange flows between the river and groundwater aquifer, which consequently have strong impacts on the hyporheic thermal regime and biogeochemical processes (Song et. al, 2018).

A pressure transducer logger was installed since 2001 for long-term monitoring of the hourly river stage, temperature and specific conductance. One thermistor was installed in July, 8, 2016 to record the riverbed temperature every 5 minutes at the depths of +0.16 m, -0.04 m, -0.24 m and -0.64 m, where plus and minors sign indicate above and below the surface of the riverbed, respectively (Figure 3.1). In addition, four piezometers and one river gauge (RG3) were installed near the thermistor to monitor the

hydraulic heads at different depth and river stage, respectively.

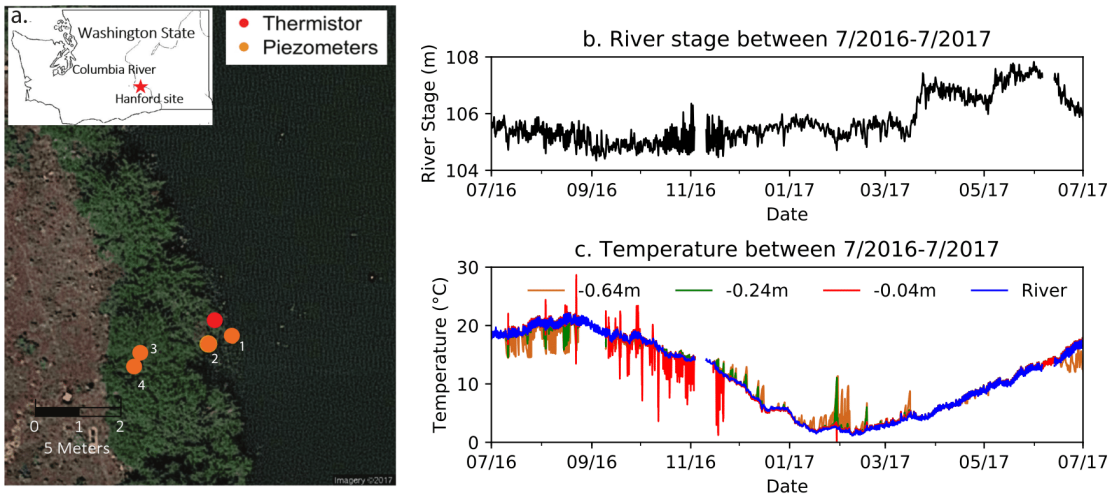

Figure 3.1 Location map and collected data. a. The field site at Hanford 300 area where the thermistor, piezometers and the river gauge are installed. b. River stage between 7/2016 and 7/2017. Note that there is a 7-days gap in early Nov., 2016 and early June, 2017. c. River temperature and subsurface temperatures at depths -0.04 m, -0.24 m and -0.64 m between 7/2016 and 7/2017. Note that upwelling of cold groundwater and hot groundwater are observed in summer and winter, respectively.

3.2.2 Forward simulation-PFLOTRAN

The simulator used in this study is PFLOTRAN, a massively parallel reactive flow and transport open source code, which has the capability of modeling the hydro-thermal-chemical transport in saturated and unsaturated zone. The Thermal-Hydrologic (TH) module of PFLOTRAN is chosen in this study to model the single phase, saturated and nonisothermal flow and transport in the saturated sediments of riverbed. The governing equation for mass and energy transport are,

$$\frac{\partial}{\partial t}(\varphi s \eta) + \nabla \cdot (\eta \mathbf{q}) = Q_w \ , \qquad (1)$$

$$\frac{\partial}{\partial t}\left[\varphi s\eta U + (1-\varphi)\rho_r c_p T\right] + \nabla\cdot(\eta \mathbf{q} H - \kappa\nabla T) = Q_e \ , \tag{2}$$

where φ is the porosity; s is the saturation; η is the molar density; $\mathbf{q}$ is Darcy flux; Q_w and Q_e are source/sink term for mass and energy transport, respectively; U and H are the internal energy and enthalpy of the fluid, respectively; ρ_r is rock density; c_p and κ are the heat capacity and thermal conductivity of the porous media, respectively.

According to the different forms of Darcy's law, the hydraulic conductivity for single phase flow could be expressed as,

$$K = \frac{k\rho_w g}{\mu_w} \ , \tag{3}$$

where *K* is hydraulic conductivity, *k* is intrinsic permeability, ρ_w is water density, *g* is gravitational constant and μ_w is water viscosity. Among those factors, *k* is the property that is determined by the particle size and pore structure. Water density is impacted by pressure and temperature theoretically, but the deviation to the value 997 kg/m^3 (at 25 °C and atmospheric pressure) is usually small for the river reach environment and thus is often treated as a constant value. The thing is different for water viscosity. Water viscosity is sensitive to the temperature in the range of seasonal river temperature variation. A simplified correlation between temperature and liquid water at standard pressure of 0.1 MPa is (Huber et.al, 2009),

$$\mu_w = \mu_0 \sum_{i=1}^{4} a_i (T/300)^{b_i} \ , \tag{4}$$

Table 3.1 Coefficients of a_i and b_i in equation (4)

i	a_i	b_i
1	280.68	-1.9
2	511.45	-7.7
3	61.131	-19.6
4	0.45903	-40

where μ_0 is the reference viscosity $1\times10^{-6}\,\mathrm{Pa\cdot s}$; T is the liquid water temperature with unit K; a_i and b_i are coefficients given in Table 1. This correlation works for the temperature range 253.15 K$\leqslant T\leqslant$383.15 K. The exponential relation between the water viscosity and temperature indicates that the viscosity could vary a lot even in a small temperature range, and the fact is the viscosity can vary more than 50% between the normal range of river temperature, 1 °C- 25 °C, at our study site. Therefore, hydraulic conductivity in the riverbed is intrinsically a time-variant value that needs to be correlated with temperature while using.

3.2.3 Ensemble Smoother with Multiple Data Assimilation (ES-MDA)

ES-MDA is the iterative form of ES that overcomes the inaccuracy problem of ES due to the single update of parameters by assimilating all data simultaneously. The analysis equation of ES-MDA is similar to that of ES except adding an inflation term to the covariance matrix of measurement error to damp the changes in the model at early iteration (Emerick and Reynolds, 2013). The analysis equation of ES-MDA is,

$$\mathbf{m}_j^a = \mathbf{m}_j^f + \mathbf{C}_{MD}^f(\mathbf{C}_{DD}^f + \alpha_i\mathbf{C}_D)^{-1}(\mathbf{d}_{obs} + \sqrt{\alpha_i}\mathbf{C}_D^{1/2}\mathbf{z}_d - \mathbf{d}_j^f)\ , \qquad (5)$$

for j = 1, 2,…, N_e, where N_e is the number of ensemble realizations; $\mathbf{m}_j^a$ and $\mathbf{m}_j^f$ are the jth N_m-dimension analyzed and forecast vector of model parameters, respectively; $\mathbf{C}_{MD}^f$ is the $N_m \times N_d$-dimension cross-covariance matrix between the vector of model parameters, $\mathbf{m}^f$, and the vector of predicted data, $\mathbf{d}^f$, where N_d is the number of measurements or predicted data; $\mathbf{C}_{DD}^f$ is the $N_d \times N_d$-dimension auto-covariance matrix of predicted data; α_i is the variance inflation coefficient for ith iteration; $\mathbf{C}_D$ is the $N_d \times N_d$-dimension auto-covariance matrix of observed data measurement errors; $\mathbf{d}_{obs}$ is the N_d-dimension vector of observed data; $\mathbf{z}_d \sim (0, \mathbf{I}_{N_d})$ and $\mathbf{d}_j^f$ is the jth N_d-dimension vector of predicted data. The series of inflation coefficient α_i needs to satisfy the following equation,

$$\sum_{i=1}^{N_e} \frac{1}{\alpha_i} = 1 , \tag{6}$$

of which a common setting is letting α_i be equal to the number of iterations.

In this study, the observation vector $\mathbf{d}_{obs}$ includes the subsurface temperature records located at different depth below the riverbed. The model parameter vector $\mathbf{m}$ is chosen to include the intrinsic permeability and thermal conductivity of saturated sediment in the riverbed because these two parameters are important to impact to the fluid and heat flow. Note that porosity is considered to be a known value in this study. If the thermal conductivity is known but porosity is uncertain, one can replace the thermal

conductivity in $\mathbf{m}$ with porosity. Estimating porosity and thermal conductivity are not suggested because they have similar impact to the heat transport and thus unidentifiable in assimilation.

The forward model used to generate the predicted data during data assimilation is a one-dimensional (1-D) hydro-thermal model that mimics the vertical flow and heat transport along the thermistor (Figure 3.2). The height of the 1-D model is 0.65 m with grid dimension 0.01 m. The observation depth for the 1-D numerical model is chosen to be -0.05 m and -0.25 m to accommodate the configuration of the thermistor. Note that the observation depth is increased by 0.01 m compared to the true sensor location to accommodate the three-dimensional(3-D) model built for validation(see next section). The computational cost for 3-D model with vertical grid dimension 0.01 m is unbearable. The temperatures and hydraulic head at the location of the deepest sensor are served as bottom boundary conditions, and the temperature and hydraulic head at the river side or the location of the shallowest sensor are served as the top boundary conditions to drive the 1-D hydro-thermal model. HEF is approximated as the average-in-depth vertical Darcy's flux calculated by the 1-D model. Estimation of HEF can be divided into two categories based on the availability of field measurement of hydraulic head. If hydraulic head and temperature are recorded simultaneously along the thermistor at different depths, permeability is chosen to be estimated. The recorded temperature and hydraulic heads at two different depths are used as boundary conditions to drive the 1-D hydro-thermal model to generate predicted temperatures at the observation point. The permeability in addition with thermal conductivity and/or

porosity thus can be estimated with the analysis equation (5). Once the permeability is estimated, HEF can be calculated with the estimated permeability and measured hydraulic gradient based on Darcy's law. Note that the water viscosity is dynamic over time and needs to be correlated with temperature using equation (4). If the hydraulic head are not recorded in the field, Darcy flux is estimated directly. Note that average-in-depth Darcy flux cannot be assigned in the simulator PFLOTRAN directly. To accommodate the simulator, the actual parameter that is estimated is the hydraulic head at the top of the 1-D model with the fixed hydraulic head at the bottom. An empirical permeability value needs to be provided to drive the 1-D hydro-thermal model. The accuracy of the prior permeability does not affect the estimated flux as higher or lower prior permeability than the true value will lead to lower and higher estimation of hydraulic head at the top and what we care is the product of permeability and hydraulic gradient. Note that the Darcy flux is dynamic over time, so using ES-MDA to estimate Darcy flux needs to be conducted sequentially by setting the posterior of the previous time window as the prior of the current time window.

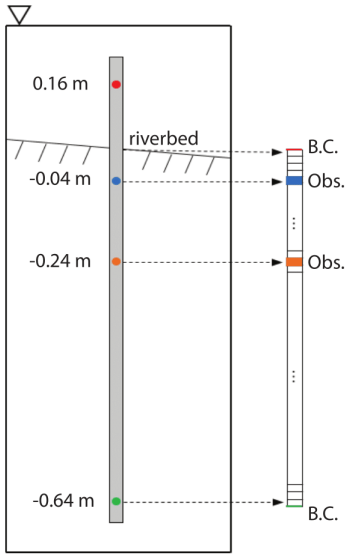

Figure 3.2 Thermistor configuration and the associated 1-D hydro-thermal model. Schematic diagram of the thermistor and the 1-D hydro-thermal model that simulate the fluid and heat flow along the thermistor. Temperatures recorded by middle sensors at depths -0.04 m and -0.24 m are considered to be observations, and the hydraulic heads and temperatures at the river and bottom side are used as boundary conditions to drive the 1-D numerical model. The grid dimension of the 1-D numerical model is 0.01 m.

3.2.4 Scheme of validation

To validate the proposed method, a two-step validation process is designed. The first step is using 1-D hydro-thermal model to validate the method under ideal flow condition. The configuration of the 1-D hydro-thermal model is the same as the forward model used in data assimilation, and the top and bottom boundary conditions are extracted from the 3-D model at river side and the depth of -0.65 m, respectively. The simulated temperatures by the 1-D model at different depths are used as synthetic observations to estimate HEF. The second step is using 3-D model to test the performance of the proposed method under the multi-flow condition. Two 3-D models are built with homogeneous and heterogeneous property for the alluvium layer,

respectively. The reason for designing the second step is the 1-D forward model used in data assimilation simplifies the real flow field, and we are interested in the impact of the structural error of forward model to the estimation of HEF. The 3-D model has the dimension of 400 m×400 m×20 m covering the area where the thermistor and piezometers are installed (Figure 3.3). The model uses the long-term monitored river stage and river temperature as the boundary condition at the river side. For the inland side, the flow condition is assumed to be no flux and the temperature is assumed to be constant. The model domain is divided into three zones based on the geological setting. A highly permeable unconfined aquifer, Hanford formation, is connected to the Columbia river with saturated thickness fluctuating between ~5 m and ~8 (Chen et al., 2012). The Hanford formation is underlain by a less permeable formation, named Ringold, and overlain by an alluvium layer with thickness between ~1 m and ~2 m for the part connected with river. Since no enough data is available to characterize the hydraulic and thermal properties, two models, one homogeneous model and one heterogeneous model with permeability distributed lognormaly in the alluvium layer, are built to investigate the influence of multi-dimensional flow and heterogeneity, respectively. These two 3-D model can approximate the flow and heat transport conditions at the field condition.

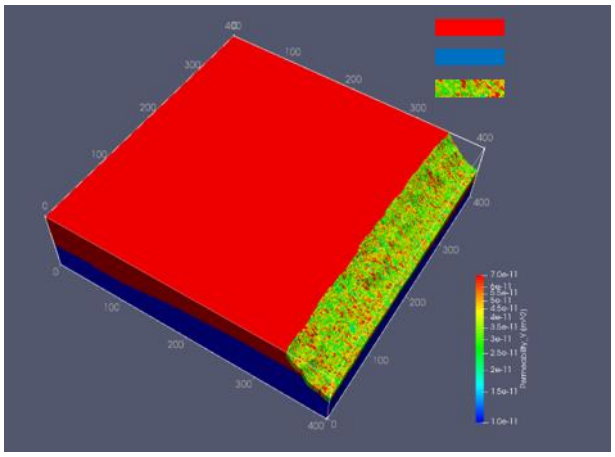

Figure 3.3 3-D hydro-thermal model of the study site. Permeability field of the 3-D numerical model with the dimension 400 m×400 m×20 m built for the study site. Black spot is the location where the thermistor is installed.

3.3 Results and discussion

3.3.1 Validation using 1-D hydro-thermal model

3.3.1.1 with hydraulic head information

Hydraulic head measurements provide us accurate information of hydraulic gradient below the riverbed, so the performance of the method is subject to the accuracy of estimated permeability. The parameters used in the 1-D model to generate the synthetic observations, including permeability, thermal conductivity and porosity, are considered to be the true values and the estimated parameters are compared with the true values to verify the accuracy of this method. Parameters used in data assimilation are listed in Table 3.2. The prior logarithmic permeability, thermal conductivity and porosity are all assumed to satisfy normal distribution. Note that the observation error ratio is defined as the ratio between the observation error to the observation value. The observation error is

not only impacted by the resolution of thermistor, but also by the field environmental. One can use an absolute observation error if the prior information of observation error is accessible, otherwise relative observation error can be used to account for the noise from different sources. Figure 3.4 shows the posterior distribution of parameters after each iteration of ES-MDA by assimilating different number of data points with observation error ratio 0.01. The estimated parameters show different sensitivity to the number of observation points. Permeability is most sensitive to the temperature observation and requires the least number of observation points to converge to the true value. 1000-minutes continuous temperature observation (200 points at the interval of 5 minutes) are found to be enough for accurate estimation of permeability with the observation error ratio 0.01. Thermal conductivity is less sensitive to the temperature observation and requires longer observation time to converge to the true value. Porosity is found to be not sensitive to the temperature observation, thus it is recommended to get the prior information of porosity by field measurement. Figure 3.5 shows the percent error between the estimated value and true value with different observation error ratios.

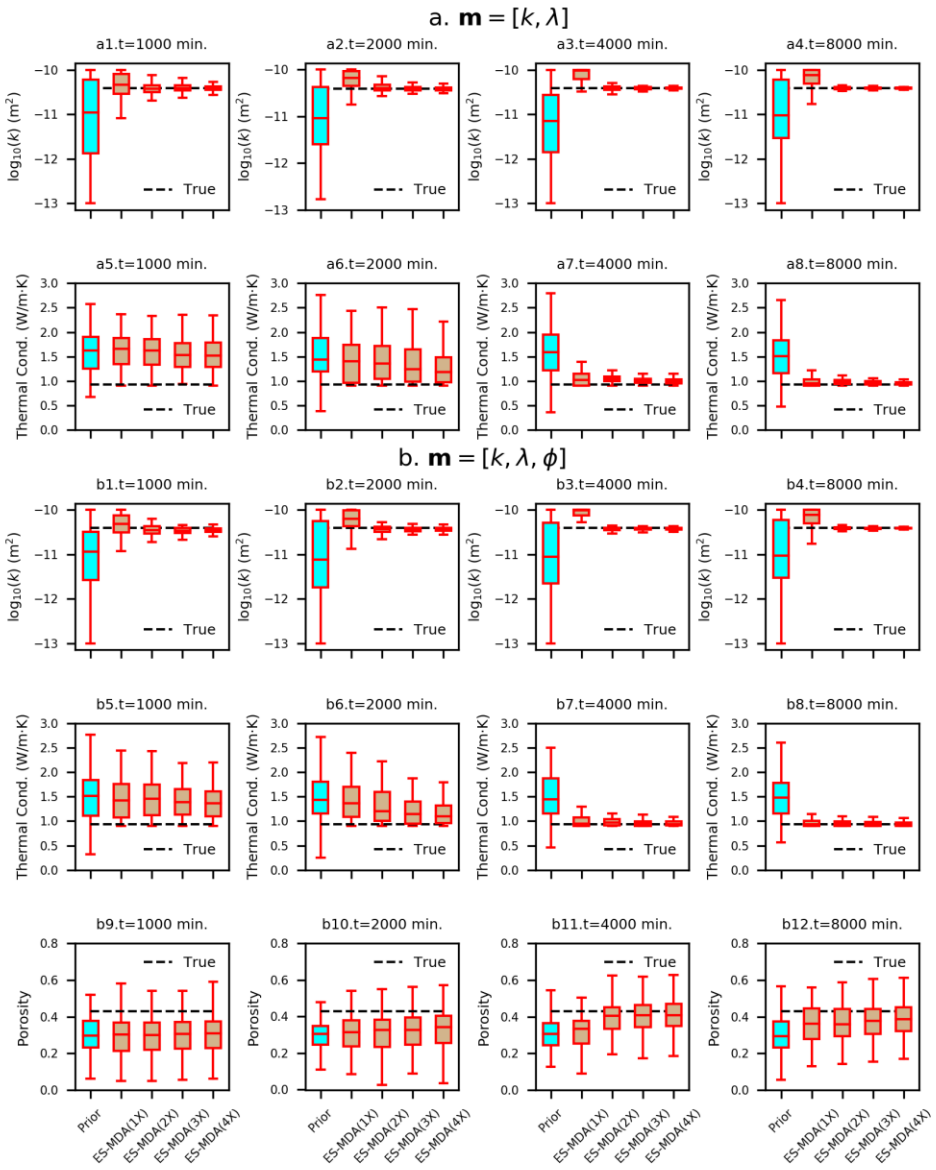

Figure 3.4 Estimation of permeability, thermal conductivity and porosity of 1-D hydro-thermal model using ES-MDA by considering two parameter set(a) and three parameter set(b). a1-a4 and a5-a8 show the evolution of permeability(k) and thermal conductivity(λ), respectively, with the assimilation time windows t=1000,2000,4000 and 8000 minutes. b1-b4, b5-b8 and b9-b12 show the evolution of permeability, thermal conductivity and porosity(φ), respectively, with the number of data points t=200,400,800 and 1600.

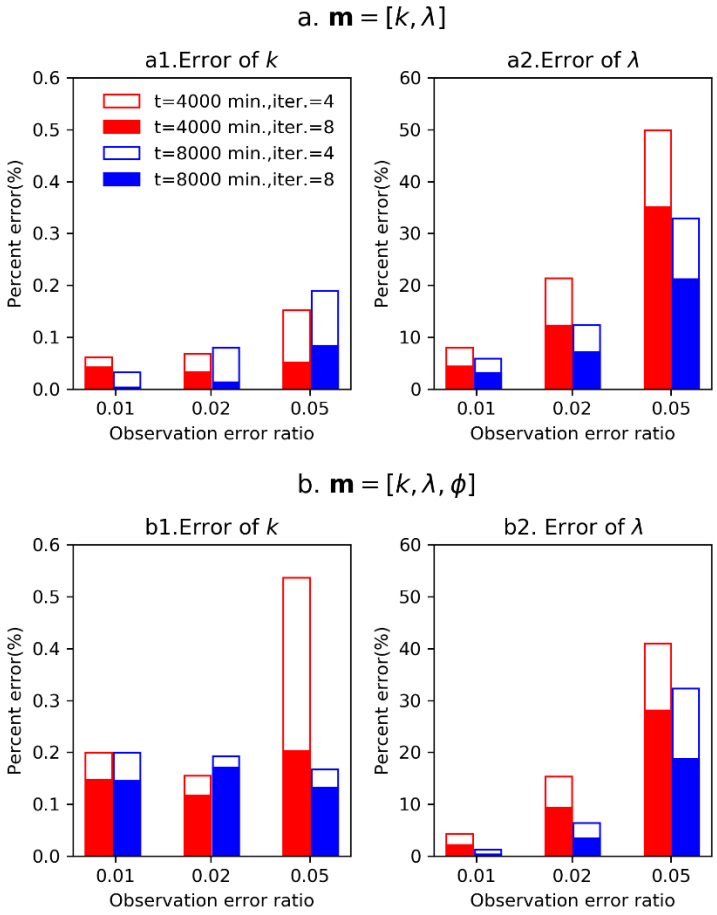

Figure 3.5 Error of estimated k and λ with different observation error ratio. a. k and λ are estimated, b. k, λ and φ are estimated.

Table 3.2 Model parameter and data assimilation setting

Parameter	Value
True $\log_{10}(k)$	-10.41 $\log_{10}(m^2)$
True λ	0.93 W/(m·K)
True φ	0.43
Mean of $\log_{10}(k)$	-11 $\log_{10}(m^2)$
s.d. of $\log_{10}(k)$	1 $\log_{10}(m^2)$
Upper limit of	-10 $\log_{10}(m^2)$
Lower limit of	-13 $\log_{10}(m^2)$
Mean of λ	1.5 W/(m·K)
s.d. of λ	0.5 W/(m·K)
Upper limit of λ	2.5 W/(m·K)
Lower limit of λ	0.9 W/(m·K)
Mean of φ	0.3
s.d. of φ	0.1
Upper limit of φ	0.7
Lower limit of φ	0.01
Number of	100
Number of	4/8
Observation error	0.01/0.02/0.05

Greater observation error does not have obvious impact on the estimation of permeability. However, the accuracy of thermal conductivity decreases a lot, and longer observation time and more iterations are needed to reduce the error of estimated thermal conductivity. As HEF is the focus of this study and it is only determined by permeability under the condition that hydraulic gradient information is known, whether the estimated thermal conductivity and porosity are accurate enough or not do not affect the estimation of HEF.

Once the permeability is estimated, HEF can be calculated according to Darcy' law with the measured hydraulic gradient. Figure 3.6(a-d) displays the estimated temperature using prior ensemble of permeability and thermal conductivity. The mean temperature deviates from the true temperature significantly especially between the period of 4/17/2017 and 4/25/2017 when strong upwelling of cold groundwater occurs. EnKF and ES-MDA have similar performance in terms of parameter estimation. However, the computational cost of EnKF is much more expansive than the ES-MDA by assimilating the same amount of data due to the frequent restart of simulation (~2 hours v.s. 4 minutes by assimilating 800 data points). Figure 3.6(e) shows the annual variation of hydraulic conductivity considering the impact of temperature on water viscosity. The minimum and maximum hydraulic conductivity over the year 7/2016-7/2017 are ~21 m/d, and ~33 m/d, respectively, indicating that using a single point-of-time field measurement of hydraulic conductivity may cause an error up to 50\% while estimating HEF.. Note that upwelling of hot water observed in late Jan., 2017 and middle March, 2017 are accompanied with the rapid increase of hydraulic conductivity. Cold water upwelling is observed in the late April, 2017 and early May, 2017 along with the decrease of hydraulic conductivity. Figure 3.6(f-g) compares the HEF calculated by PFLOTRAN and Darcy's law with dynamic hydraulic conductivity in consideration. Downwelling dominates in terms of the flux magnitude and duration, especially between April and July when the river stage is high. The HEF calculated by two methods agreed well, indicating that the thermal-induced viscosity and hydraulic conductivity change is an important factor that needs to be considered while using Darcy's law to estimate the

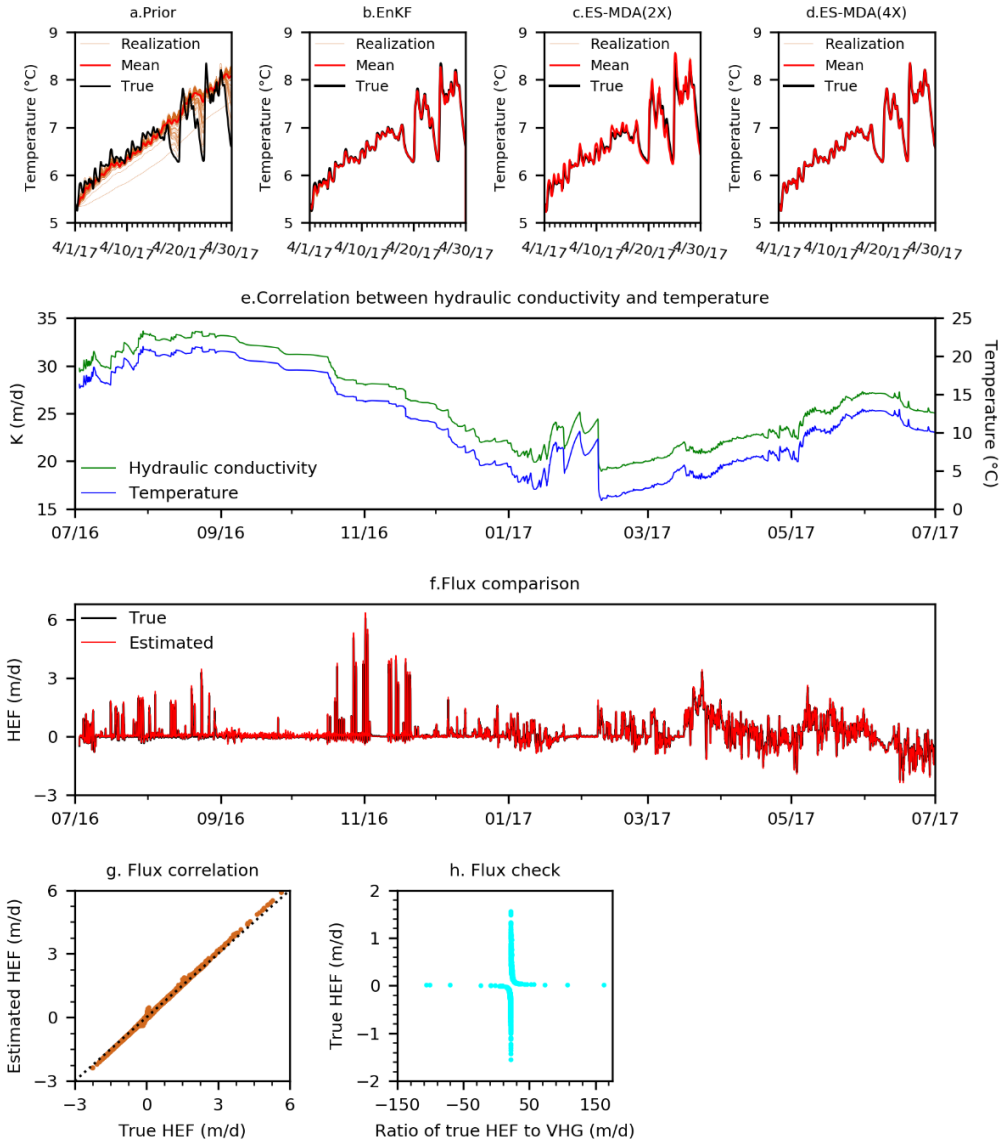

Figure 3.6 Performance of data assimilation methods and the accuracy of estimated HEF under synthetic 1-D flow condition. a. Estimated temperature at the depth of -0.25 m using prior ensemble of permeability and thermal conductivity. b. Posterior temperature at the depth of -0.25 m using EnKF method. c-d. Posterior temperature at the depth of -0.25 m using ES-MDA method after 2 and 4 iterations, respectively. e. Temperature at the depth -0.25 m and correlated hydraulic conductivity using equation 6 based on the estimated permeability. Note that a sharp increase of hydraulic conductivity is observed in Jan., 2017 due to the upwelling of hot groundwater. f. Comparison between the true HEF calculated by PFLOTRAN and the estimated HEF based on Darcy's law. g. Correlation between the true HEF and estimated HEF. h. Correlation between the true HEF and the ratio of the true HEF to hydraulic gradient.

HEF. In PFLOTRAN, the equation of state for water has considered the impact of temperature and pressure to the viscosity, thus it can gives correct estimation for flux. Also note that when the vertical flux is very small ($<10^{-3}$ m/d), the estimated hydraulic conductivity cannot be used to calculate the HEF by multiplying with hydraulic gradient. Figure 3.6(h) shows the correlation between the true HEF and the ratio of true HEF to the hydraulic gradient. As one can see, when HEF is large, the ratio is nearly constant indicating a constant hydraulic conductivity. However, when HEF is very small, the ratio increases to a large value that is beyond the reasonable range of hydraulic conductivity. A possible reason for this phenomenon is small values of both flux and hydraulic gradient will increase the impact of numerical issue and the ratio between them cannot be considered as the hydraulic conductivity at this situation.

3.3.1.2 Without hydraulic head information

When hydraulic head information is not accessible, the Darcy's flux q is considered as a variable and estimated directly by assimilating the recorded subsurface temperature. Previous analysis has demonstrated that fluid flow related parameter (e.g. k) is most sensitive to the temperature observation, and q, is expected to has similar performance compared with k in terms of parameter estimation through temperature observation. The most obvious difference between estimating k and q is q is dynamic in nature and thus it can only be approximated by a constant value in small time window. The small time window of data assimilation determines the resolution of estimated q.

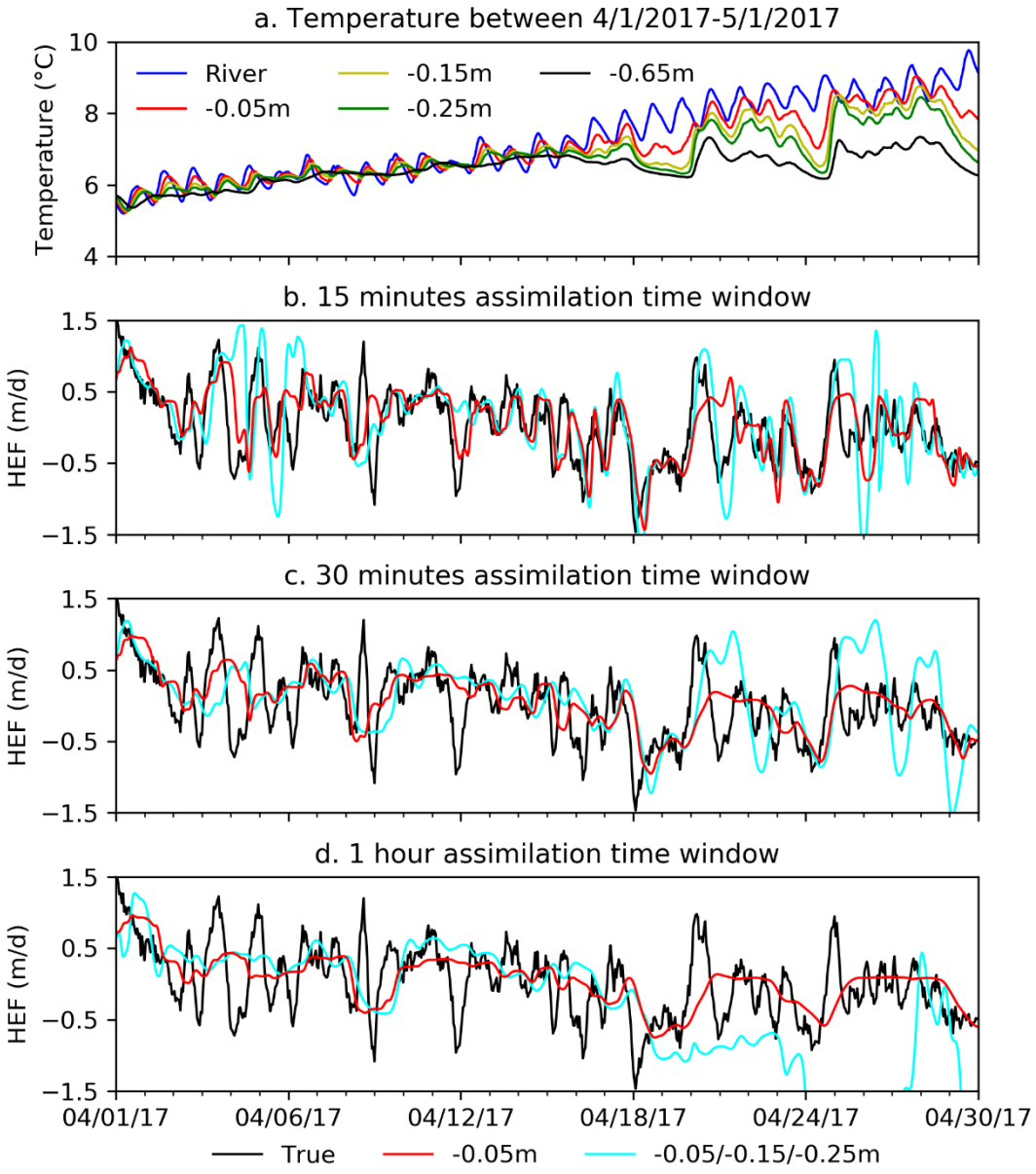

Figure 3.7 Estimation of HEF without hydraulic head information under synthetic 1-D flow condition. The observations are synthetic temperature time series collected at the frequency of 5 minutes from the depths of -0.05 m, -0.15 m and -0.25 m. Only flux qis estimated assuming φ and λare known. a. River temperature and simulated temperatures at different depths. b-d. Estimated HEFs by assimilating 1-point temperature data from depth -0.05 m and 3-points data from three observation depths using 15-minutes(b), 30-minutes(c) and 1-hour(d) assimilation time windows.

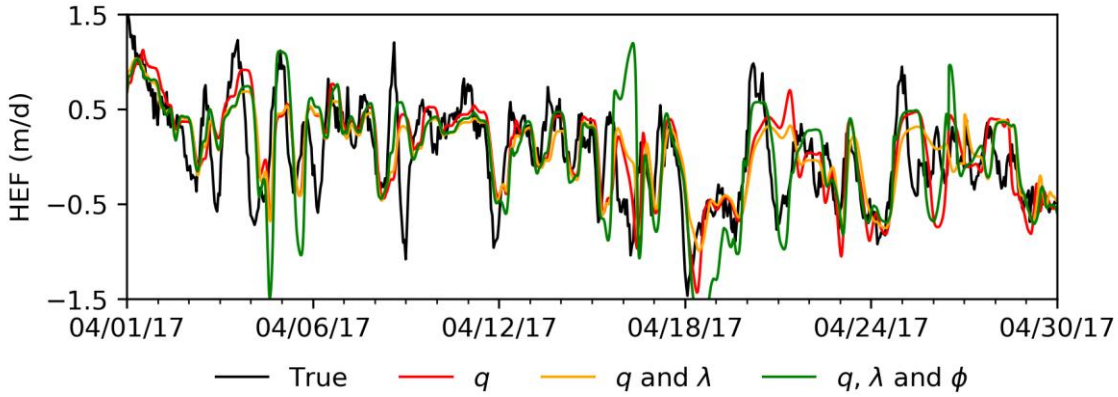

Figure 3.8 Sensitivity of HEF estimation without hydraulic head information to the number of estimated parameters. Three parameter sets are considered, including 1 parameter q, two parameters q and φand three parameters q,φ and λ. The temperature time series are extracted from the synthetic 1-D model at the depth -0.05 m and the assimilation time window is 15-minutes.

Figure 3.7 shows the estimated q with different assimilation time windows using single and multiple observations. As one can see, the scenario with 15-minutes assimilation time window can capture most sub-daily flux dynamics for both downwelling and upwelling periods, except for the situation that flux changes very rapidly. The performance of estimating q is sensitive to the observation depth. Using single observation from depth -0.15 m, -0.25 m or combination of observations from three different depths have worth performance compared with that using single observation at the depth -0.05 m. This is because when the assimilation time window is small, the heat signal can only transport a few centimeters with the average Darcy's velocity ~1-2 m/day and the temperature records at deeper depth actually reflects the q at earlier time instead of current time window. Figure 3.8 shows the performance of this method using different combination of assimilating parameters. The difference between

estimating q alone and multiple parameters are small, indicating that q is most sensitive to the temperature observation, similar to the role of k.

The very rapid sub-daily flux change is not captured by the scenario of 15-minutes assimilation time window and 5-minutes observation interval. Although it is expected that reducing the assimilation time window to a smaller value (e.g. 5 minutes) and increasing the observation frequency to 1 minute interval can further increases the resolution of estimated q, it comes with higher computation cost and shorter monitoring period considering the storage of the thermistor sensors. An interesting question is if we can still capture the flux peaks using 15-minutes assimilation time window but with extra information of flow direction. The intention of knowing flow direction is we can manually adjust the prior distribution of q for the time window when q is found to be revered to accelerate convergence to the true value. To verify the hypothesis, a new scheme, namely, "discontinuous scheme", is designed. In the discontinuous scheme, the prior distribution of q will be regenerated to satisfy the lognormal distribution with mean 0.4 and standard deviation 0.2 When flow is detected to change from upwelling to downwelling. When the flow direction is reversed from downwelling to upwelling, the mean and standard deviation of prior distribution of q is assumed to be -0.4 and 0.2, respectively. Figure 3.9 shows that this scheme has better performance compared with the continuous scheme by capturing more peaks. Note that the discontinuous scheme only needs the flow direction information which could be inferred from the hydraulic head measurements at different depth near the thermistor, which does not require the piezometer at the same depth with heat sensor.

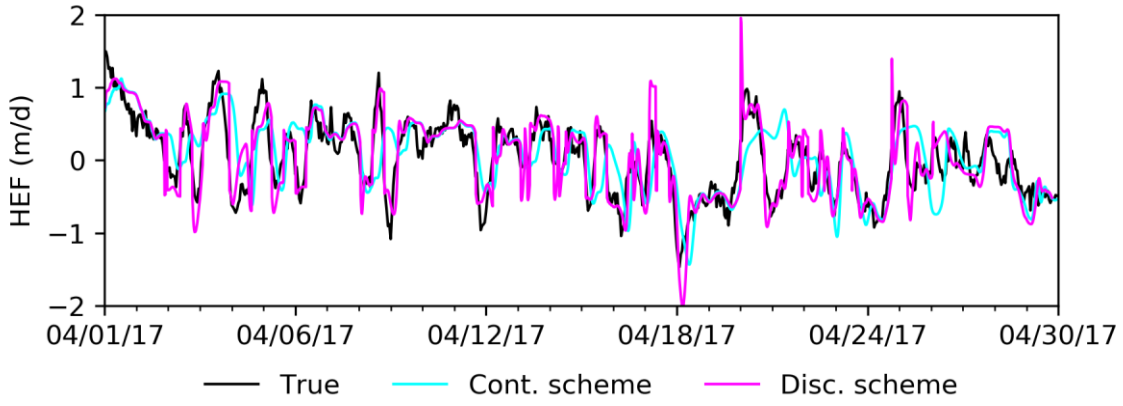

Figure 3.9 Estimation of HEF using continuous and discontinuous assimilation schemes. Continuous assimilation scheme means using the posterior parameters from previous assimilation time window as the prior of the current assimilation time window, and discontinuous assimilation scheme means regenerating prior parameters for current time window if the flow direction is found to be reversed. If the flow direction changes from downwelling to upwelling, the new prior of hydraulic gradient is generated with the mean and standard deviation set to be -0.4 and 0.2, respectively, and if the flow direction changes from upwelling to downwelling, the mean and standard deviation of the new prior of hydraulic gradient is set to be 0.4 and 0.2, respectively. Note that the discontinuous scheme requires the flow direction information known in advance, which could be inferred from the hydraulic head measurements. The temperature time series are extracted from the synthetic 1-D model at the depth -0.05 m and the assimilation time window is 15-minutes. Three parameters, including q,φ and λ, are estimated.

3.3.2 Test by 3-D homogeneous and heterogeneous models

3.3.2.1 With hydraulic head information

To investigate the influence of multi-dimensional flow and heterogeneity to the performance of data assimilation approach, simulated temperatures and hydraulic heads from 3-D homogeneous and heterogeneous models were used to estimate HEF. Figure 3.10 shows the comparison between the true HEF and the estimated HEF using different

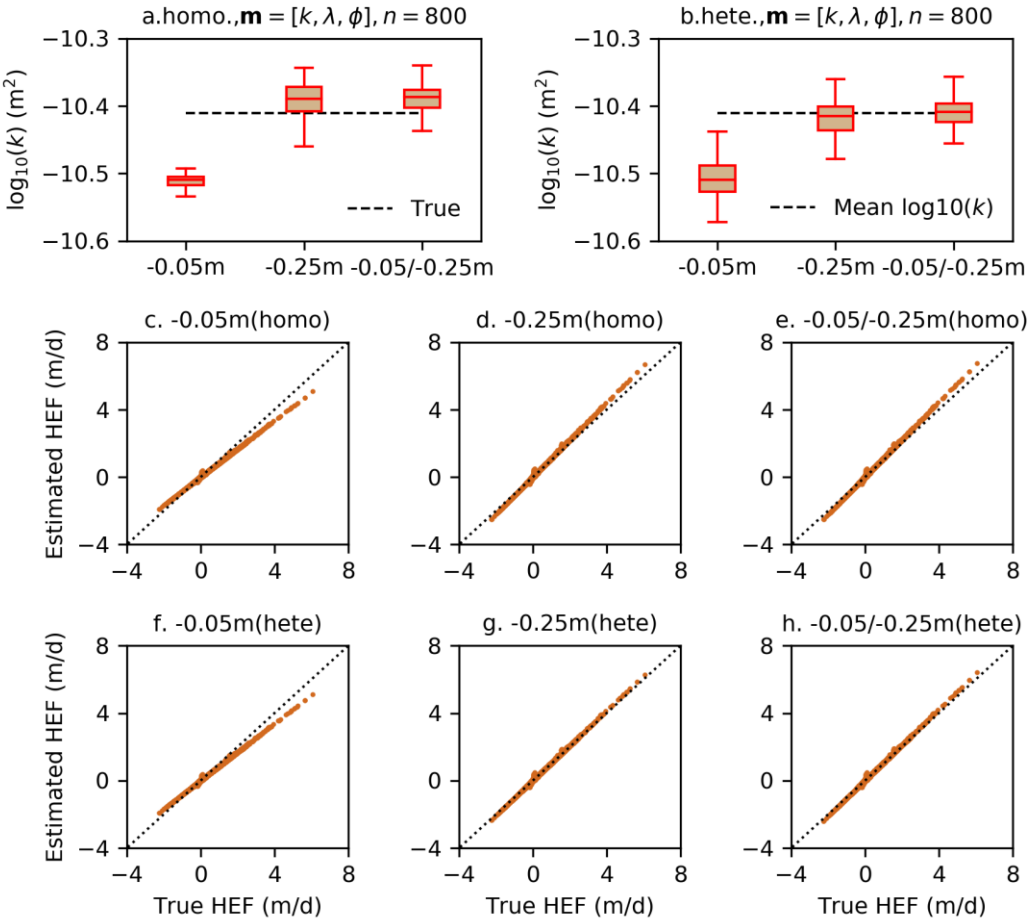

Figure 3.10 Estimation of HEF under 3-D homogeneous (a) and heterogeneous (b) flow conditions without hydraulic head information. Temperature observation is from the depth of -0.05 m and assimilation time window is 15 minutes. q,φand λare estimated together.

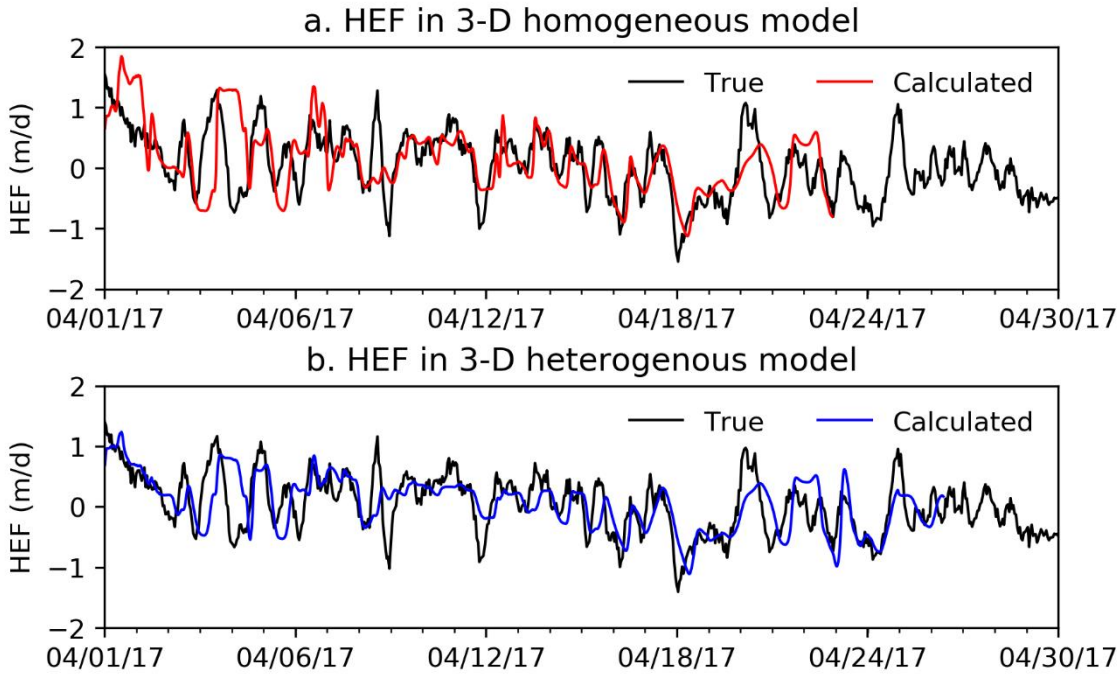

Figure 3.11 Estimation of HEF under 3-D homogeneous (a) and heterogeneous (b) flow conditions without hydraulic head information. Temperature observation is from the depth of -0.05 m and assimilation time window is 15 minutes. q, φ and λ are estimated together.

combinations of observation points by estimating permeability and thermal conductivity. The true permeability and thermal conductivity are the same with those listed in Table 3.2. It is found that multi-dimensional flow may introduce an error up to 20% and thermal conductivity cannot be estimated due to the structure error of using 1-D forward model to estimate the parameters of 3-D model. Lautz (2010) used a 2-D homogeneous model to test the impact of multi-dimensional flow to the performance of heat tracer method, and found that overestimation of flux cannot be avoided while using temperature as the indicator of flux magnitude because heat have multiple sources besides the top and bottom boundary.

3.3.2.2 Without hydraulic head information

Darcy' flux q was estimated by assimilating the synthetic temperatures from 3-D homogeneous and heterogeneous models, respectively. The assimilation time windows is chosen to be 15 minutes which has been demonstrated to be able to capture most flux dynamics. Figure 3.11 shows the estimated HEF for both homogeneous and heterogeneous models. The sub-daily flux variation and the reversing between downwelling and upwelling are captured. The performance of estimating on 3-D model is comparable to that on 1-D model and HEF with higher resolution is expected if smaller assimilation time window and observation interval are used.

3.4 Application and limitation

The proposed method was applied on the real temperature time series recorded by the thermistor to infer the HEF in the field condition. Although the numerical model can play the role of benchmark very well, the calculated HEF from the numerical model or the estimated HEF based on the synthetic temperatures cannot represent the actual HEF in the field condition as the numerical model is not calibrated.

Estimation of HEF requires the temperature records from three different depths. In addition, the distance between the observation sensor and boundary sensor is preferred to be small to accommodate the small assimilation time window. The temperature recorded at the depth -0.04 m and the river temperature are the best candidates for observation and boundary condition, respectively. However, these two temperature records are found to be nearly identical during downwelling and cannot be used together for assimilation. A possible reason is there is preferential path existed near the surface of the riverbed, so

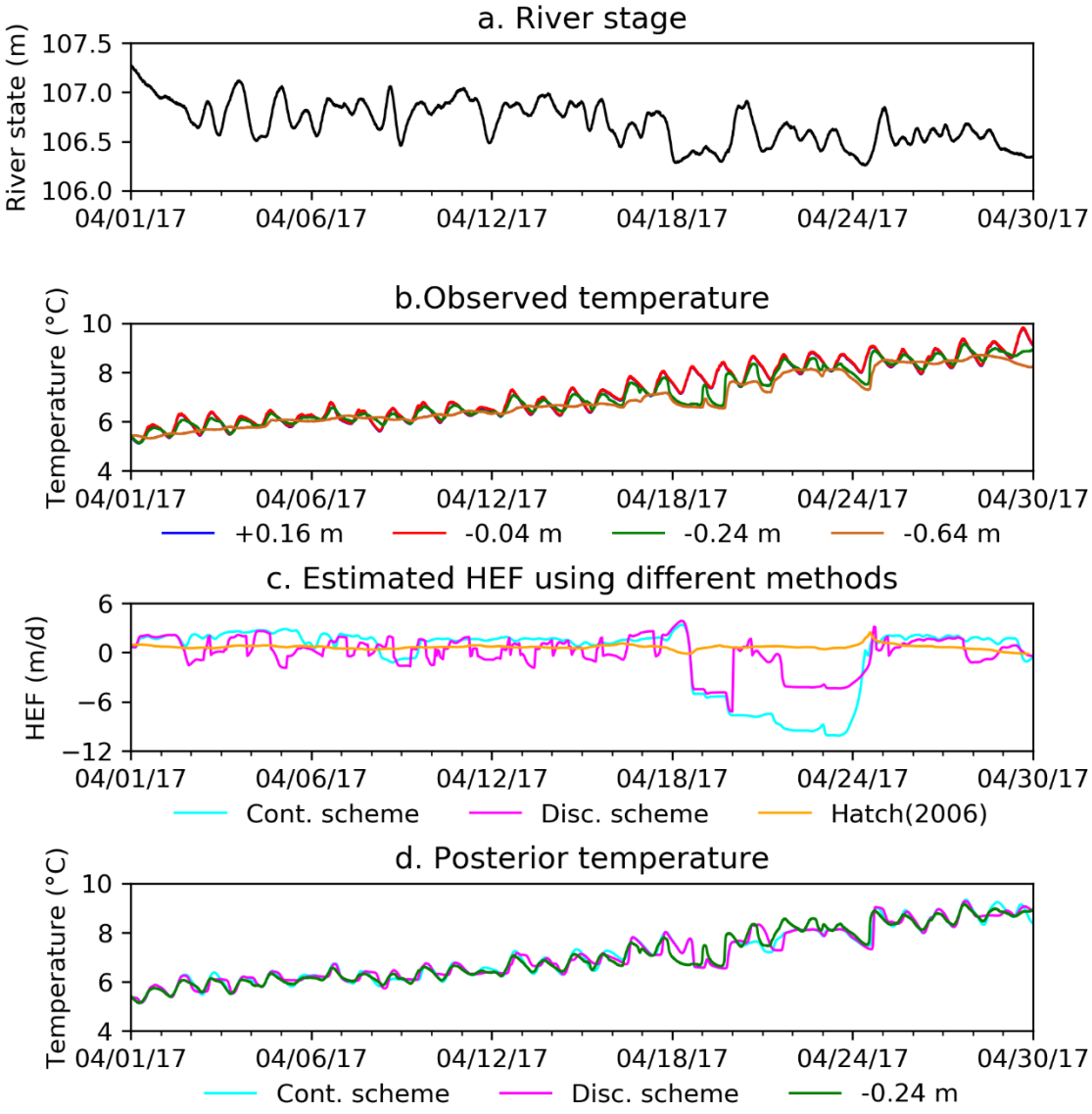

Figure 3.12 Estimated HEF between 7/2016 and 5/2018 using real temperature observations recorded at the Hanford site. Temperature is collected every 5 minutes. The temperature at the depth of -0.24 m is used as observation, and the temperature at the depth of -0.04 m and -0.64 m are used as boundary condition. Hydraulic heads are recorded at the depth of -0.55 m and -2.71 m near the thermistor. a. Observed river stage. b. Observed temperatures at different depths. c. Estimated HEF using continuous and discontinuous schemes. d. Posterior temperature by continuous and discontinuous schemes.

that river water is somehow connected to the sensor at the depth -0.04 m, especially during downwelling. Therefore, the temperature records at -0.04 m and -0.64 m are used as boundary conditions and the temperature at -0.24 m is considered to be observation. Figure 3.12(a) and (b) shows the river stage and recorded subsurface temperatures during April, 2017. Figure 3.12(c) displays the estimated HEFs in addition with the HEF calculated by Hatch et al.(2006) method. The HEF estimated by the assimilation approach is generally higher than that estimated by Hatch et al.(2006) method because the highly dynamic flux with large flux magnitude is captured by the assimilation approach. When upwelling of cold water occurs, the assimilation method fails to give reasonable estimation of HEF. Reducing the distance between the observation point and boundary could solve the issue.

The limitation of using assimilation approach to estimate HEF comes in two aspects. The first is high-frequency temperature observations are needed to make the parameter estimation converges after several iterations in small assimilation time window. The length of time window determines the resolution of HEF that can be detected by the method. High resolution of HEF requires small time window and more frequent observation. Time window of 20 minutes has been demonstrated to have good performance in reproducing the flow dynamics. A smaller time window such as 10 minutes or 5 minutes is expected to have a better performance but at the cost of computation time. The second is the distance between the observation point and boundary needs to be small, otherwise no useful temperature signals can be detected at the observation point in small assimilation time window.

3.5 Conclusion

An ensemble-based data assimilation method is proposed to estimate the HEF under highly dynamic flow condition using observed temperature time series with or without the hydraulic head information. If the hydraulic head information is known, one can estimate the permeability first and then calculate the HEF manually by considering the temperature-induced dynamic hydraulic conductivity. If the hydraulic head is not recorded, one can use high-frequency temperature time series to estimate sub-daily HEF as well. This is a promising method because the acquisition of temperature data is easy and it does not require the prior information of permeability, porosity and thermal conductivity.

References

Cardenas, M. B., and V. A. Zlotnik (2003), Three-dimensional model of modern channel bend deposits, Water Resour. Res., 39(6).

Cardenas, M. B., and J. L. Wilson (2007), Effects of current-bed form induced fluid flow on the thermal regime of sediments, Water Resour. Res., 43(8).

Cardenas, M. B., J. L. Wilson, and V. A. Zlotnik (2004), Impact of heterogeneity, bed forms, and stream curvature on subchannel hyporheic exchange, Water Resour. Res., 40(8).

Chen, Y., and D. X. Zhang (2006), Data assimilation for transient flow in geologic formations via ensemble Kalman filter, Adv. Water Resour., 29(8), 1107-1122.

Chen, X. Y., H. Murakami, M. S. Hahn, G. E. Hammond, M. L. Rockhold, J. M. Zachara, and Y. Rubin (2012), Three-dimensional Bayesian geostatistical aquifer characterization at the Hanford 300 Area using tracer test data, Water Resour. Res., 48.

Constantz, J. (1998), Interaction between stream temperature, streamflow, and groundwater exchanges in Alpine streams, Water Resour. Res., 34(7), 1609-1615.

Constantz, J., and F. Murphy (1991), The temperature-dependence of ponded infiltration under isothermal conditions, J. Hydrol., 122(1-4), 119-128.

Emerick, A. A., and A. C. Reynolds (2012), History matching time-lapse seismic data using the ensemble Kalman filter with multiple data assimilations, Computat. Geosci., 16(3), 639-659.

Emerick, A. A., and A. C. Reynolds (2013), Ensemble smoother with multiple data assimilation, Comput. Geosci. , 55, 3-15.

Evensen, G. (1994), Sequential data assimilation with a nonlinear quasi-geostrophic model using Monte-Carlo methods to forecast error statistics, J. Geophys. Res.-Oceans, 99(C5), 10143-10162.

Evensen, G. (2003), The Ensemble Kalman Filter: theoretical formulation and practical implementation, Ocean Dynam., 53(4), 343-367.

Evensen, G. (2009), Data Assimilation: The Ensemble Kalman Filter, Springer Berlin Heidelberg.

Gomez-Velez, J. D., J. Harvey, M. B. Cardenas, and B. Kiel (2015), Denitrification in the Mississippi River network controlled by flow through river bedforms, Nat. Geosci., 8(12), 941-U975.

Harvey, J., and M. Gooseff (2015), River corridor science: Hydrologic exchange and ecological consequences from bedforms to basins, Water Resour. Res., 51(9), 6893-6922.

Hatch, C. E., A. T. Fisher, J. S. Revenaugh, J. Constantz, and C. Ruehl (2006), Quantifying surface water-groundwater interactions using time series analysis of streambed thermal records: Method development, Water Resour. Res., 42(10).

Huang, X., C. B. Andrews, J. Liu, Y. Y. Yao, C. K. Liu, S. W. Tyler, J. S. Selker, and C. M. Zheng (2016), Assimilation of temperature and hydraulic gradients for quantifying the spatial variability of streambed hydraulics, Water Resour. Res., 52(8), 6419-6439.

Irvine, D. J., L. K. Lautz, M. A. Briggs, R. P. Gordon, and J. M. McKenzie (2015), Experimental evaluation of the applicability of phase, amplitude, and combined methods to determine water flux and thermal diffusivity from temperature time series using VFLUX 2, J. Hydrol., 531, 728-737.

Ju, L., J. J. Zhang, C. Chen, L. S. Wu, and L. Z. Zeng (2018), Water flux characterization through hydraulic head and temperature data assimilation: Numerical modeling and sandbox experiments, J. Hydrol., 558, 104-114.

Kalbus, E., F. Reinstorf, and M. Schirmer (2006), Measuring methods for groundwater - surface water interactions: a review, Hydrol. Earth Syst. Sc., 10(6), 873-887.

Kaufman, M. H., M. B. Cardenas, J. Buttles, A. J. Kessler, and P. L. M. Cook (2017), Hyporheic hot moments: Dissolved oxygen dynamics in the hyporheic zone in response to surface flow perturbations, Water Resour. Res., 53(8), 6642-6662.

Keery, J., A. Binley, N. Crook, and J. W. N. Smith (2007), Temporal and spatial variability of groundwater-surface water fluxes: Development and application of an analytical method using temperature time series, J. Hydrol., 336(1-2), 1-16.

Kiel, B. A., and M. B. Cardenas (2014), Lateral hyporheic exchange throughout the Mississippi River network, Nat. Geosci., 7(6), 413-417.

Kurtz, W., H. J. Hendricks Franssen, H. P. Kaiser, and H. Vereecken (2014), Joint assimilation of piezometric heads and groundwater temperatures for improved modeling of river-aquifer interactions, Water Resour. Res., 50(2), 1665-1688.

Lautz, L. K. (2010), Impacts of nonideal field conditions on vertical water velocity estimates from streambed temperature time series, Water Resour. Res., 46.

Lautz, L. K. (2012), Observing temporal patterns of vertical flux through streambed sediments using time-series analysis of temperature records, J. Hydrol., 464, 199-215.

Lautz, L. K., and D. I. Siegel (2006), Modeling surface and ground water mixing in the hyporheic zone using MODFLOW and MT3D, Adv. Water Resour., 29(11), 1618-1633.

Lautz, L. K., and R. E. Ribaudo (2012), Scaling up point-in-space heat tracing of seepage flux using bed temperatures as a quantitative proxy, Hydrogeol. J., 20(7), 1223-1238.

Luce, C. H., D. Tonina, F. Gariglio, and R. Applebee (2013), Solutions for the diurnally forced advection-diffusion equation to estimate bulk fluid velocity and diffusivity in streambeds from temperature time series, Water Resour. Res., 49(1), 488-506.

McCallum, A. M., M. S. Andersen, G. C. Rau, and R. I. Acworth (2012), A 1-D analytical method for estimating surface water-groundwater interactions and effective thermal diffusivity using temperature time series, Water Resour. Res., 48.

Oliver, D. S., and Y. Chen (2011), Recent progress on reservoir history matching: a review, Computat. Geosci, 15(1), 185-221.

Paulsen, R. J., C. F. Smith, D. O'Rourke, and T. F. Wong (2001), Development and evaluation of an ultrasonic ground water seepage meter, Ground Water, 39(6), 904-911.

Pebesma E., G., B. (2018), Spatial and Spatio-Temporal Geostatistical Modelling, Prediction and Simulation.

Rau, G. C., M. S. Andersen, A. M. McCallum, and R. I. Acworth (2010), Analytical methods that use natural heat as a tracer to quantify surface water-groundwater exchange, evaluated using field temperature records, Hydrogeol. J., 18(5), 1093-1110.

Rau, G. C., M. O. Cuthbert, A. M. McCallum, L. J. S. Halloran, and M. S. Andersen (2015), Assessing the accuracy of 1-D analytical heat tracing for estimating near-surface sediment thermal diffusivity and water flux under transient conditions, J. Geophys. Res.-Earth, 120(8), 1551-1573.

Rosenberry, D. O. (2008), A seepage meter designed for use in flowing water, J. Hydrol., 359(1-2), 118-130.

Rosenberry, D. O., and R. H. Morin (2004), Use of an electromagnetic seepage meter to investigate temporal variability in lake seepage, Ground Water, 42(1), 68-77.

vanLeeuwen, P. J., and G. Evensen (1996), Data assimilation and inverse methods in terms of a probabilistic formulation, Mon. Weather Rev., 124(12), 2898-2913.

Zhou, T., et al. (2017), A New Approach to Quantify Shallow Water Hydrologic Exchanges in a Large Regulated River Reach, Water, 9(9).

CHAPTER IV

FRACTIONAL MODELS SIMULATING NON-FICKIAN BEHAVIOR IN FOUR-STAGE SINGLE-WELL PUSH-PULL TESTS

4.1. Introduction

The single-well push-pull (SWPP) test is a classical tracer experiment that could be used to estimate solute transport properties near wellbores (Gelhar and Collins, 1971; Pickens and Grisak, 1981; Haggerty et al., 2001). "Push" and "Pull' refer to injection and pumping stages of the test, respectively. A typical SWPP test includes three stages, namely, tracer injection, resting, and pumping. Sometimes an additional chasing stage is added after tracer injection to push solute further away from the injection well. A primary advantage of SWPP tests compared with multi-well tracer tests is that the reversal of injection greatly increases the mass recovery (Nordqvist and Gustafsson, 2002). Another advantage is that the influence of preferential flow pathways to solute transport, especially in highly heterogeneous aquifers, is neutralized by allowing injection fluid and pumping fluid to move along the same pathway (Le Borgne and Gouze, 2008). In recent years, SWPP tests have been widely used as an efficient technology for evaluating geological reservoirs for subsurface CO_2 injection and storage (Yang et al., 2014; Rillard et al., 2014). In addition to studying subsurface geochemical reaction, SWPP tests have been used to study subsurface microbial activity and

*Reprinted with permission from "Fractional models simulating non-fickian behavior in four-stage single-well push-pull tests" by Chen, K., H. Zhan and Y. Qiang (2017), *Water Resour. Res.*, *53*, 9528-9545, Copyright [2017] by Wiley.

population dynamics for applications in contaminant remediation and bioaugmentation (Schroth et al., 2001; Istok et al., 2002; O'Mullan et al., 2015). In the energy sector, hydraulic fracturing and geothermal production have also applied SWPP tests with altered fracture networks or hydraulic conductivities to enhance natural gas or geothermal production (Cho et al., 2013; Ghergut et al., 2016).

A SWPP test is usually conducted at the meter scale, which means that the injected tracer only interacts with a small portion of the entire aquifer. Therefore, the properties estimated from SWPP tests such as dispersivity and porosity are localized and centered around the well. Despite the limited scale of this type of tests, local aquifers can exhibit anomalous transport behavior due to strong formation heterogeneity (Dentz et al., 2004). Early models developed to interpret SWPP test data usually assumed that solute transport obeyed Fick's law and only a mobile domain existed in aquifers (Gelhar and Collins, 1971; Güven et al., 1985). Gelhar and Collins (1971) gave a closed-form approximate analytical solution for SWPP tests in a single layer aquifer with the assumption that the aquifer was homogeneous and flow was steady. Falta (1984) proposed a closed-form solution for SWPP tests in a stratified aquifer on the basis of Gelhar and Collins's (1971) work. To our knowledge, no further closed-form analytical solution has been proposed to deal with dual-domain aquifer or fracture-induced anomalous transport. This is probably due to the fact that multiple fluid flow stages in a SWPP test greatly complicate any analytical treatment.

Many numerical simulations have been conducted to investigate SWPP tests. Güven et al. (1985) modeled the SWPP test data in a stratified aquifer using a Lagrangian-

Eulerian method and found that the use of scale-dependent dispersivity can be relaxed if the flow field was known in detail. Tsang (1995) used a stochastic approach to model a double-porosity aquifer with high fracture density and stated that the SWPP test was a good diagnostic tool for determining matrix diffusion. Nordqvist and Gustafsson (2002) used SUTRA (Voss, 1984) to do scoping calculation for SWPP tests and investigated the identifiability of transport parameters such as dispersivity and retardation factor. For a multi-stage SWPP test, one alternative to numerical simulations is to propose an analytical solution for each stage and use the result of a previous stage as the initial condition for the next stage. The advantage of such an approach is that the complex four-stage problem is decomposed into four relatively simple problems and each problem can be solved analytically. Haggerty et al. (2001) adapted this approach and combined it with a multi-rate mass transfer model to investigate non-Fickian transport behavior observed in SWPP tests in a fractured aquifer.

Over the past decade, most SWPP tests have been conducted in fractured aquifers in which strong heterogeneity and anomalous transport were observed. Those tests were specially designed to verify different non-Fickian transport models and help estimate aquifer properties. There are three kinds of models that were commonly used to interpret anomalous transport behavior, including multi-rate mass transfer, continuous time random walk (CTRW), and fractional advection-dispersion equation (fADE) models. The multi-rate mass transfer model assumes that the mass transfer rate between mobile and immobile domains satisfies a certain distribution, such as lognormal or gamma distribution (Haggerty and Gorelick, 1995; Haggerty et al., 2000). The multi-rate model

works well in predicting long-tail breakthrough curves (BTCs) in fractured aquifers and has already been used to interpret SWPP test data (Haggerty et al., 2001). The CTRW model is a probability model borrowed from the physics community that is useful in describing solute transport in porous media. Several studies have demonstrated that CTRW is a general model for describing solute transport and that the multi-rate mass transfer model is a special case of CTRW (Berkowitz and Scher, 1998; Dentz and Berkowitz, 2003; Berkowitz et al., 2006). Le Borgne and Gouze (2008) developed a CTRW model with a dual-slope power-law transition time distribution to interpret a SWPP test exhibiting heavy tailing. The fractional model is an alternative to interpret the anomalous transport. The equivalence of the fractional model with the multi-rate model has been demonstrated (Benson et al., 2000; Schumer et al., 2003). To our knowledge, no fractional models have been developed yet to interpret SWPP tests. Benson et al. (2004) developed a fractional model to simulate a single-well pumping scenario, which would be equivalent to the last stage in a SWPP test. However, the temporal subordination method that was used to calculate the fractional-in-time derivative by Benson et al. (2004) cannot be extended to the multi-stage SWPP test because the advection-dispersion operator depends on time.

The objective of this study is to develop a new fractional model to interpret four-stage SWPP test data with long-tail BTCs obtained from a fractured aquifer. A general implicit Euler method is proposed to solve the coupled fractional-in-time-and-space model (FTS) and to match the four-stage SWPP test data with arbitrary boundary conditions in a radial coordinate system. Our newly developed fractional model can be

used to predict solute distribution in mobile and immobile zones at different stages. In addition, a new semi-analytical solution to the mobile-immobile model with a first-order mass transfer rate for the four-stage SWPP test is developed to investigate the difference of local and non-local transport BTCs in SWPP tests. A minor point to note is that the fractional model developed here is established on the basis of the mobile and immobile approach, and it is similar to that used in Schumer et al. (2003), but different from the fractional models of Benson et al. (2000, 2004).

4.2. Methodology

Since a SWPP test involves single-well injection and pumping, a radial coordinate system is the best framework to investigate the problem. Model specifics are discussed in the following section. The assumptions made in our approach are as follows: 1) the well is fully penetrating and the injection rate and pumping rate are both constant, but not necessarily the same; 2) the aquifer is horizontally isotropic with a uniform thickness, and extends sufficiently far from the well so the outer boundary is not a model constraint; 3) the upper and lower boundaries of the aquifer are impermeable to flow and transport; 4) the regional flow is neglected and flow is only driven by injecting (or pumping) during the experimental period; 5) transverse dispersion is ignored and only radial dispersion is considered; 6) flow is steady-state during injection, chasing, and pumping stages.

The influence of transient flow on the BTCs in SWPP tests is omitted in many previous studies of SWPP tests (Haggerty et al., 2001; Becker and Shapiro, 2003; Le Borgne and Gouze, 2008). The flow transience is caused by a number of factors

including a finite hydraulic diffusivity (which is the ratio of radial hydraulic conductivity over the specific storage) and the wellbore storage. In general, a smaller hydraulic diffusivity will require a longer time to reach steady state, and/or a larger wellbore radius will result in a greater wellbore storage effect, which will disturb the early flow field over a longer period of time. Considering that the difference between the solution under transient flow and the solution under steady flow is concentrated near the peak of the BTC and such a difference is negligible at late time, the flow field is assumed to reach steady state instantaneously during stage change for simplification (Nordqvist and Gustafsson, 2002; Wang et al., 2017). Nevertheless, a precise understanding of the influence of flow transience on the SWPP test deserves an independent investigation in the future and will not be reported in this study.

4.2.1. The Fractional model for SWPP tests

The mass balance equation of mobile zone transport in a radial flow system without a source and sink term is

$$\frac{\partial c_m}{\partial t} + \beta \frac{\partial c_{im}}{\partial t} = -\frac{1}{r}\frac{\partial}{\partial r}\left[rq(r,t)\right] \quad (1)$$

where c_m and c_{im} are the solute concentrations in the mobile and immobile zones, respectively [M/L^3]; t is the transport time [T]; r is the radial distance to the center of an injection or pumping well [L]; $\beta = \theta_{im}/\theta_m$ is the capacity ratio (or immobile-mobile ratio); θ_{im} and θ_m are the porosities in the immobile and mobile zones, respectively; $q(r,t)$ is the mass flux term. The mass flux term of Fickian transport can be represented as the sum of advective flux and dispersive flux

$$q(r,t) = v(r)c_m - D(r)\frac{\partial c_m}{\partial r} \tag{2}$$

where $v(r)$ is the advective velocity [L/T] and $D(r)$ is the dispersion coefficient [L/T^2]. $v(r)$ and $D(r)$ are both distance-dependent and given by $v(r) = Q/(2\pi b\theta_m r)$ and $D(r) = aQ/(2\pi b\theta_m r)$, respectively, where Q is the injection or pumping rate [L^3/T], b is the aquifer thickness [L] and a is the radial dispersivity [L]. Note that the fluid flow field is assumed to be in steady state. For simplification, the set of parameters $Q/(2\pi b\theta_m)$ is replaced by κ_v hereinafter.

The SWPP test usually includes four sequential stages, namely, tracer injection, water chasing, resting and pumping. The governing equation describing a SWPP test with a first-order rate-limited mobile-immobile mass transfer is thus obtained by substituting equation (2) into (1)

$$\frac{\partial c_m}{\partial t} + \beta\frac{\partial c_{im}}{\partial t} = L(t)c_m \tag{3}$$

$$\theta_{im}\frac{\partial c_{im}}{\partial t} = \omega(c_m - c_{im}) \tag{4}$$

where

$$L(t) = \begin{cases} -\dfrac{\kappa_v}{r}\dfrac{\partial}{\partial r} + \dfrac{a\kappa_v}{r}\dfrac{\partial^2}{\partial r^2} & 0 \le t < t_{inj} \\ -\dfrac{\kappa_v}{r}\dfrac{\partial}{\partial r} + \dfrac{a\kappa_v}{r}\dfrac{\partial^2}{\partial r^2} & t_{inj} \le t < t_{cha} \\ 0 & t_{cha} \le t < t_{rest} \\ \dfrac{\kappa_v}{r}\dfrac{\partial}{\partial r} + \dfrac{a\kappa_v}{r}\dfrac{\partial^2}{\partial r^2} & t_{rest} \le t < t_{pump} \end{cases} \tag{5}$$

(Haggerty et al., 2001). Here $L(t)$ is a temporally dependent spatial operator; t_{inj}, t_{cha}, t_{rest}, and t_{pump} are the ending times of injection, chasing, resting, and pumping stages, respectively, for a complete SWPP test. Note that the advection-dispersion equation (ADE) for injection and chasing stages are the same if one assumes that the injection rates of these two stages remain

identical. This assumption is valid and it is actually a normal setting in SWPP tests (Gouze et at., 2008). The difference between these two stages is reflected at the boundary conditions at wellbore, which will be discussed later. Actually, water chasing does not add new solutes into the aquifer and the objective of injecting chasing fluid is to push tracer farther from the injection well to obtain more information on subsurface properties while pumping back. If the chasing stage is not included in the field experiments, the part of $L(t)$ between t_{inj} and t_{cha} can be omitted.

For non-Fickian transport, more specifically, non-local transport in space, the mass flux term is given by

$$q(r,t) = v(r)c_m - D(r)\left[p\frac{\partial^{\alpha-1}c_m}{\partial r^{\alpha-1}} + (1-p)\frac{\partial^{\alpha-1}c_m}{\partial(-r)^{\alpha-1}} \right] \tag{6}$$

where $\partial^{\alpha-1}c_m/\partial r^{\alpha-1}$ and $\partial^{\alpha-1}c_m/\partial(-r)^{\alpha-1}$ are the Riemann-Liouville fractional derivatives; p is the skewness indicating the proportion of preferential path in the direction of flow, and p=1 and p=0 represent maximally positive skewness and maximally negative skewness respectively; α is the fractional order in space satisfying $1 < \alpha \leq 2$, which describes the degree of non-local transport in space; $D(r) = a_{FS}\kappa_v/r$ and a_{FS} is fractional dispersivity [$L^{\alpha-1}$] (Benson, 2004). Note that a_{FS} is not the same as the dispersivity in classical ADE because its unit is a fraction of unit length. Inserting equation (6) into (3), the fractional-in-space (FS) model describing SWPP tests is obtained as

$$\frac{\partial c_m}{\partial t} + \beta\frac{\partial c_{im}}{\partial t} = L_{FS}(t)c_m \tag{7}$$

where

$$L_{FS}(t)=\begin{cases}-\dfrac{\kappa_v}{r}\dfrac{\partial}{\partial r}+\dfrac{a_{FS}\kappa_v}{r}\dfrac{\partial^{\alpha}}{\partial r^{\alpha}} & 0\le t<t_{inj}\\ -\dfrac{\kappa_v}{r}\dfrac{\partial}{\partial r}+\dfrac{a_{FS}\kappa_v}{r}\dfrac{\partial^{\alpha}}{\partial r^{\alpha}} & t_{inj}\le t<t_{cha}\\ 0 & t_{cha}\le t<t_{rest}\\ \dfrac{\kappa_v}{r}\dfrac{\partial}{\partial r}+\dfrac{a_{FS}\kappa_v}{r}\dfrac{\partial^{\alpha}}{\partial(-r)^{\alpha}} & t_{rest}\le t<t_{pump}\end{cases} \quad (8)$$

Note that the skewness p is set to be 1 in the injection and chasing stages because the distribution of tracer concentration skews to the far side along the flow direction, and p is set to be 0 in the pumping stage as the flow is reversed and the distribution skews towards the wellbore. The temporal effect of non-Fickian transport is incorporated into the term $\beta\partial c_{im}/\partial t$. For first-order rate-limited mass transfer between the mobile and immobile zones, c_{im} and $\partial c_{im}/\partial t$ are given as (Schumer et al., 2003)

$$c_{im}=\omega e^{-\omega t}*c_m+c_{im}(r,0)e^{-\omega t} \quad (9)$$

$$\frac{\partial c_{im}}{\partial t}=\frac{\partial}{\partial t}\left[f(t)*c_m\right]+\frac{1}{\omega}\frac{\partial}{\partial t}\left[f(t)c_{im}(r,0)\right] \quad (10)$$

where $f(t)=\omega e^{-\omega t}$ is the memory function which is the probability density of solutes entering the immobile zone at t=0 and remaining there at time t (Carrera et al., 1997); "*" is the convolution sign; ω is the first-order mass transfer rate [1/T]; $c_m(r, 0)$ and $c_{im}(r, 0)$ are the initial concentrations in the mobile and immobile zones, respectively. For SWPP tests, $c_{im}(r, 0)$ is zero, so the relation between the mobile and immobile concentrations for SWPP tests can be simplified as

$$c_{im}=f(t)*c_m \quad (11)$$

$$\frac{\partial c_{im}}{\partial t} = \frac{\partial}{\partial t}\left[f(t) * c_m \right] \tag{12}$$

For first-order rate-limited mass transfer, the memory function follows an exponential form (Haggerty et al., 2000). However, heavy tailing BTCs are often observed in field tracer tests and they are attributed to the power-law memory function $f(t) = \tau_\gamma t^{-\gamma}/\Gamma(1-\gamma)$ where γ is the power-law index, $\Gamma(x)$ denotes the gamma function, and τ_γ is a scale factor for the power-law that is always set to be 1 [$T^{\gamma-1}$].

Note that a cutoff time is introduced to the memory function in some recent studies to capture the transition of BTC at late time from a power-law to an exponential trend, which is observed for solute transport in streams (Meerschaert et al., 2008; Aubeneau et al., 2014; Zhang et al., 2015). However, the late time transition is rarely observed in SWPP tests to the best of our knowledge, so the cutoff time is not considered in this study. Substituting equation (12) with the power-law memory function into equation (7) and then using the relation

$$\frac{\partial^\gamma c_m}{\partial t^\gamma} = \frac{\partial}{\partial t}\left[\frac{\tau_\gamma t^{-\gamma}}{\Gamma(1-\gamma)} * c_m \right] \tag{13}$$

one can get the fractional-in-time-and-space (FTS) model,

$$\begin{cases} \dfrac{\partial c_m}{\partial t} + \beta\tau_{\gamma_{inj}} \dfrac{\partial^{\gamma_{inj}} c_m}{\partial t^{\gamma_{inj}}} = -\dfrac{\kappa_v}{r}\dfrac{\partial}{\partial r} + \dfrac{a_{FS}\kappa_v}{r}\dfrac{\partial^\alpha}{\partial r^\alpha}, & 0 \le t < t_{inj} \\ \dfrac{\partial c_m}{\partial t} + \beta\tau_{\gamma_{cha}} \dfrac{\partial^{\gamma_{cha}} c_m}{\partial t^{\gamma_{cha}}} = -\dfrac{\kappa_v}{r}\dfrac{\partial}{\partial r} + \dfrac{a_{FS}\kappa_v}{r}\dfrac{\partial^\alpha}{\partial r^\alpha}, & t_{inj} \le t < t_{cha} \\ \dfrac{\partial c_m}{\partial t} + \beta\tau_{\gamma_{rest}} \dfrac{\partial^{\gamma_{rest}} c_m}{\partial t^{\gamma_{rest}}} = 0, & t_{cha} \le t < t_{rest} \\ \dfrac{\partial c_m}{\partial t} + \beta\tau_{\gamma_{pump}} \dfrac{\partial^{\gamma_{pump}} c_m}{\partial t^{\gamma_{pump}}} = \dfrac{\kappa_v}{r}\dfrac{\partial}{\partial r} + \dfrac{a_{FS}\kappa_v}{r}\dfrac{\partial^\alpha}{\partial (-r)^\alpha}, & t_{rest} \le t < t_{pump} \end{cases} \tag{14}$$

where $\partial^{\gamma} c_m/\partial t^{\gamma}$ with $\gamma=\{\gamma_{inj}, \gamma_{cha}, \gamma_{rest}$ and $\gamma_{pump}\}$ is the Riemann-Liouville fractional derivative; γ_{inj}, γ_{cha}, γ_{rest} , and γ_{pump} are the time fractional indexes for the injection, chasing, resting, and pumping stages, respectively, satisfying $0 < \gamma_{inj}, \gamma_{cha}, \gamma_{rest}, \gamma_{pump} \leq 1$; $\tau_{\gamma_{inj}}$, $\tau_{\gamma_{cha}}$, $\tau_{\gamma_{rest}}$, and $\tau_{\gamma_{pump}}$ are the scale factors for the corresponding fractional indexes. The reason that the time fractional index is stage-dependent is because the retention time distributions for stages after injection are modified with particles pre-existing in the immobile zone. The temporally dependent spatial operator remains the same as that of the FS model. The FTS model (equation (14)) considers both space and time fractional derivatives, which account for the non-local transport and power-law retention time of solutes in the immobile zone, respectively. Note that $\gamma = 1$ is equivalent to adding a retardation factor of $(1+\beta\tau_{\gamma})$ for c_m. This is because the power-law memory function $f(t) = \tau_{\gamma}\delta(t)$ when $\gamma \rightarrow 1$ and convolution of $\partial c_m/\partial t$ with $\tau_{\gamma}\delta(t)$ is $\tau_{\gamma}\partial c_m/\partial t$. The fractional-in-time (FT) model can be produced simply by letting the fractional order of space equal to 2. The immobile concentration $c_{im}(r,t)$ during the SWPP test can be calculated by employing equation (11). The total concentration $c_{tot}(r,t)$ which is defined as $c_{tot}(r,t) = \theta_m c_m + \theta_{im} c_{im}$ is obtainable as well.

The boundary and initial conditions for a four-stage SWPP test are

$$c_m(r_w, t) = c_{inj}, 0 < t < t_{inj} \tag{15}$$

$$c_m(r_w, t) = 0, t_{inj} \leq t < t_{cha} \tag{16}$$

$$\frac{\partial c_m(r_w, t)}{\partial r} = 0, t_{rest} \leq t < t_{pump} \tag{17}$$

$$c_m(r_e, t) = 0, 0 < t < t_{pump} \tag{18}$$

$$c_m(r,0) = c_{im}(r,0) = 0, r_w < r < r_e \quad (19)$$

where r_w is the wellbore radius [L]; r_e is the radial distance of the outer boundary which is sufficiently far from the wellbore so as not to affect the SWPP test results [L]. Note that the boundary condition for the resting stage is not specified because this stage only involves a temporal derivative, and the advection-dispersion operator is not included, thus spatial derivatives are not a concern. Therefore, the boundary condition, which is needed when the governing equation involves spatial derivative(s), is irrelevant for the resting stage.

A solver is developed to solve equation (14) using an implicit finite-difference method. The implicit Euler method is proven to be unconditionally stable if the Riemann-Liouville derivative is represented by the shifted Grünwald formula (Meerschaert and Tadjeran, 2003; Zhang, 2009). Details of the numerical scheme to solve the fractional models are elaborated in Appendix B.

4.2.2. First-order rate-limited mobile-immobile (FORMIM) model

A semi-analytical solution assuming the first-order rate-limited mass transfer between the mobile and immobile zones is proposed for a four-stage SWPP test. The semi-analytical solution can serve as a benchmark to test the numerical solver of the fractional model with an integer fractional index. Note that this calibration only holds for the FS model with $\alpha = 2$. If time fraction is considered such as in the FT or FTS model, the semi-analytical solution is not equal to that of the fractional model with $\gamma = 1$ because the FORMIM model assumes the memory function has an exponential form while the FT and FTS models assume the memory function is a Dirac delta function $\delta(t)$.

The basic scheme for the derivation of the semi-analytical solution is to obtain the analytical solution for each stage sequentially and to use the final distribution of a previous stage as the initial condition for the current stage. This operation is only valid for the FORMIM model because no memory effect is incorporated for the exponential memory function. For the fractional model with the power-law memory function, this operation will miss all the past concentration information at each grid point and is thus incorrect.

4.2.2.1. Injection and chasing stages

The governing equation of transport in the mobile zone during injection and chasing stages for the FORMIM model is

$$\frac{\partial c_m}{\partial t} + \beta \frac{\partial c_{im}}{\partial t} = -\frac{\kappa_v}{r}\frac{\partial c_m}{\partial r} + \frac{a\kappa_v}{r}\frac{\partial^2 c_{im}}{\partial r^2} \tag{20}$$

The immobile zone transport still satisfies equation (4). The outer boundary condition and initial conditions are already given in equations (18) and (19), respectively. The wellbore boundary condition is modified to

$$c_m(r_w, t) = c_{inj}\left[H(t) - H(t - t_{inj})\right], 0 < t < t_{cha} \tag{21}$$

where $H(t)$ is the Heaviside step function. The dimensionless form of the governing equation in the mobile zone (equation (20)) considering equation (4) is

$$\frac{\partial c_m'}{\partial \tau} = -\frac{1}{\rho}\frac{\partial c_m'}{\partial \rho} + \frac{1}{\rho}\frac{\partial^2 c_m'}{\partial \rho^2} - \varepsilon_m(c_m' - c_{im}') \tag{22}$$

where $c_m' = c_m/c_{inj}$, $c_{im}' = c_{im}/c_{inj}$, $\rho = r/a$, $\varepsilon_m = \omega a^2/\theta_m \kappa_v$, $\tau = \kappa_v t/a^2$. The dimensionless form of the immobile zone equation is

$$\frac{\partial c_{im}'}{\partial \tau} = \varepsilon_{im}(c_m' - c_{im}') \tag{23}$$

where $\varepsilon_m = \omega a^2/\theta_{im}\kappa_v$. Performing Laplace transforms on equations (21)-(23), the semi-analytical solution for injection and chasing stages can be obtained in the Laplace domain. The details of solution development are given in Appendix B. The dimensionless mobile concentration in the Laplace domain $\overline{c_m'}(\rho, s)$ is

$$\overline{c_m}'(\rho, s) = \left[1 - \exp(-\tau_{inj} s)\right] \exp\left(\frac{y - y_w}{2}\right) \frac{A_i(A_1^{1/3} y)}{s A_i(A_1^{1/3} y_w)} \tag{24}$$

where

$$A_1 = \varepsilon_m + s - \frac{\varepsilon_m \varepsilon_{im}}{s + \varepsilon_{im}} \tag{25}$$

$$y = \rho + \frac{1}{4A_1} \tag{26}$$

$$y_w = \rho_w + \frac{1}{4A_1} \tag{27}$$

where ρ_w is the dimensionless wellbore radius $\rho_w = r_w/a$, s is the Laplace transform variable corresponding to dimensionless time in the real domain, τ_{inj} is the dimensionless injection time; and $A_i(x)$ is the Airy function of the first kind. The dimensionless immobile concentration in the Laplace domain $\overline{c_{im}'}(\rho, s)$ is

$$\overline{c_{im}}'(\rho, s) = \frac{\varepsilon_{im} \overline{c_m}'(\rho, s)}{s + \varepsilon_{im}} \tag{28}$$

Numerical Laplace inversion is conducted using the de Hoog method (de Hoog et at., 1982). Detailed discussions on various numerical Laplace inversion methods for flow

and transport in the subsurface can be found in recent reviews by Hassanzadeh and Pooladi-Darvish (2007) and Wang and Zhan (2015).

4.2.2.2. Resting stage

The governing equation of the mobile zone during the resting stage is

$$\frac{\partial c_m}{\partial t} + \beta \frac{\partial c_{im}}{\partial t} = 0 \tag{29}$$

and the immobile zone equation is the same as equation (4). The initial condition for c_m is,

$$c_m(\rho, \tau_{rest} \to \tau_{cha}) = c_m(\rho, \tau_{cha}) \tag{30}$$

To solve the initial value problem, one more condition is required. Two assumptions are made here. The first assumption is that the total solute mass of the mobile and immobile zones is constant from the beginning to the end of the resting stage (equation (31)). The second assumption is that the mobile and immobile concentrations are the same in the resting stage when resting time goes to infinity (equation (32))

$$c_m'(\rho, \tau_{cha})\theta_m + c_{im}'(\rho, \tau_{cha})\theta_{im} = c_m'(\rho, \tau_\infty)\theta_m + c_{im}'(\rho, \tau_\infty)\theta_{im} \tag{31}$$

$$c_m'(\rho, \tau_\infty) = c_{im}'(\rho, \tau_\infty) \tag{32}$$

Note that τ_∞ means that the time in the resting stage goes to infinity, not including a pumping stage. Details of solving equation (29) are given in Appendix B. The dimensionless $c_m'(\rho,\tau)$ of the resting stage is

$$c_m'(\rho, \tau) = (c_2 - c_1)\exp\left[-(\varepsilon_m + \varepsilon_{im})\tau\right] + c_1 \tag{33}$$

where

$$c_1 = \frac{c_m'(\rho, \tau_{cha})\theta_m + c_{im}'(\rho, \tau_{cha})\theta_{im}}{\theta_m + \theta_{im}} \tag{34}$$

$$c_2 = c_m'(\rho, \tau_{cha}) \tag{35}$$

and the dimensionless $c_{im}'(\rho,\tau)$ of the resting stage is

$$c_{im}'(\rho,\tau) = -\frac{\varepsilon_{im}}{\varepsilon_m} c_m'(\rho,\tau) + (\frac{\varepsilon_{im}}{\varepsilon_m} + 1) c_1 \tag{36}$$

4.2.2.3. Pumping stage

The direction of advective flux is reversed in the pumping stage, thus the governing equation of the mobile zone for this stage is modified accordingly

$$\frac{\partial c_m}{\partial t} + \beta \frac{\partial c_{im}}{\partial t} = \frac{\kappa_v}{r} \frac{\partial c_m}{\partial r} + \frac{a\kappa_v}{r} \frac{\partial^2 c_m}{\partial r^2} \tag{37}$$

The initial conditions for the mobile and immobile zones are respectively

$$c_m(\rho, \tau_{pump} \to \tau_{rest}) = c_m(\rho, \tau_{rest}) \tag{38}$$

$$c_{im}(\rho, \tau_{pump} \to \tau_{rest}) = c_{im}(\rho, \tau_{rest}) \tag{39}$$

Chen and Woodside (1988) investigated the pumping problem without an immobile zone in the aquifer and proposed a closed-form analytical solution. A semi-analytical solution with an immobile zone is proposed based on their work (Appendix B). The mobile concentration in the Laplace domain

$$\overline{c_m'}(\rho, s)$$

is

$$\overline{c_m'}(\rho, s) = \pi e^{-\frac{\rho}{2}} \left\{ \int_{\rho_w}^{\rho} H_1 F(\lambda) d\lambda + \int_{\rho}^{\infty} H_2 F(\lambda) d\lambda - \int_{\rho_w}^{\infty} H_3 F(\lambda) d\lambda \right\} \tag{40}$$

where

$$F(\lambda) = \lambda e^{\frac{\lambda}{2}} B_3(\lambda) \tag{41}$$

$$H_1 = \frac{A_i(z)B_i(u)}{A_3^{1/3}} \tag{41}$$

$$H_2 = \frac{A_i(u)B_i(z)}{A_3^{1/3}} \tag{42}$$

$$H_3 = \frac{A_i(z)A_i(u)}{A_3^{1/3}} \frac{A_3^{1/3}B_i'(z_w) - \frac{1}{2}B_i(z_w)}{A_3^{1/3}A_i'(z_w) - \frac{1}{2}A_i(z_w)} \tag{43}$$

$$z = A_3^{1/3}\left(\rho + \frac{1}{4A_3}\right) \tag{44}$$

$$z_w = A_3^{1/3}\left(\rho_w + \frac{1}{4A_3}\right) \tag{45}$$

$$u = A_3^{1/3}\left(\lambda + \frac{1}{4A_3}\right) \tag{46}$$

$$A_3 = \varepsilon_m + s - \frac{\varepsilon_m \varepsilon_{im}}{s + \varepsilon_{im}} \tag{47}$$

$$B_3(\rho) = \frac{\varepsilon_m c_{im}'(\rho, \tau_{rest})}{s + \varepsilon_{im}} + c_m'(\rho, \tau_{rest}) \tag{48}$$

Here $A_i'(x)$ is the derivative of the Airy function of the first kind, $B_i(x)$ is the Airy function of the second kind and $B_i'(x)$ is the derivative of the Airy function of the second kind. The immobile concentration in Laplace domain $\overline{c_{im}'}(\rho, s)$ is

$$\overline{c_{im}}'(\rho, s) = \frac{\varepsilon_{im}\overline{c_m}'(\rho, s) + c_{im}'(\rho, \tau_{rest})}{s + \varepsilon_{im}} \tag{49}$$

Both $\overline{c_m}'(\rho, s)$ and $\overline{c_{\imath m}}'(\rho, s)$ are inversed to the real domain using the de Hoog method.

4.3. Discussion

4.3.1. Calibration

Since the semi-analytical solution of the FORMIM model and the fractional models for SWPP tests are novel, no previous work could be used to calibrate these solutions. The way adopted for calibration here is to compare the FORMIM model and the FS model with α=2, which are supposed to be the same theoretically. Note that the FTS model with α=2 and γ=1 is not equivalent to the FORMIM model because γ=1 introduces a retardation effect for the mobile zone. Figure 4.1 displays the calibration results for the mobile and immobile zones. A very good match between the semi-analytical and numerical solutions is obtained for the dimensionless concentration up to the scale of 10^{-6}, which is sufficient for practical use in most cases. The numerical solution is slightly affected by the discretization of time and space. Here the uniform time and space steps are chosen to be 0.02 hours and 0.02 m, respectively, considering the computational cost.

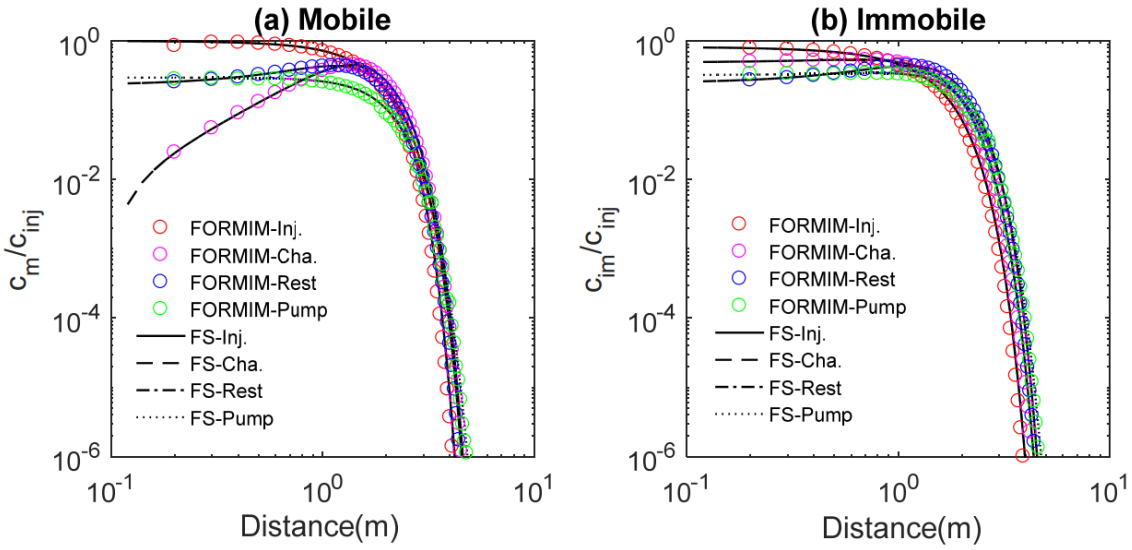

Figure 4.1 Calibration of the FORMIM model and the FS model with α = 2 at the end of each stage of the SWPP test, including injection, chasing, resting and pumping. (a) Distribution curve of the relative mobile concentration at each stage; (b) Distribution curve of the relative immobile concentration at each stage.

4.3.2. Interpretation of fractional space and time derivatives

The fractional space derivative controls the strength of non-local transport in space. Figure 4.2 displays the mobile concentration distribution at the end of each stage of the SWPP test with α varying from 1.4 to 2 and γ = 1, which is equivalent to the FS model with a retardation factor of 1+β. Herein, both the FS and ADE models consider the retardation factor implicitly. Fast movement of the leading edge of the plume opposite to the wellbore is observed for the fractional models (α = {1.4, 1.6, 1.8}) during injection. The smaller the fractional space index, the farther the solutes moves away from the injection well. In the pumping stage (Figure 4.2(d)), the leading edge of the plume moves toward the wellbore and the spatial distribution of concentration is expected to skew toward the flow direction. The reason that the observed skewness is opposite to the

flow direction is because the initial mass before pumping is more concentrated near the wellbore. The spatial distributions of concentration in the chasing and resting stages are identical when the molecular diffusion is neglected because the memory function is $\delta(t)$ when $\gamma = 1$. Note that it is impossible that the concentration remains the same during the resting stage in the real world due to molecular diffusion, no matter how small it is. Here we neglect molecular diffusion for simplification purpose and attribute the mass change in the mobile zone to the mobile-immobile mass transfer. The influence of the fractional time derivative on solute distribution is shown in Figure 4.3 where α is set to be 2 and γ varies over a range of values from 0.4 to 1. Early arrival of the leading edge of the plume is not observed due to the non-zero initial mass distribution before pumping. The effect of non-locality in time is similar to that of retardation, with a smaller time fractional index corresponding to a larger retardation factor. Note that the concentration profiles are not constant during the resting stage because tracer particles in the immobile zone are released.

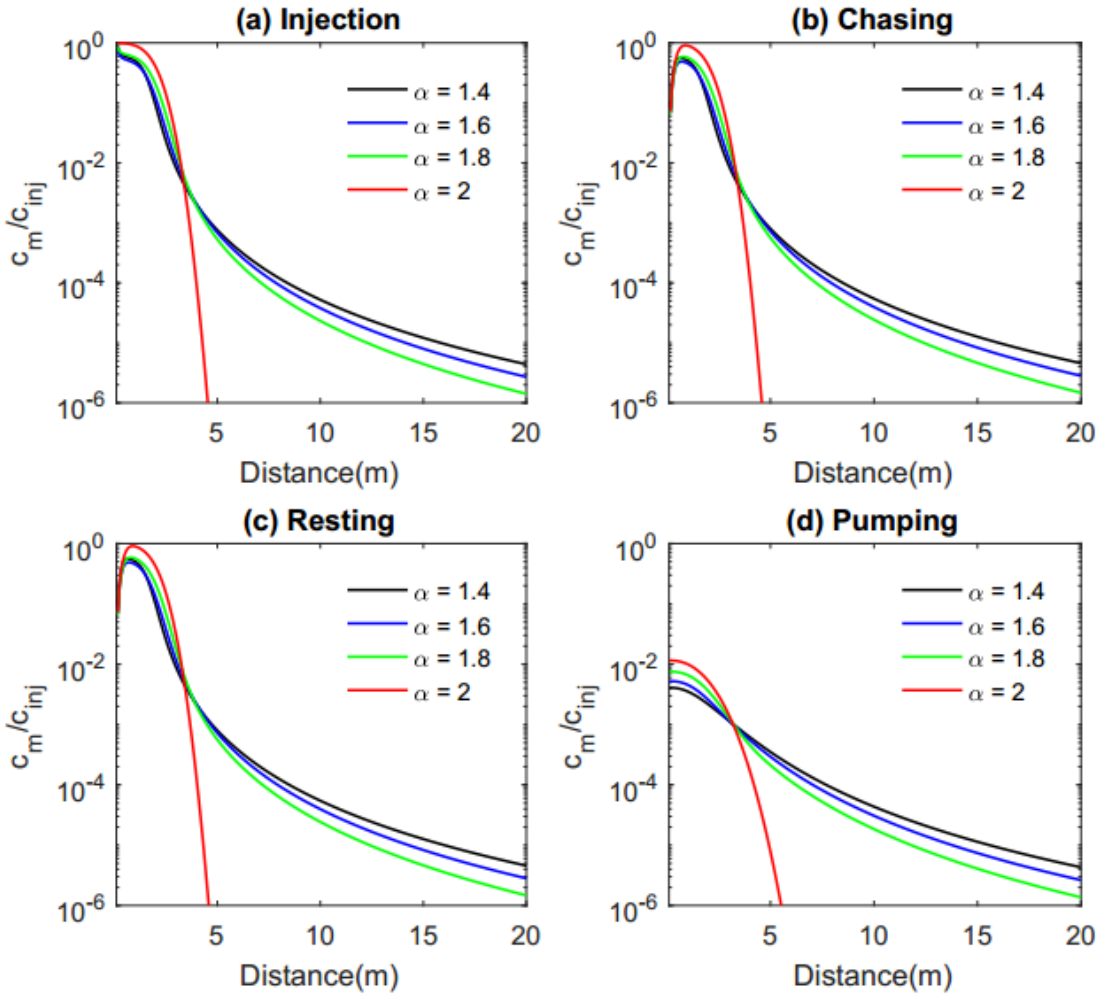

Figure 4.2 Distribution curves of the mobile concentration at the end of each stage of the SWPP test using the FS model with α = 1.4, 1.6, 1.8 and 2 and retardation factor (1+β). (a) Distribution curves at the end of injection; (b) Distribution curves at the end of chasing; (c) Distribution curves at the end of resting; (d) Distribution curve after 50 hours of pumping.

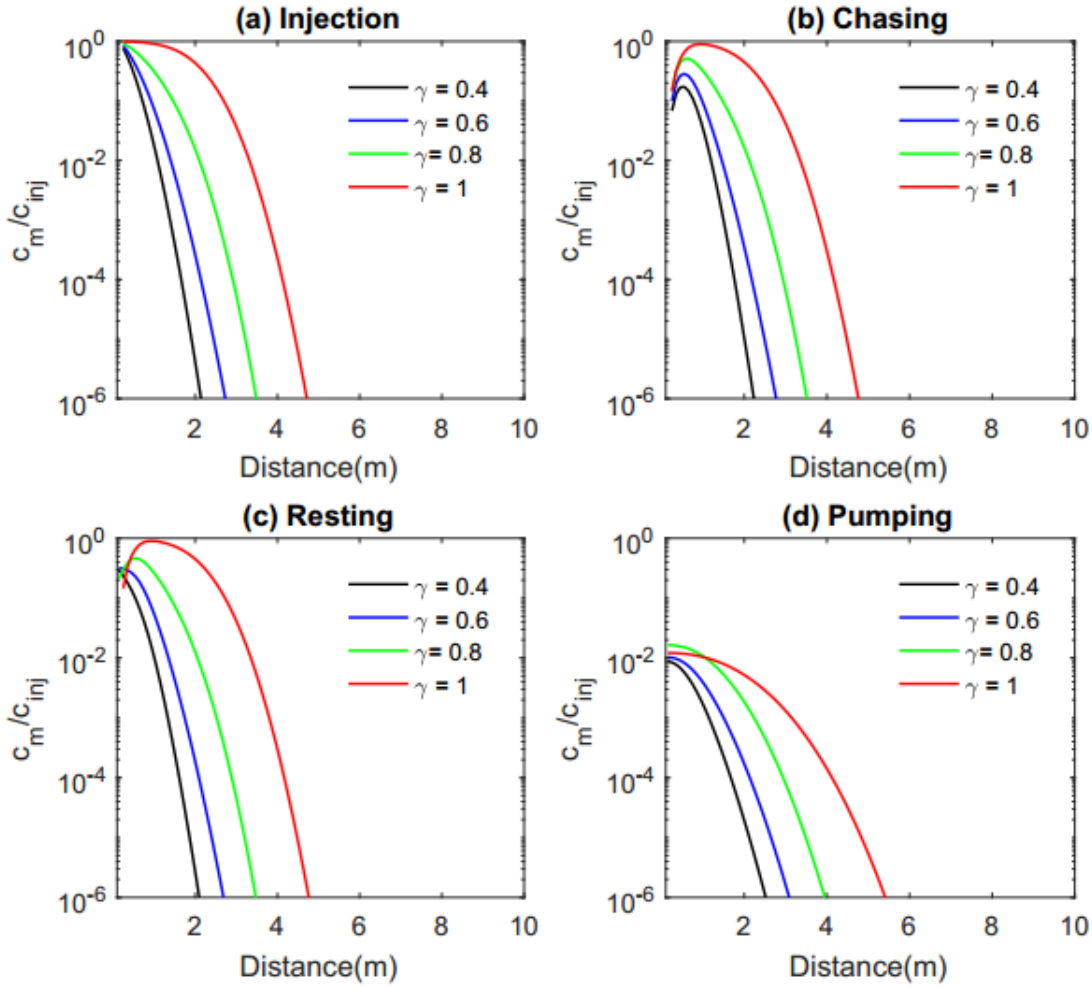

Figure 4.3 Distribution curves of the mobile concentration at the end of each stage of the SWPP test using the FT model with γ = 0.4, 0.6, 0.8 and 1. (a) Distribution curves at the end of injection; (b) Distribution curves at the end of chasing; (c) Distribution curves at the end of resting; (d) Distribution curves after 50 hours of pumping.

The BTC comprises the primary data that are obtained from a field SWPP test. Figure 4.4(a) shows the BTCs of the FS model with different α. The concentration increases first due to the injected chaser and tailing is observed for $\alpha<2$ at late time. The BTC of the case with local transport (α = 2) drops exponentially and the BTCs of the

non-local transport ($\alpha < 2$) are approximately linear at late time. Two observations are worthy of note. Firstly, the early arrival that is the characteristic of the FS model is not observed. This is because the initial mass distribution before pumping is nonzero and most particles are concentrated near the wellbore. Secondly, tailing of late time is observed for $\alpha<2$. The reason for tailing is because a portion of the tracer particles retains at the far side during pumping due to the preferential flow toward the wellbore, and such particle retention has the same effect as particle immobilization on the BTCs. Figure 4.4(b) displays BTCs with varying γ. The power-law memory function with index γ represents subdiffusive transport and is characterized by a linear decrease of the BTC at late time. Note that the BTC is less sensitive to α compared with γ.

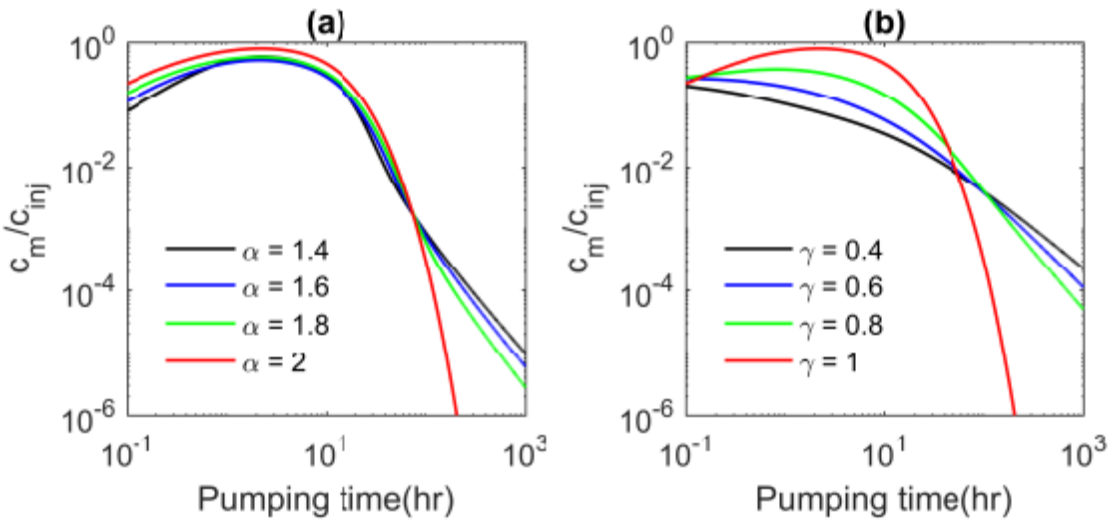

Figure 4.4 BTCs during the pumping stage. (a) FS model with α = 1.4, 1.6, 1.8 and 2; (b) FT model with γ = 0.4, 0.6, 0.8 and 1.

4.3.3. Capacity ratio

An essential assumption made in all of the above models is that the aquifer may be described by a physical model consisting of mobile and immobile zones. Therefore, the capacity ratio β, which represents the volumetric ratio between the immobile and mobile zones, is an important factor to consider. Figure 4.5(a) shows the BTCs of the FS model with α = 1.8 and retardation factor (1+β), for which β varies from 0 to 1. The BTCs move upward with β rising and drop linearly at the same rate at late time. Figure 5(b) shows the BTCs of the FT model with γ = 0.8. Note that the BTC with β = 0 is actually equivalent to the BTC of ADE model because neither non-local transport in space nor in time is considered. It is found that β determines the location of the BTC, but does not affect its shape.

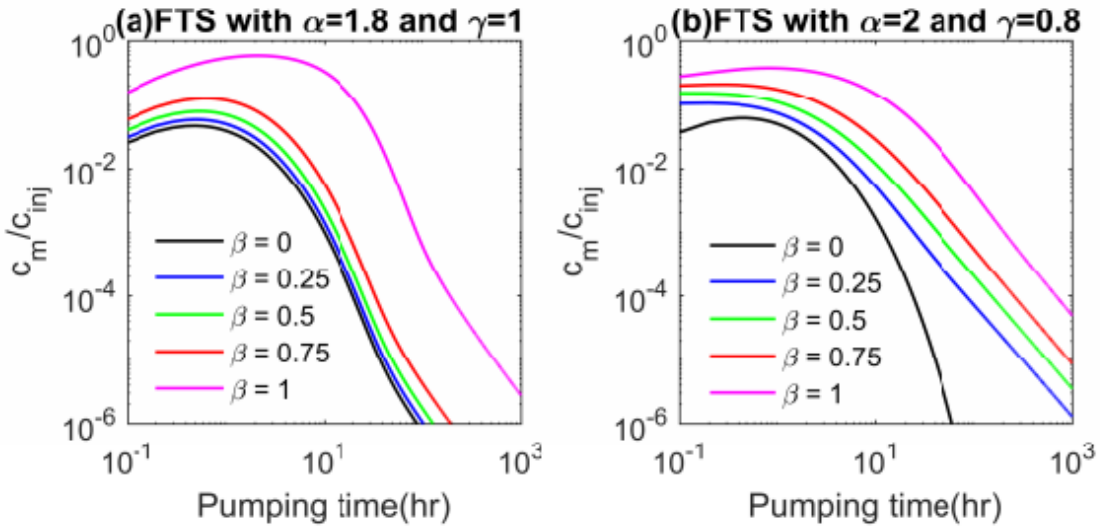

Figure 4.5 BTCs with β = 0, 0.25, 0.5, 0.75 and 1. (a) FS model with α = 1.8; (b) FT model with γ = 0.8.

4.3.4. Mass distribution

Solute mass distribution is another concern in the SWPP test. Here we define $c_m\theta_m/c_{inj}$ as the relative mass in the mobile zone. Figure 4.6 compares the mobile mass distribution predicted by different models, including ADE, FS (α = 1.8) and FT (γ = 0.8). Figures 4.6(a)-(d) correspond to the mass distribution at the end of injection, chasing, resting, and 50 hours after pumping, respectively. Parameters are from Table 4.1. The mobile mass distribution of the FS model shows a heavy leading plume compared with the other two models. Note that the mobile mass of the FT model near the wellbore increases during the resting stage due to the released particles from the immobile zone.

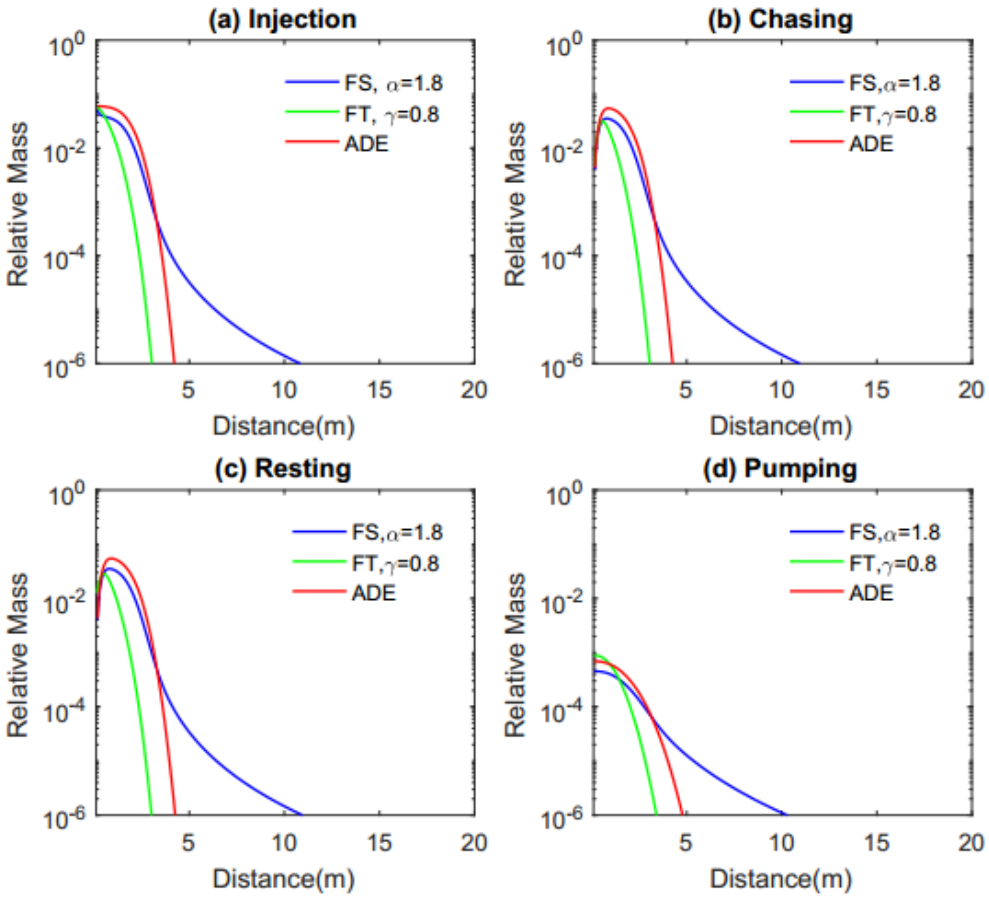

Figure 4.6 Relative mobile mass distributions at the end of each stage of the SWPP test using the ADE, FS (α =1.8) and FT (γ=0.8) models. (a): Mass distribution at the end of injection stage (t_{inj} = 10 hours); (b): Mass distribution at the end of chasing stage (t_{cha} = 3 hours); (c): Mass distribution at the end of resting stage (t_{rest} = 10 hours); (d): Mass distribution after 50 hours of pumping.

Table 4.1 Model settings for the validation of the FORMIM model and the FS model with $\alpha = 2$

Parameters	Value
Injection, chasing, pumping rates (m3/hr)	0.5, 0.5, 0.5
Tracer concentration (mmol/m3)	1
Injection, chasing, resting and pumping	10, 3, 10, 10
Mobile porosity, immobile porosity	0.06, 0.06
Mass transfer coefficient (1/hr)	0.01
Dispersivity (m)	0.3

4.3.5 Operational factors

Two operational factors that may affect the BTCs of SWPP tests are the duration of each stage and pumping rate. The duration affects time-dependent processes like the mass transfer between the mobile and immobile zones and the pumping rate determines the advective timescale. Figure 4.7 plots the BTCs of the injection, chasing, and resting stages with different injection times using the ADE model and FTS model with $\alpha = 1.8$ and $\gamma = 0.8$. The ADE model is more sensitive to the injection duration and the injection duration does not affect the slope of the BTC at late time (Figure 4.7(a)). For different chasing durations, the peak concentration decreases and shifts to the right with the increasing chasing time (Figure 4.7(b)). In addition, the concentration at the early stage of pumping is strongly affected by the chasing time. For different resting durations, the BTC of the ADE model does not change due to the zero advection-dispersion operator and the BTC of the FTS model at late time is gentler with increasing resting duration (Figure 4.7(c)). Note that the resting duration must be much larger than the injection or chasing duration in order to observe obvious shifts of BTCs. Figure 4.8 shows the influence of pumping rate on the shape of BTCs. As one can see, the pumping rate,

which is proportional to the radial advective velocity, determines the arrival time of the peak concentration, but has little influence on the peak value and late time behavior.

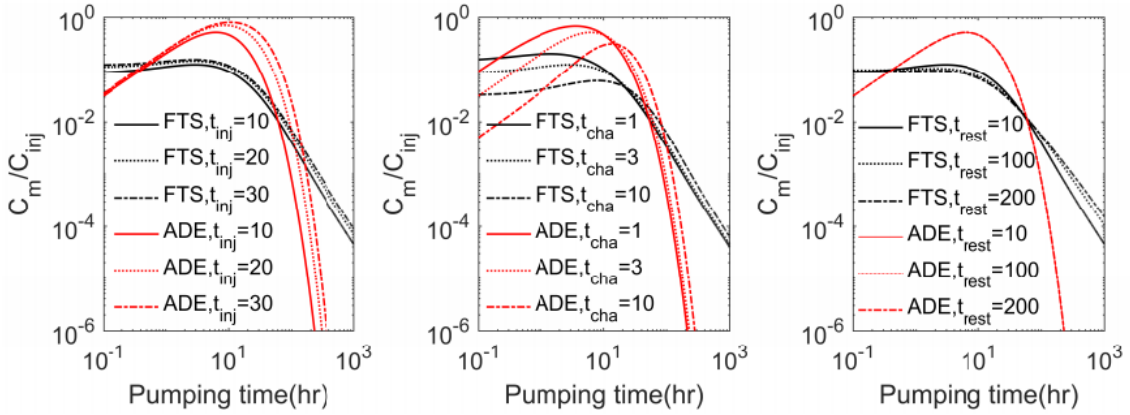

Figure 4.7 BTCs with different durations for injection, chasing and resting stages using the FTS model (α = 1.8, γ = 0.8) and the ADE model. (a) Injection duration t_{inj} = 10, 20 and 30 hours; (b) Chasing duration t_{cha} = 1, 3, 10 hours; (c) Resting duration t_{rest} = 10, 100 and 200 hours. Note that the BTCs of the ADE model overlap with each other in the resting stage in (c).

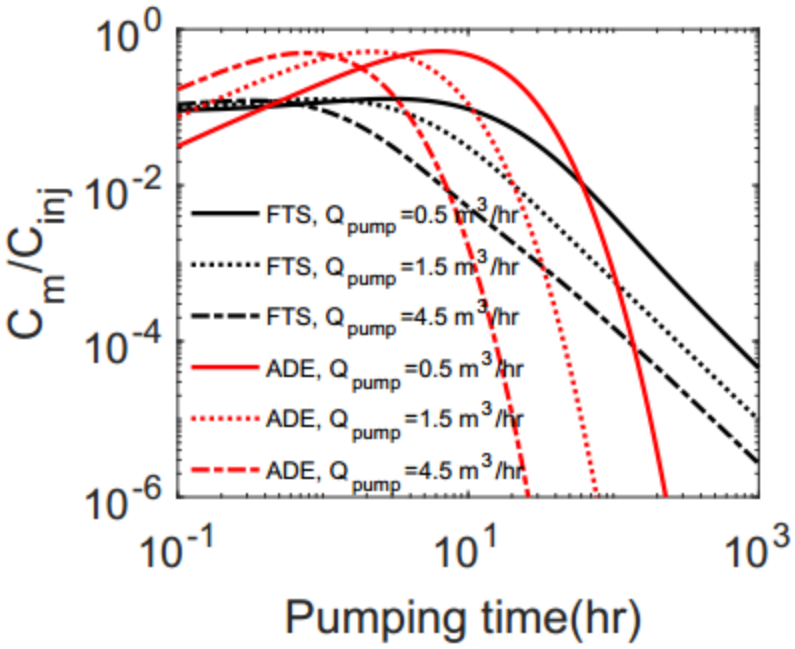

Figure 4.8 BTCs with Q_{pump} = 0.5, 1.5 and 4.5 m^3/hr using the FTS model (α = 1.8, γ = 0.8) and the ADE model.

4.3.6 Time-dependent γ

Figure 4.9 shows the BTCs with varying time-fractional index. It is found that the slope of late time BTC is determined by γ_{pump}. A smaller γ_{inj}, γ_{cha} or γ_{rest} will move the BTC downward because a smaller index indicates greater retention and more particles rest in the immobile zone when pumping starts.

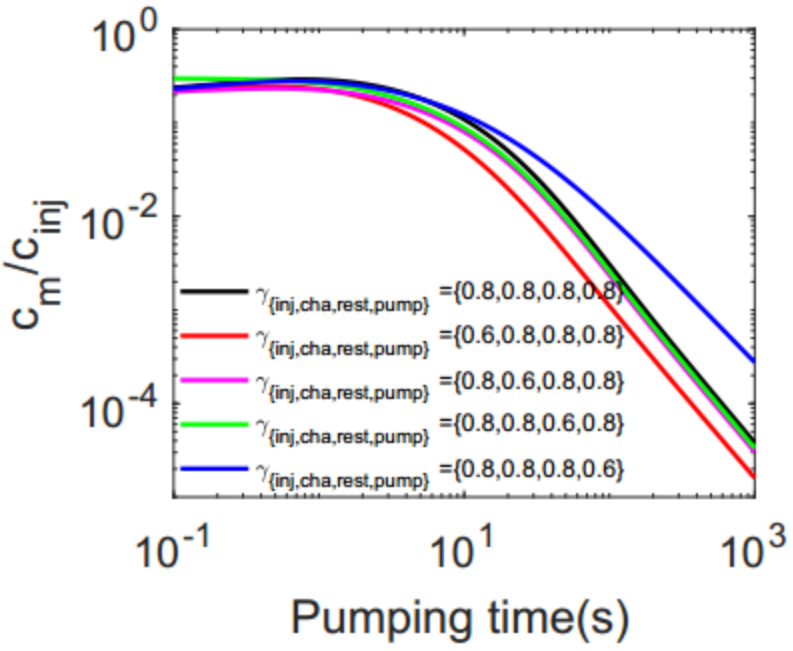

Figure 4.9 BTCs with varying time-fractional index for each stage.

4.4. Modeling of SWPP Tests

In this section, we will apply the above developed theory to interpret multiple SWPP injection experiments reported in Matter et al. (2007), Assayag et al. (2009), and Yang et al. (2014). Detailed description of the study site, borehole information, and geological setting can be found in Assayag et al. (2009) and Yang et al. (2014). In brief, the borehole TW3 located at the Lamont–Doherty Earth Observatory test site in the Newark basin was drilled to the depth of 457 m, penetrating three major permeability zones at the depth of 230 m, 300 m and 360 m, respectively. The experimental data in this study were collected from a shallow zone (depth of 230 m) at the contact of Palisade dolerite sill and underlying metamorphosed sedimentary rock. Downhole imaging of the formation shows distinctive fractures within the injection zone and well log analysis

Table 4.2 Experimental data of S1 and S2 tests

Test	Injection	Injection	Injection	Chaser	Resting	Pumping	Pumping
S1	232-240	7.78	3	208	7	12	64.7
S2	232-240	11.4	3	193	5	12.06	96

shows that the porosity is between 0.01 and 0.1. Parameters of two SWPP tests are shown in Table 4.2.

Figure 4.10 displays the experimental data of S1 and S2 tests with BTCs predicted by the FTS model. Three observations from the field data are worth noting. Firstly, the early concentration of the S1 test at the pumping stage is much smaller than that of the S2 test. This observation could be attributed to the smaller amount of injected tracer and the two days longer duration in the resting stage for the S1 test. Some preliminary simulations with the ADE model demonstrate that a larger injected tracer volume results in a flatter BTC near the peak concentration and has no obvious influence on the peak concentration. Therefore, a temporal process needs to be considered while interpreting the field data. Secondly, an increase for concentration in the early stage of pumping is expected, but it is not seen in the field data. A possible reason is that the chaser volume is much smaller than the injected tracer volume and the influence of the chaser is further weakened by wellbore storage which is not considered in the analytical or fractional models. Thirdly, the slope of the BTC after the advective timescale in the S2 test is linear in a log-log plot. The advective timescale is $\int_0^L 1/vdr$ for radial flow at steady state. A simple way to estimate it is to take the injection timescale, which is about 3 hours (~10^4 s), as the advective time scale in the pumping stage because the pumping

rate is close to the injection rate. The linear decline of concentration after the advective timescale indicates a power-law memory function, so the FTS model is chosen for parameter calibration.

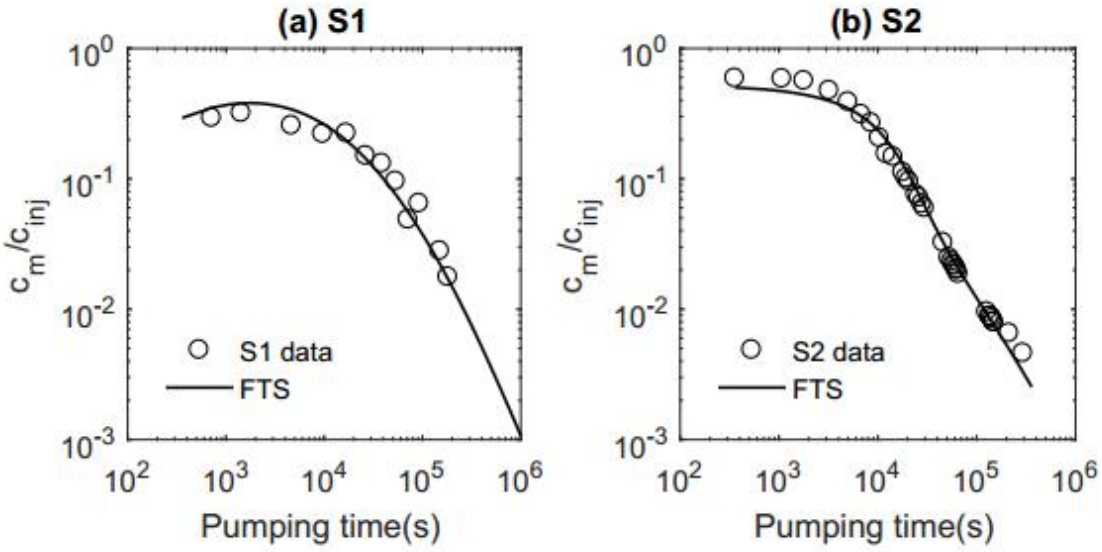

Figure 4. 10 Experimental data of the S1 and S2 tests and predicted BTCs by the FTS model. S1(left): FTS model with γ=0.8691 and α=1.9201; S2(right): FTS model with γ=0.8142 and α=1.9051.

The fractional dispersivity and effective porosity cannot be inverted from the BTC independently due to the poor constraints on the mean advective velocity (Becker and Shapiro, 2003; Le Borgne and Gouze, 2008). Therefore, the mobile porosity is set initially to be 0.06 according to the well log interpretation and the immobile porosity is calibrated manually until the predicted BTC moves to the range of the data points. Three parameters, including a_{FS}, γ and α, are then fitted using a non-linear least square solver in MATLAB. Note that the time-fractional indexes in equation (14) are assumed to be the same for all four stages to reduce the model degrees of freedom, especially when the

spatial and temporal information in the first three stages is not available, which is not uncommon in actual implementation of SWPP tests. For S1 test, the calibrated values for each parameter are θ_{im}=0.068, a_{FS}=0.7134, γ=0.8691, and α=1.9201. For S2 test, the calibrated values are θ_{im}=0.062, a_{FS}=0.1007, γ=0.8142, and α=1.9051. a_{FS} varies a lot because larger a_{FS} and smaller γ have the same effect on the BTC, specifically, by lowering the peak and flattening the BTC. One notable point is that the FT model can also fit the data well because the tailing caused by the non-local transport in space can be attributed to the non-local behavior in time. The reason we keep the non-local transport in space is that many fractures have been observed from the wellbore image, thus preferential flow is believed to play an important role at the site where the S1 and S2 tests are conducted.

The BTC of the S1 test actually does not show tailing because of the short pumping duration, and the BTC of the S2 test exhibits tailing, but the resolution of the normalized measured concentration (~10^{-3}) in the S2 test may not be fine enough to verify the model at very late time with the normalized concentration at the scale ~10^{-5}. Here we test our model on a high-resolution dataset (Gouze et al., 2008; Le Borgne and Gouze, 2008). The injection duration t_{inj} and the chasing duration t_{cha} are 4 minutes and 40 minutes, respectively, and the resting stage is skipped. Mobile porosity is ~0.38 based on the core tests. Figure 4.11 shows the fitting of the BTC. The parameter set (θ_m, θ_{im}, a_{FS}) is calibrated to be (0.30, 0.28, 0.005). The issue mentioned in Le Borgne and Gouze (2008) that the CTRW model with a consistent waiting time distribution during the pumping stage cannot recover the entire BTC is encountered here as well because the measured

BTC exhibits slope transition (from ~ -2 to ~ -1.5) at late time (> ~2×10^4 s). Le Borgne and Gouze (2008) used a double-exponent CTRW model to fit the entire BTC by setting a different waiting time distribution at the beginning of transition (2×10^4 s). This approach can be applied to the FTS model as well in terms of fitting. However, the reason for the slope change at very late time is still an open question. A possible explanation is that the true velocity field may play a more important role at the late time of pumping (Le Borgne and Gouze, 2008).

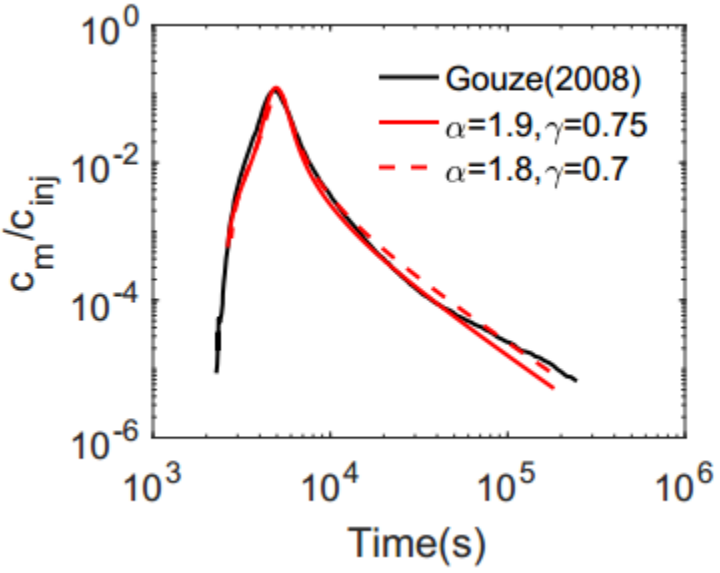

Figure 4.11 Experimental data of Gouze et al. (2008) and predicted BTCs by the FTS model. Black solid: BTC from Gouze et al. (2008) with t_{inj}=4 min and t_{cha}=40 min; Red solid: FTS model with α=1.9 and γ=0.75; Red dashed: FTS model with α=1.8 and γ=0.7

4.5. Applicability and limitation

Another interesting question is whether the fractional model is the only model that could be used to interpret the SWPP test with the observations mentioned above. Actually, many other models have been proposed to match the field data, such as an

advection-driven model (Becker and Shapiro, 2003), a diffusion-driven model (Haggerty et al., 2001) or a mobile-immobile model (Liu et al., 2010). All these models, including the ADE model, are capable of matching the field data at the advective time scale. Most of the previous work effort was put on the prediction and physical explanation for the late time behavior. The BTCs in the pumping stage predicted by the ADE model decline exponentially at late time and the theoretical late time slope of the traditional double-porosity model is -1.5 (Tsang, 1995). However, the BTCs of most field data drop linearly at late time, meaning that it satisfies a power-law function instead of an exponential function. In addition, the magnitude of slope of field data decline is usually greater than 1.5 in log-log plots. Therefore, temporally related processes such as multi-rate mass transfer or power-law waiting time distribution are employed to give a better prediction for the late time behavior. Table 4.3 compiles the major contribution to the modeling of SWPP tests in the last two decades. The late time slope in this study is about -1.8. As one can see, the multi-rate, CTRW and FTS models are powerful in predicting BTCs with a wide range of tail slopes. The multipath model assuming mass transport in highly channelized aquifers with distributed channel apertures shows the same ability to model the tailing effect with various decline slopes (Becker and Shapiro, 2003).

Table 4.3 List of models developed for simulating SWPP tests

Authors	Model	Late-time	Test site
Tsang (1995)	Double-porosity	-1.5	N[a]
Haggerty et al. (2001)	Multi-rate diffusion	-2.1 ~ -2.8	WIPP
Becker and Shapiro (2003)	Multipath	-4.5	Mirror lake
Le Borgne and Gouze (2008)	Double exponent CTRW	-1.6	Ses Sitjoles
Liu et al. (2010)	FORMIM	-2.3	MADE
Hansen et al. (2016)	CTRW	-2.3	MADE

a. No field data supplied.

The SWPP test is designed to investigate time-dependent processes, such as matrix diffusion or mobile-immobile mass transfer. A unique configuration of the SWPP test, particularly, the reversal of flow, is designed to mitigate the influence of aquifer heterogeneity that might obscure a time-dependent process in the multi-well tracer tests. However, the advantage of the SWPP test is also a shortcoming in terms of the detection of aquifer heterogeneity. How to choose a proper model to interpret the time-dependent process depends on the observed BTC data. Here we draw some guidelines from the literature and our study to help choose the proper model. Firstly, if the BTCs do not show tailing yet due to the short pumping (pumping duration less than the intersection point between the power-law decline and exponential decline as shown in Figure (4)), all models mentioned above should be able to recover the BTCs and the simplest ADE model is the first option because it has the least number of parameters to fit. By doing so, it does not necessarily mean that there is no non-local behavior in time or space. In respect to the non-locality in space, it is difficult to quantify the degree of non-locality from the BTCs before the intersection point (see Figure 4(a)) due to the negligible

difference of BTCs obtained from the ADE model and the FS model. For non-locality in time, the lower peak concentration (see Figure 4(b)) can be fitted with a larger dispersivity using the ADE model. Secondly, if the pumping duration is long enough and the slope of late time decline is close to -1.5, the double porosity model (Tsang, 1995) is a good choice and the time related behavior can be attributed to the matrix diffusion. Note that the characteristic of BTCs with a late time slope of -1.5 is valid in both homogeneous and heterogeneous aquifers, but BTCs generated by the ADE model strongly depend on the degree of heterogeneity (Tsang, 1995). Thirdly, if the objective of the SWPP test is the long-term effect of remediation or if the BTC exhibits linear decline with a slope whose magnitude is greater than 1.5, mobile-immobile, multi-rate, CTRW, and FTS models are all capable of explaining the tailing behavior. Note that only the FTS model considers the effect of preferential flow among those studied for SWPP tests.

4.6. Conclusions

This study proposes a time-dependent fractional model to simulate four-stage SWPP tests conducted at a deep fractured aquifer. An implicit finite-difference solver is developed to solve the system of fractional governing equations and the numerical method is unconditionally stable. Semi-analytical solutions for each stage of the SWPP test are developed as well with the assumption of a first-order rate-limited mass transfer between the mobile and immobile zones. The following conclusions can be drawn from the study.

(1) The FTS model is capable of recovering the long-time tailing of the SWPP test. Non-local transport in both time and space can produce the tailing effect. A smaller fractional index results in a lower peak concentration and a larger late time slope for the BTC.

(2) Capacity ratio is an important parameter that affects the peak concentration of the BTC. A larger capacity ratio results in a higher peak concentration. The peak concentration is also heavily dependent on the operational parameters, such as the duration of injection or chasing stage and the pumping rate.

(3) A smaller time-fractional index in the injection, chasing, or resting stage will result in a less mobile mass at the beginning of pumping, and thus the BTC moves downward. The slope of the late time BTC is determined by the space-fractional index over all stages and the time-fractional index in the pumping stage.

References

Assayag, N., J. Matter, M. Ader, D. Goldberg, and P. Agrinier (2009), Water-rock interactions during a CO_2 injection field-test: Implications on host rock dissolution and alteration effects, *Chem. Geol., 265*(1-2), 227-235.

Aubeneau A.F., B. Hanranhan, D. Bolster and J. L. Tank (2014), Substrate size and heterogeneity control anomalous transport in small streams, *Geophys. Res. Lett.*, 41, 8335–8341, doi:10.1002/2014GL061838.

Baleanu, D., K. Diethelm, E. Scalas, and J. J. Trujillo (2012), Fractional Calculus-Models and Numerical Methods, World Scientific Pub., Singapore.

Becker, M.W. and A.M. Shapiro (2003), Interpreting tracer breakthrough tailing from different forced-gradient tracer experiment configurations in fractured bedrock, *Water Resour. Res., 39,* 1024, doi:10.1029/2001WR001190.

Benson, D. A., S. W. Wheatcraft, and M. M. Meerschaert (2000), Application of a fractional advection-dispersion equation, *Water Resour. Res., 36*(6), 1403-1412, doi:10.1029/2000WR900031.

Benson, D. A., C. Tadjeran, M. M. Meerschaert, I. Farnham, and G. Pohll (2004), Radial fractional-order dispersion through fractured rock, *Water Resour. Res., 40*, W12416, doi:10.1029/2004WR003314.

Berkowitz, B., and H. Scher (1998), Theory of anomalous chemical transport in random fracture networks, *Phys. Rev. E, 57*(5), 5858-5869.

Berkowitz, B., A. Cortis, M. Dentz, and H. Scher (2006), Modeling non-Fickian transport in geological formations as a continuous time random walk, *Rev. Geophys.*, *44*(2).

Chen, C. S., and G. D. Woodside (1988), Analytical solution for aquifer decontamination by pumping, *Water Resour. Res.*, *24*(8), 1329-1338, doi:10.1029/WR024i008p01329.

Cho, Y., K. Han, N. Kim, S. Park, and Y. Kim (2013), Estimating in situ biodegradation rates of petroleum hydrocarbons and microbial population dynamics by performing single-well push-pull tests in a fractured bedrock aquifer, *Water Air Soil Poll.*, *224*(2), 1364.

de Hoog, F.R., J.H. Knight and A.N. Stokes (1982), An improved method for numerical inversion of Laplace transforms. *SIAM J. Sci. Stat. Comput.*, *3*(3), 357–366.

Dentz, M., and B. Berkowitz (2003), Transport behavior of a passive solute in continuous time random walks and multirate mass transfer, *Water Resour. Res.*, *39*, 1111, doi:10.1029/2001WR001163.

Dentz, M., A. Cortis, H. Scher, and B. Berkowitz (2004), Time behavior of solute transport in heterogeneous media: transition from anomalous to normal transport, *Adv. Water Resour.*, *27*(2), 155-173.

Dimitrov, Y. (2014), Numerical approximations for fractional differential equations, *J. of Frac. Cal. and App.*, 5(22), 1-45.

Falta, R. W. (1984), Analysis and interpretation of single-well and two-well tracer dispersion experiments in stratified aquifers, 101 pp, Auburn Univ., Ala.

Gelhar, L. W., and M. A. Collins (1971), General analysis of longitudinal dispersion in nonuniform flow, *Water Resour. Res.*, *7*(6), doi:10.1029/WR007i006p01511.

Ghergut, J., H. Behrens, and M. Sauter (2016), Petrothermal and aquifer-based EGS in the Northern-German Sedimentary Basin, investigated by conservative tracers during single-well injection-flowback and production tests, *Geothermics*, *63*, 225-241.

Güven, O., R. W. Falta, F. J. Molz, and J. G. Melville (1985), Analysis and interpretation of single-well tracer tests in stratified aquifers, *Water Resour. Res.*, *21*(5), 676-684, doi:10.1029/WR021i005p00676.

Haddad, A. S., H. Hassanzadeh, J. Abedi, Z. X. Chen, and A. Ware (2015), Characterization of scale-dependent dispersivity in fractured formations through a divergent flow tracer test, *Groundwater*, *53*, 149-155.

Hadermann, J. and W. Heer (1996), The Grimsel (Switzerland) migration experiment: integrating field experiments, laboratory investigations and modeling, *J. Contam. Hydrol.*, *21*, 87-100.

Haggerty, R., and S. M. Gorelick (1995), Multiple-rate mass-transfer for modeling diffusion and surface-reactions in media with pore-scale heterogeneity, *Water Resour. Res.*, *31*(10), 2383-2400, doi:10.1029/95WR10583.

Haggerty, R., S. A. McKenna, and L. C. Meigs (2000), On the late-time behavior of tracer test breakthrough curves, *Water Resour. Res.*, *36*(12), 3467-3479, doi:10.1029/2000WR900214.

Haggerty, R., S. W. Fleming, L. C. Meigs, and S. A. McKenna (2001), Tracer tests in a fractured dolomite 2. Analysis of mass transfer in single-well injection-withdrawal tests, *Water Resour. Res.*, *37*(5), 1129-1142, doi:10.1029/2000WR900334.

Hansen, S.K., B. Berkowitz, V. V. Vesselinov, D. O'Malley and S. Karra (2016), Push-pull tracer tests: Their information content and use for characterizing non-Fickian, mobile-immobile behavior, *Water Resour. Res.*, *52*, 9565-9585, doi:10.1002/2016WR018769.

Hassanzadeh, H., and M. Pooladi-Darvish (2007), Comparison of different numerical Laplace inversion methods for engineering applications, *Appl. Math. Comput.*, *189*(2), 1966-1981.

Istok, J. D., J. A. Field, M. H. Schroth, B. M. Davis, and V. Dwarakanath (2002), Single-well "push-pull" partitioning tracer test for NAPL detection in the subsurface, *Environ. Sci. Technol.*, *36*(12), 2708-2716.

Le Borgne, T., and P. Gouze (2008), Non-Fickian dispersion in porous media: 2. Model validation from measurements at different scales, *Water Resour. Res.*, *44*, W06427, doi:10.1029/2007WR006279.

Liu, G., C. Zheng, G. R. Tick, J. J. Butler. Jr. and S. M. Gorelick (2010), Relative importance of dispersion and rate-limited mass transfer in highly heterogeneous porous media: Analysis of a new tracer test at the Macrodispersion Experiment (MADE) site, *Water Resour. Res.*, *46*, W03524, doi:10.1029/2009WR008430.

Matter, J. M., T. Takahashi, and D. Goldberg (2007), Experimental evaluation of in situ CO_2-water-rock reactions during CO_2 injection in basaltic rocks: Implications for

geological CO_2 sequestration, *Geochem. Geophy. Geosy., 8*, Q02001, doi:10.1029/2006GC001427.

Meerschaert, M. M., and C. Tadjeran (2003), Finite difference approximations for fractional advection-dispersion flow equations, *J. Comput. Appl. Math., 172*(1), 65-77.

Meerschaert M. M., Y. Zhang and B. Baeumer (2008), Tempered anomalous diffusion in heterogeneous systems, *Geophys. Res. Lett.*, 35, L17403, doi:10.1029/2008GL034899.

Nordqvist, R., and E. Gustafsson (2002), Single-well injection-withdrawal tests (SWIW) literature review and scoping calculations for homogeneous crystalline bedrock conditions, Swedish Nuclear Fuel and Waste Management Co., Stockholm Sweden.

O'Mullan, G., M. E. Dueker, K. Clauson, Q. Yang, K. Umemoto, and N. Zakharova (2015), Microbial stimulation and succession following a test well injection simulating CO_2 leakage into a shallow Newark basin aquifer, *Plos One*, 10(1):e0117812.

Pickens, J. F., and G. E. Grisak (1981), Scale-dependent dispersion in a stratified granular aquifer, *Water Resour. Res.*, *17*(4), 1191-1211, doi:10.1029/WR017i004p01191.

Rillard, J., P. Gombert, P. Toulhoat, and P. Zuddas (2014), Geochemical assessment of CO2 perturbation in a shallow aquifer evaluated by a push-pull field experiment, *Int. J. Greenh. Gas Con.*, *21*, 23-32.

Schroth, M. H., J. Kleikemper, C. Bolliger, S. M. Bernasconi, and J. Zeyer (2001), In situ assessment of microbial sulfate reduction in a petroleum-contaminated aquifer using push-pull tests and stable sulfur isotope analyses, *J. Contam. Hydrol., 51*(3-4), 179-195.

Schumer, R., D. A. Benson, M. M. Meerschaert, and B. Baeumer (2003), Fractal mobile/immobile solute transport, *Water Resour. Res.*, *39*, 1296, doi:10.1029/2003WR002141.

Tsang, Y. W. (1995), Study of alternative tracer tests in characterizing transport in fractured rocks, *Geophys. Res. Lett.*, *22*(11), 1421-1424.

Voss, C. I. (1984), SUTRA –Saturated-Unsaturated Transport. A finite element simulation model for saturated-unsaturated fluid-density-dependent ground-water flow with energy transport or chemically-reactive single-species solute transport. U.S. Geological Survey Water-Resources Investigations Report 84-4369.

Wang, Q. R., and H. B. Zhan (2015), On different numerical inverse Laplace methods for solute transport problems, *Adv. Water. Resour.*, *75*, 80-92.

Wang, Q. R., H. B. Zhan and Y. X. Wang (2017), Single-well push-pull test in transient Forchheimer flow field. *J. Hydrol.*, *549*, 125-132.

Wu, Y. S., and L. H. Pan (2005), An analytical solution for transient radial flow through unsaturated fractured porous media, *Water Resour. Res.*, *41*, W02029, doi:10.1029/2004WR003107.

Yang, C. B., P. J. Mickler, R. Reedy, B. R. Scanlon, K. D. Romanak, J. P. Nicot, S. D. Hovorka, R. H. Trevino, and T. Larson (2013), Single-well push-pull test for assessing potential impacts of CO2 leakage on groundwater quality in a shallow Gulf Coast aquifer in Cranfield, Mississippi, *Int. J. Greenh. Gas Con.*, *18*, 375-387.

Yang, Q., J. Matter, M. Stute, T. Takahashi, G. O'Mullan, K. Umemoto, K. Clauson, M. Elias Dueker, N. Zakharova, J. Goddard, and D. Goldberg (2014), Groundwater

hydrogeochemistry in injection experiments simulating CO2 leakage from geological storage reservoir, *Int. J. Greenh. Gas Con*., *26*, 193-203.

Zhan, H. B., Z. Wen, and G. Y. Gao (2009), An analytical solution of two-dimensional reactive solute transport in an aquifer-aquitard system, *Water Resour. Res.*, *45*, W10501, doi:10.1029/2008WR007479.

Zhang, Y. (2009), Finite difference approximations for space-time fractional partial differential equation, *J. Numer. Math.*, *17*(4), 319-326.

Zhang, Y., M. M. Meerschaert, B. Baeumer and E. M. LaBolle (2015), Modeling mixed retention and early arrivals in multidimensional heterogeneous media using an explicit Lagrangian scheme, *Water Resour. Res.*, 51, 6311–6337, doi:10.1002/2015WR016902.

CHAPTER V

SUMMARY

This study uses three cases to demonstrate how to use heat and chemical tracers to infer the subsurface flow at different geological settings. In Chapter II, a novel model was developed to reconstruct the pulsatory magma degassing activity by combined analysis of temperature and chemical data collected at the hot springs near the volcano summit. In Chapter III, an ensemble data assimilation method ES-MDA was developed to calculate the surface water-groundwater exchange flux using high-resolution temperature time-series. And in Chapter IV, a fractional model was developed to interpret the conservative tracer that is collected in SWPP test at a fractured aquifer. Different models were developed at different geological settings to accommodate the characteristic transport behavior of heat source and chemical source. The observed difference between heat and chemical transport in subsurface environments results from the role of solid matrix to the transport process. Heat can conduct through the solid, but chemicals can only be sorbed onto the solid surface and then released dynamically. The heat diffusivity is usually two order of magnitude higher than the chemical diffusivity, thus their transport behavior in subsurface environments show noticeable difference. The chemical tracer we discussed in this study is conservative tracer. No reaction or decay is taken into consideration. Incorporation of reactive tracer into the model to gain more insights into the subsurface environment is an important research area that is worth to be investigated in the future. For example, in the volcanic hydrothermal system, the

high-temperature thermal fluid would affect the rate of absorption and desorption, thus by comparing the chemical composition of degassing gas and water sample collected at the hot spring, we can have a better understanding for the in-situ geochemical properties of the hydrothermal system.

APPENDIX A

DERIVATION OF SOLUTIONS FOR PULSATORY HEAT AND CHEMICAL INJECTION INTO THE HYDROTHERMAL SYSTEM

The governing equation of the heat transport in the aquifer and the boundary condition at the recharge side are given in equations (1). The other boundary condition at the far side is,

$$\left.\frac{\partial T_{aq}}{\partial x}\right|_{x\to\infty,t>0} = 0 \ , \tag{A.1}$$

and the initial condition is,

$$T_{aq}(x, t=0) = T_{ini}(x) \ , \tag{A.2}$$

where $T_{ini}(x)$ is the initial temperature distribution.

The governing equation of the 1D heat conduction in the vadose zone is,

$$\Gamma_{vz}\frac{\partial T_{vz}}{\partial t} = \sigma_{vz}\frac{\partial^2 T_{vz}}{\partial z^2} \ , \tag{A.3}$$

and the boundary and initial conditions are,

$$T_{vz}(z=0, t) = T_{ls}(x) \ , \tag{A.4}$$

$$T_{vz}(z=h_{vz}, t) = T_{aq}(x, t) \ , \tag{A.5}$$

$$T_{vz}(z, t=0) = T_{ls}(x) + g(z+h_{vz}), \tag{A.6}$$

where $T_{ls}(x)$ is the land surface temperature and g is the geothermal gradient.

For the base unit beneath the aquifer, the governing equation is,

$$\Gamma_{bu}\frac{\partial T_{bu}}{\partial t}=\sigma_{bu}\frac{\partial^2 T_{bu}}{\partial z^2}\ , \tag{A.7}$$

and the boundary and initial conditions are,

$$T_{bu}(z=h_{vz}+h_{aq},t)=T_{aq}(x,t)\ , \tag{A.8}$$

$$T_{bu}(z=h_{vz}+h_{aq}+h_{bu},t)=T_f(x)\ , \tag{A.9}$$

$$T_{bu}(z,t=0)=T_{ini}(x)+g(z-h_{vz}-h_{aq}), \tag{A.10}$$

where $T_f(x)$ is the temperature in the deep base unit.

The Laplace transform of equation (A.3) is,

$$\sigma_{vz}\frac{\partial^2\overline{T_{vz}}}{\partial z^2}-\Gamma_{vz}s\overline{T_{vz}}+\Gamma_{vz}\left[T_{ls}+g_{vz}(z+h_{vz})\right]=0\ , \tag{A.11}$$

where the overbar means the term in Laplace domain hereinafter, and s is the Laplace transform parameter in respect to time. The general solution of equation (A.11) is,

$$\overline{T_{vz}}=c_3\cosh\left[\sqrt{\frac{\Gamma_{vz}s}{\sigma_{vz}}}(z-h_{vz})\right]+c_4\sinh\left[\sqrt{\frac{\Gamma_{vz}s}{\sigma_{vz}}}(z-h_{vz})\right]+\frac{T_{ls}+g(z+h_{vz})}{s}\ . \tag{A.12}$$

Substituting equations (A.4) and (A.5) in Laplace domain into equation (A.12), one can get,

$$c_3=\overline{T_{aq}}-\frac{T_{ls}+gh_{vz}}{s}\ , \tag{A.13}$$

$$c_4=-c_3\coth(-h_{vz}\sqrt{\Gamma_{vz}s/\sigma_{vz}})\,. \tag{A.14}$$

The flux between the aquifer and the vadose is,

$$\left.\frac{\partial \overline{T_{vz}}}{\partial z}\right|_{z=0} = c_4\sqrt{\frac{\Gamma_{vz}s}{\sigma_{vz}}} + \frac{g}{s}. \tag{A.15}$$

Following the same procedures from equation (A.11) to equation (A.15), one can get the transient temperature of the basal layer,

$$\overline{T_{bu}} = c_5\cosh\left[\sqrt{\frac{\Gamma_{bu}s}{\sigma_{bu}}}(z-h_{vz}-h_{aq})\right] + c_6\sinh\left[\sqrt{\frac{\Gamma_{bu}s}{\sigma_{bu}}}(z-h_{vz}-h_{aq})\right] + \frac{T_{ini}+g(\mathrm{z}-h_{vz}-h_{aq})}{s}, \tag{A.16}$$

$$c_5 = \overline{T_{aq}} - \frac{T_{ini}}{s}, \tag{A.17}$$

$$c_6 = -c_5\coth\left(\sqrt{\frac{\Gamma_{bu}s}{\sigma_{bu}}}h_{bu}\right), \tag{A.18}$$

and the flux between the aquifer and the basal layer is,

$$\left.\frac{\partial \overline{T_{bu}}}{\partial z}\right|_{z=0} = c_6\sqrt{\frac{\Gamma_{bu}s}{\sigma_{bu}}} + \frac{g}{s}. \tag{A.19}$$

Substituting the flux term (equations (A.15) and (A.19)) and boundary conditions (equations (1b) and (2)) into the Laplace form of equation (1a), one can get the transient temperature of aquifer,

$$\overline{T_{aq}}(x,s) = c_1\exp\left(\frac{u\rho_w c_w\theta - \sqrt{(u\rho_w c_w\theta)^2 + 4\sigma_{aq}M}}{2\sigma_{aq}}x\right) + \frac{N}{M}, \tag{A.20}$$

$$M = \Gamma_{aq} s + \coth\left(\sqrt{\frac{\Gamma_{bu} s}{\sigma_{bu}}} h_{bu}\right) \frac{\sqrt{\Gamma_{bu}\sigma_{bu} s}}{h_{aq}} - \coth\left(-\sqrt{\frac{\Gamma_{vz} s}{\sigma_{vz}}} h_{vz}\right) \frac{\sqrt{\Gamma_{vz}\sigma_{vz} s}}{h_{aq}} \ , \tag{A.21}$$

$$N = \frac{\sigma_{bu}}{h_{aq}} \left[\frac{T_{ini}}{s} \coth\left(\sqrt{\frac{\Gamma_{bu} s}{\sigma_{bu}}} h_{bu}\right) \sqrt{\frac{\Gamma_{bu} s}{\sigma_{bu}}} + \frac{g}{s} \right] - \frac{\sigma_{vz}}{h_{aq}} \left[\frac{T_s + g h_{vz}}{s} \coth\left(-\sqrt{\frac{\Gamma_{vz} s}{\sigma_{vz}}} h_{vz}\right) \sqrt{\frac{\Gamma_{vz} s}{\sigma_{vz}}} + \frac{g}{s} \right] , \tag{A.22}$$

$$c_1 = \sum_{j=1}^{P_{num}} \frac{T_{r,j}}{s} [\exp(-s t_{j-1}) - \exp(-s t_j)] - \frac{N}{M} \ . \tag{A.23}$$

Numerical Laplace inversion is conducted using the de Hoog method which works well in both advection-dominated and dispersion-dominated problems.

Considering the equivalence between the convection-diffusion equation and advection-dispersion equation in terms of mathematical form, the above solution can be easily modified to describe the solute transport in the aquifer with infinite pulsatory injection,

$$C_{aq}(x, s) = c_2 \exp\left(\frac{u\theta - \sqrt{(u\theta)^2 + 4Ds}}{2D} x \right) , \tag{A.24}$$

$$c_2 = \sum_{j=1}^{P_{num}} \frac{C_{r,j}}{s} \left[\exp\left(-s t_{j-1}\right) - \exp\left(-s t_j\right) \right] . \tag{A.25}$$

Table A.1. Hydraulic and thermal parameters used in the models of CE, Ga and CC springs

Parameters	CE	Ga	CC
Groundwater velocity[1] (m/s)	1×10^{-5}	1×10^{-5}	1×10^{-5}
Dispersivity[1] (m)	20	30	30
Aquifer Length[1] (m)	75	650	2500
Vadose zone thickness[2] (m)	100	150	150
Saturated flow thickness[3] (m)	2	2	2
Volumetric heat capacity of the aquifer[4] (J/m^3K)	2.8×10^{6}	2.8×10^{6}	2.8×10^{6}
Volumetric heat capacity of the vadose zone[4]	2.7×10^{6}	2.7×10^{6}	2.7×10^{6}
Volumetric heat capacity of the base unit[4] (J/m^3K)	2.7×10^{6}	2.7×10^{6}	2.7×10^{6}
Thermal conductivity of the aquifer[4] (W/mK)	1.9	1.9	1.9
Thermal conductivity of the vadose zone[4] (W/mK)	1.97	1.97	1.97
Thermal conductivity of the base unit[4] (W/mK)	1.97	1.97	1.97

[1]: Villemant et al. (2005);
[2]: Rosas-Carbajal et al. (2016);
[3]: Estimated from the average flux at spring (Villemant et al., 2014);
[4]: Eppelbaum et al. (2014).

APPENDIX B

NUMERICAL SOLUTIONS FOR FRACTIONAL MODEL AND SEMI-ANALYTICAL SOLUTION FOR MOBILE-IMMOBILE MODEL OF SWPP TEST

B.1. Implicit Euler Method for the Fractional Models

B.1.1. Injection stage

The governing equation of the FTS model is given in equation (14). The time fractional Riemann-Liouville derivative $\partial^{\gamma_{inj}} c_m / \partial t^{\gamma_{inj}}$ is defined as

$$\frac{\partial^{\gamma_{inj}} c_m(r,t)}{\partial t^{\gamma_{inj}}} = \frac{1}{\Gamma(1-\gamma_{inj})} \frac{\partial}{\partial t} \int_0^t \frac{c_m(r,\eta)}{(t-\eta)^{\gamma_{inj}}} d\eta \tag{B.1}$$

, and the spatial fractional Riemann-Liouville derivative $\partial^{\alpha} c_m / \partial r^{\alpha}$ is defined as

$$\frac{\partial^{\alpha} c_m(r,t)}{\partial r^{\alpha}} = \frac{1}{\Gamma(2-\alpha)} \frac{\partial^2}{\partial r^2} \int_0^r \frac{c_m(\xi,t)}{(r-\xi)^{\alpha-1}} d\xi \tag{B.2}$$

Note that the time fractional Riemann-Liouville derivative $\partial^{\gamma_{inj}} c_m / \partial t^{\gamma_{inj}}$ is identical to time fractional Caputo derivative

$$\frac{\partial^{\gamma_{inj}} c_m(r,t)}{\partial t^{\gamma_{inj}}} = \frac{1}{\Gamma(1-\gamma_{inj})} \int_0^t (t-\eta)^{-\gamma_{inj}} \frac{\partial c_m(r,\eta)}{\partial \eta} d\eta \tag{B.3}$$

with the initial condition that $c_m(r,0) = 0$ (Baleanu et al., 2012). It is preferred to study the fractional differential equation with the Caputo derivative because its properties make it easier for numerical solution (Dimitrov, 2014).

The discretization scheme for time is $t_k = k\Delta t$ ($k = 0, 1, 2, \ldots, t_{pump}/\Delta t$) where Δt is a uniform time step and $t_{pump}/\Delta t$ is the total number of time steps. t_k satisfies $0 \le t_k \le t_{pump}$. Note that $k = 0$ indicates the initial concentration. For space discretization, the distance of grid i to the wellbore

is $r_i=i\Delta r$ (i=1, 2, …, m) where Δr is the uniform radial step and m is the total number of grids. r_i satisfies $r_w \le r_i \le r_e$. The finite-difference approximation to the Caputo derivative equation (B.3) is

$$\begin{aligned}\frac{\partial^{\gamma_{inj}} c_m(r_i,t_{k+1})}{\partial t^{\gamma_{inj}}} &= \frac{1}{\Gamma(1-\gamma_{inj})}\sum_{j=0}^{k}\frac{c_m(r_i,t_{j+1})-c_m(r_i,t_j)}{\Delta t}\int_{j\Delta t}^{(j+1)\Delta t}\frac{d\xi}{(t_{k+1}-\xi)^{\gamma_{inj}}}+O(\Delta t)\\ &= \frac{\Delta t^{1-\gamma_{inj}}}{\Gamma(2-\gamma_{inj})}\sum_{j=0}^{k}\frac{c_m(r_i,t_{k+1-j})-c_m(r_i,t_{k-j})}{\Delta t}\left[(j+1)^{1-\gamma_{inj}}-j^{1-\gamma_{inj}}\right]+O(\Delta t)\end{aligned} \tag{B.4}$$

For the Riemann-Liouville derivative, a shifted Grünwald formula is used, which guaranties that the implicit Euler method is unconditionally stable

$$\frac{\partial^{\alpha} c_m(r_i,t_{k+1})}{\partial r^{\alpha}} = \frac{1}{\Delta r^{\alpha}}\sum_{j=0}^{i+1} g_j c_m(r_i-(j-1)\Delta r,t_{k+1})+O(\Delta t+\Delta r) \tag{B.5}$$

where $g_j=\Gamma(j-\alpha)/[\Gamma(-\alpha)\Gamma(j+1)]$, j=1,2,3,….

Substituting equations (4) and (5) into (14) for the injection stage and then discretizing the first derivative terms using the implicit finite-difference method, one gets

$$\begin{aligned}&\frac{c_m(r_i,t_{k+1})-c_m(r_i,t_k)}{\Delta t}+\frac{\beta\tau_{\gamma_{inj}}\Delta t^{1-\gamma_{inj}}}{\Gamma(2-\gamma_{inj})}\sum_{j=0}^{k}\frac{c_m(r_i,t_{k+1-j})-c_m(r_i,t_{k-j})}{\Delta t}\left[(j+1)^{1-\gamma_{inj}}-j^{1-\gamma_{inj}}\right]\\ &=-b(r_i)\frac{c_m(r_i,t_{k+1})-c_m(r_{i-1},t_{k+1})}{\Delta r}+\frac{a(r_i)}{\Delta r^{\alpha}}\sum_{j=0}^{i+1} g_j c_m(r_i-(j-1)\Delta r,t_{k+1}),\ 0\le k<\frac{t_{inj}}{\Delta t}\end{aligned} \tag{B.6}$$

where $b(r_i)=k_v/r_i$ and $a(r_i)=\alpha_L k_v/r_i$. Denote $c_m(r_i,t_k)=c_i^k$, $a_i=a(r_i)$, $b_i=b(r_i)$, $e_j=\left(j+1\right)^{1-\gamma_{inj}}-j^{1-\gamma_{inj}}$, $u_i=a_i\Delta t\Delta r^{-\alpha}$, $w_i=b_i\Delta t\Delta r^{-1}$, $z=\beta\tau_{\gamma_{inj}}\Delta t^{1-\gamma_{inj}}/\Gamma\left(2-\gamma_{inj}\right)$, and equation (B.6) can be rewritten as

$$c_i^{k+1}-c_i^k+z\sum_{j=0}^{k}e_j(c_i^{k+1-j}-c_i^{k-j})=-w_i(c_i^{k+1}-c_{i-1}^{k+1})+u_i\sum_{j=0}^{i+1}g_j c_{i-j+1}^{k+1},\ 0\le k<\frac{t_{inj}}{\Delta t} \tag{B.7}$$

Rearranging equation (B.7)

$$
\begin{aligned}
&-u_i g_0 c_{i+1}^{k+1} + (w_i - u_i g_1 + z e_0 + 1) c_i^{k+1} - (w_i + u_i g_2) c_{i-1}^{k+1} - u_i \sum_{j=3}^{i+1} g_j c_{i-j+1}^{k+1} \\
&= c_i^k + z \sum_{j=0}^{k-1} (e_j - e_{j+1}) c_i^{k-j} + z e_k c_i^0,\ 0 \le k < \frac{t_{inj}}{\Delta t}
\end{aligned}
\tag{B.8}
$$

The matrix form of equation (B.8) is

$$
\begin{cases}
A_{inj} U^1 = (z e_0 - z e_1 + 1) U^0 + H_{inj},\ k = 0 \\
A_{inj} U^{k+1} = U^k + z \sum_{j=0}^{k-1} (e_j - e_{j+1}) U^{k-j} + z e_k U^0 + H_{inj},\ 0 < k < \frac{t_{inj}}{\Delta t}
\end{cases}
\tag{B.9}
$$

where $U^k = (c_1^k, c_2^k, \ldots, c_m^k)^T$, $H_{inj} = ((w_1 + u_1 g_2) c_{inj}, \overbrace{0, \ldots, 0}^{m-1})^T$ and coefficient matrix A_{inj} is

$$
A_{inj(i,j)} = \begin{cases}
-u_i g_{i-j+1}, & j < i-1 \\
-w_i - u_i g_2, & j = i-1 \\
w_i - u_i g_1 + z e_0 + 1, & j = i \\
-u_i g_0, & j = i+1 \\
0, & j > i+1
\end{cases}
\tag{B.10}
$$

B.1.2. Chasing stage

The discretized equation for the chasing stage is the same as equation (8). Note that the term $\sum_{j=1}^{k-1} (e_j - e_{j+1}) c_i^{k-j}$ contains all the past concentration information at grid *i*, including the whole injection stage and the chasing stage before time step *k*+1. Therefore, the matrix form should be modified from equation (B.9) accordingly

$$
\begin{cases}
A_{cha} U^{k+1} = U^k + z \sum_{j=0}^{k-1} (e_j - e_{j+1}) U^{k-j} + z e_k U^0,\ k = \frac{t_{inj}}{\Delta t} \\
A_{cha} U^{k+1} = U^k + z \sum_{j=k-t_{inj}/\Delta t}^{k-1} (e_j - e_{j+1}) U^{k-j} + z \sum_{j=0}^{k-t_{inj}/\Delta t-1} (e_j - e_{j+1}) U^{k-j} \\
\qquad\qquad + z e_k U^0,\ \frac{t_{inj}}{\Delta t} < k < \frac{t_{cha}}{\Delta t}
\end{cases}
\tag{B.11}
$$

where $e_j = \left(j+1\right)^{1-\gamma_{cha}} - j^{1-\gamma_{cha}}$, $z = \beta\tau_{\gamma_{cha}}\Delta t^{1-\gamma_{cha}} / \Gamma\left(2-\gamma_{cha}\right)$, $A_{cha} = A_{inj}$, and $t_{cha}/\Delta t$ is the total time steps at the end of the chasing stage. Note that the term H_{inj} is omitted here because the concentration of chasing fluid is zero.

B.1.3. Resting stage

The resting stage in equation (14) is discretized similarly

$$\frac{c_m(r_i,t_{k+1})-c_m(r_i,t_k)}{\Delta t}+\frac{\Delta t^{1-\gamma}}{\Gamma(2-\gamma)}\sum_{j=0}^{k}\frac{c_m(r_i,t_{k+1-j})-c_m(r_i,t_{k-j})}{\Delta t}\left[(j+1)^{1-\gamma}-j^{1-\gamma}\right] = 0,\ \frac{t_{cha}}{\Delta t}\le k<\frac{t_{rest}}{\Delta t} \tag{B.12}$$

where $t_{rest}/\Delta t$ is the total time steps at the end of the resting stage. Following the conventions of equation (B.7) and rearranging equation (B.12), one has

$$(ze_0+1)c_i^{k+1} = c_i^k + z\sum_{j=0}^{k-1}(e_j-e_{j+1})c_i^{k-j} + ze_kc_i^0,\ \frac{t_{cha}}{\Delta t}\le k<\frac{t_{rest}}{\Delta t} \tag{B.13}$$

The matrix form of equation (B.13) is

$$\begin{cases} A_{rest}U^{k+1} = U^k + z\sum\limits_{j=k-t_{inj}/\Delta t}^{k-1}(e_j-e_{j+1})U^{k-j} + z\sum\limits_{j=k-t_{cha}/\Delta t}^{k-t_{inj}/\Delta t-1}(e_j-e_{j+1})U^{k-j} + ze_kU^0,\ k=\dfrac{t_{cha}}{\Delta t} \\ A_{rest}U^{k+1} = U^k + z\sum\limits_{j=k-t_{inj}/\Delta t}^{k-1}(e_j-e_{j+1})U_{inj}{}^{k-j} + z\sum\limits_{j=k-t_{cha}/\Delta t}^{k-t_{inj}/\Delta t-1}(e_j-e_{j+1})U^{k-j} \\ \qquad + z\sum\limits_{j=0}^{k-t_{cha}/\Delta t-1}(e_j-e_{j+1})U^{k-j} + ze_kU^0,\ \dfrac{t_{cha}}{\Delta t}<k<\dfrac{t_{rest}}{\Delta t} \end{cases} \tag{B.14}$$

where $e_j = \left(j+1\right)^{1-\gamma_{rest}} - j^{1-\gamma_{rest}}$, $z = \beta\tau_{\gamma_{rest}}\Delta t^{1-\gamma_{rest}} / \Gamma\left(2-\gamma_{rest}\right)$ and A_{rest} is

$$A_{rest(i,j)} = \begin{cases} 0, & j<i-1 \\ 0, & j=i-1 \\ z_ie_0+1, & j=i \\ 0, & j=i+1 \\ 0, & j>i+1 \end{cases} \tag{B.15}$$

B.1.4. Pumping stage

The spatial fractional Riemann-Liouville derivative $\partial^{\alpha}c_m/\partial(-r)^{\alpha}$ is defined as

$$\frac{\partial^{\alpha}c_m(r,t)}{\partial(-r)^{\alpha}}=\frac{1}{\Gamma(2-\alpha)}\frac{\partial^2}{\partial r^2}\int_r^{r_e}\frac{c_m(\xi,t)}{(r-\xi)^{\alpha-1}}d\xi \tag{B.16}$$

Using the shifted Grünwald formula

$$\frac{\partial^{\alpha}c_m(r_i,t_{k+1})}{\partial(-r)^{\alpha}}=\frac{1}{\Delta r^{\alpha}}\sum_{j=0}^{m-i+1}g_j c_m(r_i+(j-1)\Delta r,t_{k+1})+O(\Delta t+\Delta r) \tag{B.17}$$

one can get the discretized form of equation (B.14) for the pumping stage

$$\begin{aligned}&\frac{c_m(r_i,t_{k+1})-c_m(r_i,t_k)}{\Delta t}+\frac{\Delta t^{1-\gamma}}{\Gamma(2-\gamma)}\sum_{j=0}^{k}\frac{c_m(r_i,t_{k+1-j})-c_m(r_i,t_{k-j})}{\Delta t}\left[(j+1)^{1-\gamma}-j^{1-\gamma}\right]\\&=b(r_i)\frac{c_m(r_i,t_{k+1})-c_m(r_{i-1},t_{k+1})}{\Delta r}+\frac{a(r_i)}{\Delta r^{\alpha}}\sum_{j=0}^{m-i+1}g_j c_m(r_i+(j-1)\Delta r,t_{k+1}),\ \frac{t_{rest}}{\Delta t}\le k<\frac{t_{pump}}{\Delta t}\end{aligned} \tag{B.18}$$

where $t_{pump}/\Delta t$ is the total time steps at the end of the pumping stage. Following the conventions of equation (B.7) and rearranging equation (B.16), one gets

$$\begin{aligned}&-u_i\sum_{j=2}^{m-i+1}g_j c_{i+j-1}^{k+1}+(w_i+ze_0+1-u_i g_1)c_i^{k+1}-(w_i+u_i g_0)c_{i-1}^{k+1}\\&=c_i^k+z\sum_{j=0}^{k-1}(e_j-e_{j+1})c_i^{k-j}+ze_k c_i^0,\ \frac{t_{rest}}{\Delta t}\le k<\frac{t_{pump}}{\Delta t}\end{aligned} \tag{B.19}$$

The matrix form of equation (B.17) is

$$\begin{cases} A_{pump}U^{k+1} = U^{k} + z\sum_{j=k-t_{inj}/\Delta t}^{k-1}(e_j - e_{j+1})U_{inj}{}^{k-j} + z\sum_{j=k-t_{cha}/\Delta t}^{k-t_{inj}/\Delta t-1}(e_j - e_{j+1})U^{k-j} \\ \qquad + z\sum_{j=0}^{k-t_{cha}/\Delta t-1}(e_j - e_{j+1})U^{k-j} + ze_kU^{0},\ k = \dfrac{t_{rest}}{\Delta t} \\ A_{pump}U^{k+1} = U^{k} + z\sum_{j=k-t_{inj}/\Delta t}^{k-1}(e_j - e_{j+1})U^{k-j} + z\sum_{j=k-t_{cha}/\Delta t}^{k-t_{inj}/\Delta t-1}(e_j - e_{j+1})U^{k-j} \\ \qquad + z\sum_{j=k-t_{rest}/\Delta t}^{k-t_{pump}/\Delta t-1}(e_j - e_{j+1})U^{k-j} + z\sum_{j=0}^{k-t_{pump}/\Delta t-1}(e_j - e_{j+1})U^{k-j} + ze_kU^{0},\ \dfrac{t_{rest}}{\Delta t} < k < \dfrac{t_{pump}}{\Delta t} \end{cases} \tag{B.20}$$

where $e_j = (j+1)^{1-\gamma_{pump}} - j^{1-\gamma_{pump}}$, $z = \beta\tau_{\gamma_{pump}}\Delta t^{1-\gamma_{pump}} / \Gamma(2-\gamma_{pump})$ and A_{pump} is

$$A_{pump(i,j)} = \begin{cases} 0, & j < i-1 \\ -w_i - u_i g_0, & j = i-1 \\ w_i + ze_0 + 1 - u_i g_1, & j = i \\ -u_i g_{j-i+1}, & j > i \end{cases} \tag{B.21}$$

For the FT model, only the Caputo derivative is discretized as shown above and the Fickian flux term is approximated using the traditional implicit finite-difference method. The FS model is solved similarly.

B.2 Semi-analytical Solution for the FORMIM Model

B.2.1. Injection and chasing stages

The dimensionless ADE for the mobile zone of the FORMIM model in injection and chasing stages is given in equation (22). Conducting Laplace transform to equation (22), one can get the mobile concentration in Laplace domain

$$\frac{1}{\rho}\frac{\partial\overline{c_m}'}{\partial\rho^2} - \frac{1}{\rho}\frac{\overline{c_m}'}{\partial\rho} - \varepsilon_m(\overline{c_m}' - \overline{c_{im}}') - s\overline{c_m}' = 0 \tag{B.22}$$

The immobile concentration in Laplace domain is given in equation (28). Substituting equation (28) into equation (B.22), one obtains

$$\frac{1}{\rho}\frac{\partial \overline{c_m}'}{\partial \rho^2} - \frac{1}{\rho}\frac{\overline{c_m}'}{\partial \rho} - A_1 \overline{c_m}' = 0 \tag{B.23}$$

where

$$A_1 = \varepsilon_m + s - \frac{\varepsilon_m \varepsilon_{im}}{s + \varepsilon_{im}} \tag{B.24}$$

The boundary conditions (equations 15 and 18) in Laplace domain are respectively

$$\overline{c_m}'(\rho_w, s) = \frac{1 - \exp(-\tau_{inj} s)}{s} \tag{B.25}$$

$$\overline{c_m}'(\rho_e, s) = 0 \tag{B.26}$$

where ρ_e is the dimensionless outer radius.

Note that equation (B.23) is a second-order ordinary differential equation (ODE) with variable coefficients. To transform it to self-adjoint form, substituting the following transformed variables into equation (B.23)

$$y = \rho + \frac{1}{4A_1} \tag{B.27}$$

$$\overline{c_{mt}}' = \overline{c_m}' \exp\left(-\frac{y}{2}\right) \tag{B.28}$$

$$\rho_t = A_1^{1/3} y \tag{B.29}$$

where $\overline{c_{mt}}'$ is the transformed mobile concentration in Laplace domain and ρ_t is the transformed dimensionless radius. Equation (B.23) is then transformed to

$$\frac{\partial^2 \overline{c_{mt}}'}{\partial \rho_t^2} = \rho_t \overline{c_{mt}}' \tag{B.30}$$

Equation (B.30) is the standard form of Airy equation and the solution is a linear combination of Airy functions $A_i(x)$ and $B_i(x)$, so

$$\overline{c_m}'(\rho, s) = a_0 \exp\left(\frac{y}{2}\right) A_i\left(A_1^{1/3} y\right) + b_0 \exp\left(\frac{y}{2}\right) B_i\left(A_1^{1/3} y\right) \tag{B.31}$$

As $B_i(x)$ diverges when $\rho \to \infty$, b_0 has to be zero. Substituting the boundary condition equations (B.25) and (B.26) into equation (B.31), a_0 is obtained

$$a_0 = \frac{\exp\left(-\frac{y_w}{2}\right)}{s A_i\left(A_1^{1/3} y_w\right)} \tag{B.32}$$

where $y_w = \rho_w + 1/4A_1$. Substituting equation (B.32) and $b_0 = 0$ into equation (B.31), one can get

$$\overline{c_m}'(\rho, s) = \frac{1}{s} \exp\left(\frac{y - y_w}{2}\right) \frac{A_i\left(A_1^{1/3} y\right)}{A_i\left(A_1^{1/3} y_w\right)} \tag{B.33}$$

Combining equations (B.33) and (50) will result in

$$\overline{c_{im}}'(\rho, s) = \frac{\varepsilon_{im}}{(s + \varepsilon_{im}) s} \exp\left(\frac{y - y_w}{2}\right) \frac{A_i\left(A_1^{1/3} y\right)}{A_i\left(A_1^{1/3} y_w\right)} \tag{B.34}$$

B.2.2 Resting stage

The dimensionless mobile zone equation in the resting stage is

$$\frac{\partial c_m'}{\partial \tau} = -\varepsilon_m (c_m' - c_{im}') \tag{B.35}$$

Rearranging equation (B.35)

$$c_{im}' = c_m' + \frac{1}{\varepsilon_m}\frac{\partial c_m'}{\partial \tau} \tag{B.36}$$

Substituting equation (B.36) into (B.22), one can get

$$\frac{\partial^2 c_m'}{\partial \tau^2} + (\varepsilon_m + \varepsilon_{im})\frac{\partial c_m'}{\partial \tau} = 0 \tag{B.37}$$

Equation (B.37) is a second order ODE with constant coefficients. The general solution is

$$c_m'(\rho, \tau) = c_1 e^{l_1 \tau} + c_2 e^{l_2 \tau} \tag{B.38}$$

where l_1 and l_2 are the roots of the following characteristic equation

$$l^2 + (\varepsilon_m + \varepsilon_{im})l = 0 \tag{B.39}$$

The solution of equation (B.39) is

$$l_1 = 0 \tag{B.40}$$

$$l_2 = -(\varepsilon_m + \varepsilon_{im}) \tag{B.41}$$

The initial condition in dimensionless form is

$$c_m'(\rho, \tau_{rest} \to \tau_{cha}) = c_m'(\rho, \tau_{cha}) \tag{B.42}$$

Coefficients c_1 and c_2 are calculated by substituting equations (B.40)-(B.42) and (B.30)-(B.31) into equation (B.38), then the mobile concentration in the resting stage is obtained (equation (B.32)).

B.2.3. Pumping stage

In the pumping stage, flow velocity is reversed, so governing equation is modified accordingly (equation (B.36)). The dimensionless mobile and immobile stage equations in Laplace domain are respectively

$$\frac{1}{\rho}\frac{\partial^2 \overline{c_m}'}{\partial \rho^2}+\frac{1}{\rho}\frac{\partial \overline{c_m}'}{\partial \rho}-\varepsilon_m(\overline{c_m}'-\overline{c_{im}}')-s\overline{c_m}'+c_m'(\rho,\tau_{rest})=0 \qquad \text{(B.43)}$$

$$s\overline{c_{im}}'-c_{im}'(\rho,\tau_{rest})=\varepsilon_{im}(\overline{c_m}'-\overline{c_{im}}') \qquad \text{(B.44)}$$

Substituting $\overline{c_{\imath m}'}$ obtained from equation (B.44) into equation (B.43), one can get

$$\frac{1}{\rho}\frac{\partial^2 \overline{c_m}'}{\partial \rho^2}+\frac{1}{\rho}\frac{\partial \overline{c_m}'}{\partial \rho}-A_3\overline{c_m}'+B_3(\rho)=0 \qquad \text{(B.45)}$$

where A_3 and B_3 are given in equations (B.47) and (B.48), respectively. Chen (1988) gave a closed-form analytical solution for pumping problem when there is no immobile zone. If immobile zone is taken into consideration, only semi-analytical solution is obtainable. The semi-analytical solution (equations (40)-(49)) is borrowed from Chen's (1988) work by replacing the coefficient of the first-order term and the distance-dependent term with A_3 and B_3, respectively.